Études Interdisciplinaires de Nanoparticules et de Nanocristaux par Microscopies Électroniques

Wai-Li Ling

HAL Id: tel-02268997

https://hal.univ-grenoble-alpes.fr/tel-02268997

Submitted on 22 Aug 2019

UNIVERSITÉ GRENOBLE-ALPES

Études Interdisciplinaires de Nanoparticules et de Nanocristaux par Microscopies Électroniques

Par

Wai Li Winnie Ling

Habilitation à diriger des recherches de Physique

Présentée et soutenue publiquement le 28 Juin 2019

Rapporteurs:
Catherine VENIEN-BRYAN, professeure
Daniel PICOT, directeur de recherche
Jan Pieter ABRAHAMS, professeur

Jury:
Catherine VENIEN-BRYAN, professeure
Daniel PICOT, directeur de recherche
Maité PATERNOSTRE, directrice de recherche
Jean-Luc PUTAUX, directeur de recherche
Carlo PETOSA, directeur de recherche

UNIV. GRENOBLE-ALPES

Interdisciplinary Studies of Nanoparticles and Nanocrystals by Electron Microscopies

By

Wai Li Winnie Ling

Habilitation à diriger des recherches de Physique

Presented and defended publicly on the 28th of June 2019

Reporters:
Catherine VENIEN-BRYAN, professor
Daniel PICOT, director of research
Jan Pieter ABRAHAMS, professor

Jury:
Catherine VENIEN-BRYAN, professor
Daniel PICOT, director of research
Maité PATERNOSTRE, director of research
Jean-Luc PUTAUX, director of research
Carlo PETOSA, director of research

Table of Contents:

Introduction

This report summarizes my major research activities in material science and later also in life science since I obtained my PhD and outlines the projects that I plan to work on. I started at the University of Chicago aspiring to become a biologist. My first research experience was as a summer student under the supervision of Dr. G. Ajlani in Prof. R. Haselkorn's laboratory working on the D1 protein of the photosystem II in purple bacteria. For various reasons, I later chose to pursue physics and mathematics. I obtained a PhD in condensed matter physics and carried out a postdoctoral fellowship in material science. My second postdoctoral fellowship brought me back to life science and I have since worked on projects that involve multiple disciplines.

At the University of California at Berkeley, I did my PhD thesis with Prof. Z.Q. Qiu and Dr. M. Salmeron on applying scanning tunneling microscopy to study magnetic thin films. It involved building a new scanning tunneling microscope and a sample preparation system to grow, magnetize, and characterize epitaxial thin films in an ultra-high vacuum chamber. The design and construction of this setup took more than two years. With the new instruments, we studied the growth of cobalt films with oxygen as a surfactant. We also studied multilayer structures using photoemission electron microscopy and angle-resolved photoemission spectroscopy at the Advanced Light Source in the Lawrence Berkeley Laboratory. The results gave insights into magnetic phenomena such as spin coupling and spin-reorientation transitions. In addition to research, I conducted undergraduate classes and supervised an undergraduate student (S. Paik) in Qiu group for over a year. The training in Berkeley equipped me with skills in experimental research as well as in laboratory management.

My research activities after completing my PhD are summarized in the first part of this manuscript. My first postdoctoral fellowship was at the Sandia National Laboratories, continuing the work on understanding the growth of ultrathin films. Besides using scanning tunneling microscopy, we used low energy electron microscopy to visualize dynamics in ultrathin films. These works will be presented in Chapter 1.

After about four years at Sandia and over ten years in material science, I joined the collaboration between Prof. J. Sedat and Prof. D. Agard in the University of California at San Francisco medical school. Their laboratories were pioneers in using digital detectors for transmission electron microscopy in life science and were developing a range of new techniques in cryo-electron microscopy, including cryo-electron tomography of vitreous sections, which I worked on. Results were promising (Chapter 2.1) but I had to leave just after one year because of family reason.

Arriving in Grenoble, I had first a joint appointment between CEA-LETI and the Institut de Biologie Structurale (IBS) and later a full appointment at the IBS, which I continue holding. Here, I study nanoparticles as well as protein samples using (scanning) transmission electron microscopy. The main projects will be discussed in Chapter 2.2 and Chapter 3. Very different from my research experience in material science where I was responsible experimentally for sample growth, instrumentation, data collection, as well as data analysis, projects at the IBS involve specialized teams for each stage of the experiments. Moreover, I am no longer attached to a particular instrument. Such changes opened up opportunities to collaborate with experts in different domains and led me to conduct a series of studies on the potential health effects of industrial nanoparticles. The results are described in Chapter 3.2. I also had the opportunity to be involved in a project that used single particle analysis with Dr. G. Schoehn and the results are presented in Chapter 4.

During these years, I have supervised undergraduate and master students, as well as postdoctoral fellows. Obtaining the HDR will allow me to officially supervise thesis, which will permit a more structured framework for transmitting acquired skills and knowledge to the new generation of scientists. Projects that I may involve future PhD students are covered in the second part of this manuscript.

The first part of Section II describes my research project on electron crystallography. Nanocrystals remain my main research interests. Since my arrival at the IBS, I have been working on protein electron diffraction intermittently. Earlier work with precession electron diffraction was terminated by organizational changes of the electron microscope management and access. Meanwhile, the process of

setting up relevant collaborations, the search for suitable protein crystals, and the development of sample preparation techniques have taken years. The recent breakthrough came with the access to a new hybrid pixel detector in Prof. J.P. Abrahams's laboratory at C-CINA through Dr. I. Nederlof, of Amsterdam Scientific introduced to me by Dr. A. Gómez Pérez of NanoMegas. The arrival of Dr. D. Housset in the electron microscopy group at the IBS also sped up the data analysis part of the project. Another aspect of my project involves the characterization of new functional nanocrystals fabricated at the CEA. These nanoparticles have sizes in the nanometer range and often contains organic components, which make them very sensitive to radiation damage. Electron microscopy techniques typical in materials science, intended for samples resistant to radiation damage, are not suitable for these new nanoparticles. We are thus adapting techniques borrowed from life science to characterize these novel nanoparticles. The last project covered in this manuscript is a structural biology project on a flexible protein C1q. C1q is a multifunctional protein with a prominent role in immunity. Despite its importance, its structure and functional mechanism is little understood. A strategy to undertake this problem will be described in Chapter 3. Preliminary work as well as future plans of all the projects will be presented.

Section I. Research Activities

Chapter 1. Understanding crystal growth and surface processes in hetero-epitaxial films

1.1. Strain relief in hetero-epitaxial films

Epitaxy is the deposition of material over a crystalline substrate to obtain a high-quality crystalline thin film. Epitaxial films can possess many interesting physical and chemical properties distinct from bulk materials and are used in a wide range of applications. Materials can be deposited by different means, such as chemical vapor deposition, plasma ablation, or molecular-beam epitaxy (MBE). To be able to control the properties of epitaxial films, their structure and growth needs to be understood. For my first postdoctoral fellowship at the Sandia Laboratories, I studied dislocation structures found during the initial growth of epitaxial films deposited by MBE.

Molecular- beam epitaxy allows a precise control over the film thickness. A beam of material is generated by evaporation from a source. The beam is directed towards the substrate by a collimator. The evaporation rate is measured by a quartz microbalance calibrated against real observation by a scanning tunneling microscope (STM). Sub-monolayer films can be deposited by MBE.

The STM measures the topology of a conducting surface through the quantum mechanical tunneling effect. A very sharp etched metal wire (the 'tip'), ideally terminated in a single atom, is placed within angstroms from the sample surface in an ultra-high vacuum. When a voltage (magnitude in the order of the work function of the substrate) is applied, electrons from the sample can tunnel through the vacuum gap into the tip. At a constant applied voltage, the tunneling current I depends exponentially on the distance d between the surface and the tip. With work function (energy barrier) ϕ, electron charge e, electron mass m, Planck's constant h, and applied voltage V:

$$I(d) \propto eV \, exp\left(\frac{-4\pi\sqrt{2m\phi}}{h}d\right).$$

A piezo adjusts the vertical position of the tip through a feedback loop to keep the tunneling current constant as the tip is scanned across the sample surface. Since the tunneling current changes by orders of magnitude with displacements in the angstrom range, the STM yields very sensitive measurements of the surface topology of the sample and can resolve individual atoms in favorable conditions. The following studies are based on atomic-resolution STM observations on hetero-epitaxial thin films grown on a Ru(0001) substrate.

In hetero-epitaxy, as opposed to homo-epitaxy, the deposited material is different from the substrate material. Due to the difference in the lattice spacings between the film and the substrate in heteroepitaxial films, dislocations are often formed to relieve the strains at the interface. Ordered dislocation structures are particularly interesting because they can act as templates for nanostructures with novel physical or chemical properties.

We deposited Ag and Au onto a clean Ru(0001) substrate prepared by cycles of Ar sputtering and annealing in an ultra-high vacuum ($\sim 10^{-11}$ Torr). Ag and Au, like Ru, forms a close-packed structure. Unlike Ru, which adopts a hexagonal close packed (hcp) structure with stacking "a-b-a-b", Ag and Au adopt the face-centered cubic (fcc) close packed structure with stacking "a-b-c-a-b-c". Ag and Au have lattice constants of 4.08 and 4.07 angstroms, respectively, which give rise to a $\sim7\%$ misfit with the Ru(0001) substrate. The growth of any pseudo-morphic films would result in large compressive strains and would be energetically unfavorable. We found instead a variety of dislocation structures in the heteroepitaxial films that depend sensitively on film composition and coverage.

Striped patterns are found in the first monolayer (ML) films of Ag, Au, and $Ag_{0.5}Au_{0.5}$ alloy. Striped dislocation structure has been observed in a number of (111) metal film surfaces.[1] The stripes are regions of fcc and hcp stacking separated by Shockley partial dislocations. The stripes run in one of the three equivalent fcc <11-2> directions and release the tensile stress in the direction perpendicular to the stripes. (Thus, stripes always run perpendicular to step edges.) Additional relaxation occurs where two rotational domains of the striped phase meet as the boundaries between stripe domains lower

the surface energy by allowing more isotropic strain relief.[2] When two rotational domains are arranged periodically, a herringbone phase is formed. We have found long range herringbone structures in 1 ML Ag, Au, and $Ag_{0.5}Au_{0.5}$ alloy films on Ru(0001).

Figure 1 shows herringbone structures found in 1 ML Au and 1 ML Ag. The herringbone structures can extend to hundreds of nanometers if the Ru terrace is free of defects. Atomically resolved STM image of the elbow region (Figure 1b) shows clearly the edge dislocation where the Shockley partial dislocations of the stripes meet. Figure 1d shows another atomically resolved STM image along the stripe showing the corrugation coming from the fcc and hcp regions. The relative widths of these regions are controlled by the energy difference between the fcc and hcp sites and the proximity to the phase transition from a striped phase to a pseudo-morphic over-layer. For instance, Ag has nearly the same energy in the fcc and hcp sites on Ru from first principles calculations.[3] The Ag/Ru system is highly strained and thus lies far from the phase transition to a pseudo-morphic over-layer. These factors lead to about equal width of fcc and hcp regions in the stripes. Figure 1d shows that the stripes have a periodicity of 13 Ag atoms, distributed over 14 Ru atomic sites, leading to an average atomic spacing of 2.88 angstroms along the close-packed direction, as in bulk Ag. Au stripes, on the other hand, has 24 Au atoms distributed over 25 Ru atom, which makes the Au monolayer ~3% contracted relative to bulk Au.
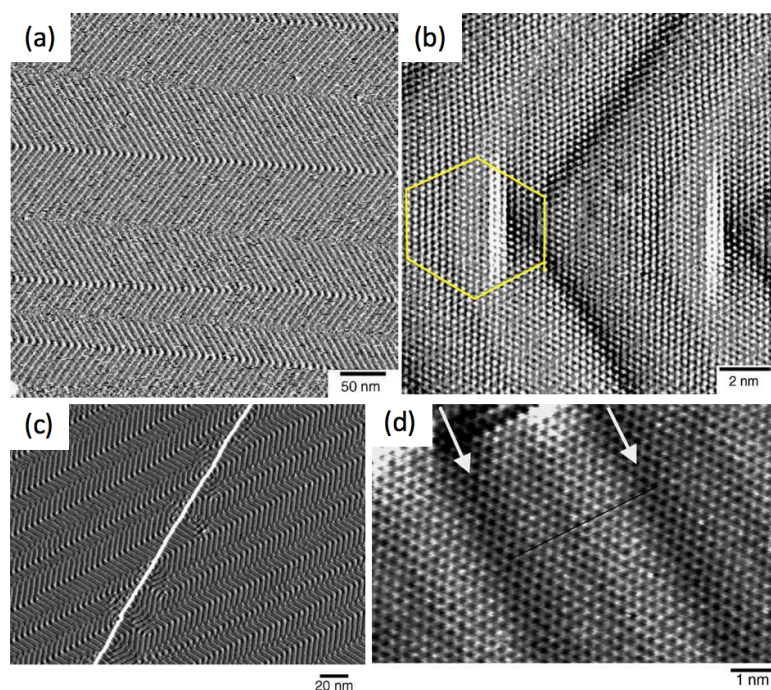

Figure 1. Scanning tunneling microscopy (STM) images of long-period herringbones of Au (a-b) and Ag (c-d) on Ru. (a) Au herringbones on a large terrace. (b) Atomic structure of the elbow at the boundary where two stripe domains meet. The Burgers circuit (yellow) shows a perfect edge dislocation at the intersection of the two partial dislocations. The extra row of atoms at this dislocation core starts on the convex side of the intersecting partial dislocations. (c) Extensive ordering of 1-ML-thick region of a ~1.2 ML Ag film. (d) Atomically resolved image shows strip period of 13 Ag atoms. Arrows point along the <11-2> direction, which the stripes run. The black line shows that the close-packed rows of Ag atoms perpendicular to the stripes undulate slightly as they occupy fcc and hcp sites sequentially.

While only one herringbone phase is found for Au on Ru, two herringbone phases that differ in periodicity were found in 1 ML Ag films. When a second Ag layer coexists with the first layer, the first layer Ag exhibits the long-period herringbone structure with elbow separated by approximately 20 nm (Figure 1c). However, when the Ag layer is incomplete, i.e. sub-monolayer coverage with bare Ru regions, the Ag layer forms a short-period herringbone phase with well-defined periodicity of ~5 nm.

Figure 2 shows the short herringbone structure observed in sub-monolayer Ag on Ru. The atomically resolved image (Figure 2f) allowed us to extract the atomic arrangement and generate a structural model of the system. When the generated structure was relaxed to a force free state using a Frenkel-Kontorova model optimized for Ag and Ru,[4] the atomic positions changed little, consistent with the experimentally observed stability of this layer. The areal densities of Ag atoms are 0.915 and 0.928 of the Ru surface

layer density for the short and long-period herringbone structures, respectively. The conversion from the short period to the long period thus involves densifying the first Ag layer.
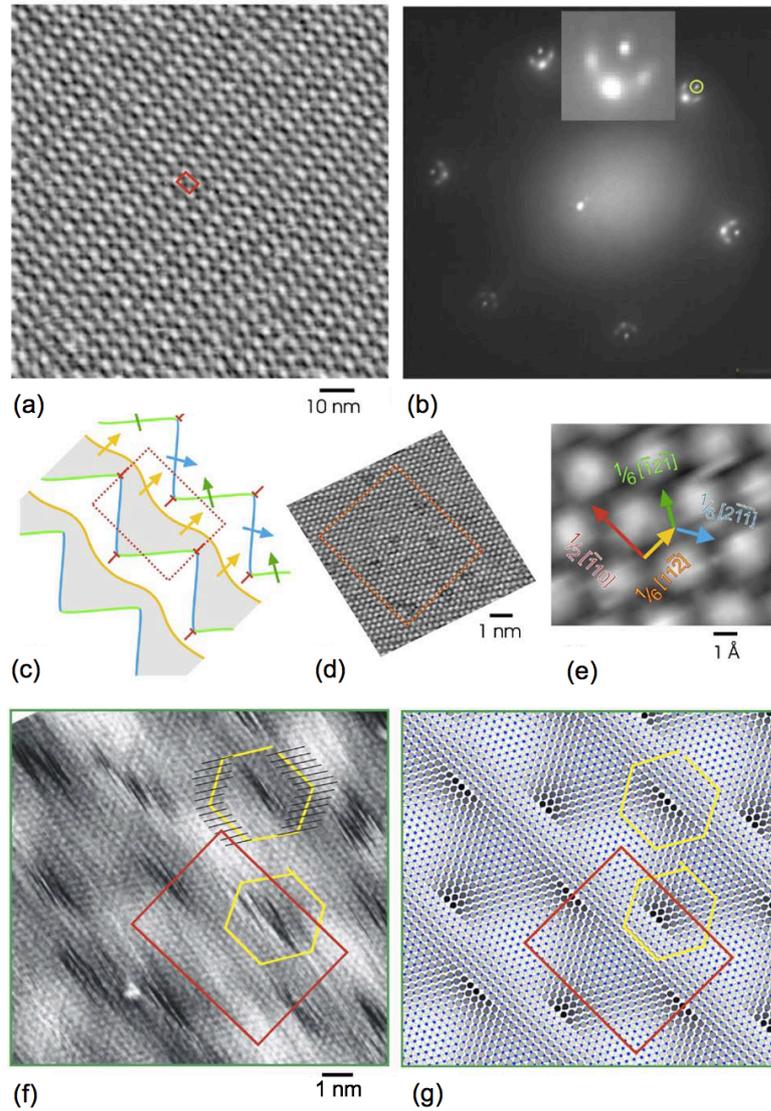

Figure 2. Short-period herringbone reconstruction of a sub-monolayer Ag film on Ru. (a) Larger scale STM image showing the long-range order of the structure. The red rectangle marks a unit cell. (b) Low-energy electron diffraction (LEED) pattern at 38 V from a 1 ML thick film region at 560 °C. A Ru lattice spot is circled. Insert shows an enlarged view around a first order beam. (c) Schematic diagram of the dislocations. The arrows indicate the Burgers vectors of the Shockley partial dislocations. The red T's label the threading dislocations (dark features in f-g). (d-e) Atomic arrangement of the Ru substrate illustrating the size and orientation of the herringbone unit cell (red rectangle) and its Burgers vectors. (f) The burgers circuits (yellow) in the atomically resolved image show the presence of threading dislocations. Black lines guide the eye along the atomic rows. (b) Frenkel-Kontorova model of the short-period herringbone structure. Substrate atoms (Ru) are blue. Ag atoms near on-top sites are dark and those near the two types of threefold hollow site are grey and unshaded, respectively.

We performed selected area low-energy electron diffraction (LEED) and microscopy (LEEM) to study the transition between the short-period herringbone and the long-period herringbone (Figure 3). Diffraction pattern of the short-period herringbone was found as long as bare Ru substrate remains. Once all the Ru surface is covered, the superstructure diffraction spots of the short-period herringbone continuously move closer together. The nucleation of the second Ag layer observed by LEEM coincides with the transformation to the long-period herringbone phase in LEED. Whereas the long-period herringbone has a periodicity of approximately 20 nm, the short-period herringbone structure is very regular with a well-defined unit cell (Figure 2a). The fact that the diffraction spots move closer together suggests that the unit cell size is increasing. In a larger unit cell, more Ag atoms are put in the pseudo-morphic binding sites, thus increasing the density of the Ag atoms.

The change in the first layer Ag structure and thus its density can be understood by considering the high surface energy of Ru. As Ru has a higher surface energy than Ag, binding of the first layer Ag to the Ru substrate is stronger than the binding of the second Ag layer on the first Ag layer. It is thus energetically more favorable to densify the first layer rather than to nucleate the second Ag layer. In the case of Au, the strong Au-Ru binding gives rise to striped monolayer with a density contracted relative to bulk Au.
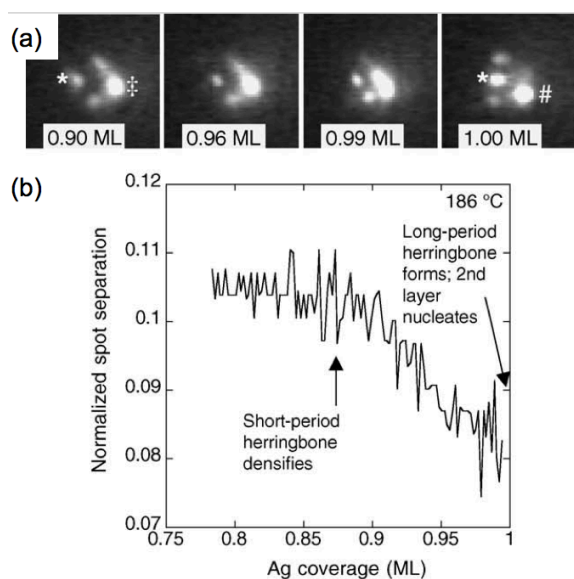
Figure 3. *Selected-area LEED analysis as a function of coverage for the first Ag layer. (a) Transition from short to long-period herringbone at 186 °C. Images are superstructure spots around the first-order Ru spot (asterisk). The double dagger and the pound sign show superstructure spots of the short and long-period herringbone structure, respectively. (b) Separation between a superstructure spot of the short-period herringbone (double dagger in a) and its associated first-order Ru spot is plotted against the Ag coverage. The distance is normalized to the separation between the specular beam and the first-order Ru spot. The LEED pattern shows that the film has the short-period herringbone structure till 0.90 ML. Around 0.91 ML, the superstructure spots move closer together as the film becomes denser as the bare Ru regions vanish. When the second Ag layer nucleates, between 0.99 and 1.00 ML, the LEED pattern abruptly changes to the pattern that corresponds to the long-period herringbone structure.*

The monolayer $Ag_{0.5}Au_{0.5}$ alloy film on Ru also exhibits the herringbone structure, with a periodicity and width in between those of Ag and Au. Figure 4 shows the first layer alloy film coexisting with the second layer film, which forms a trigon structure.
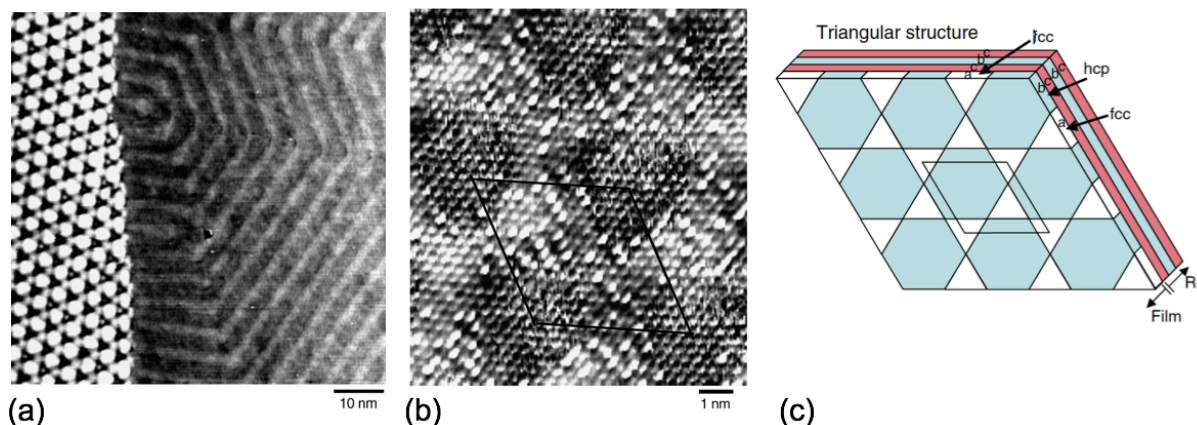

Figure 4. *Triangular dislocation network of $Ag_{0.5}Au_{0.5}$ alloy film. (a) Image of an alloy film with 1.3 ML average thickness showing the 2ML film with the triangular dislocation network on the left and a 1 ML film with the herringbone structure on the right across a monatomic Ru substrate step. (b) Atomically resolved STM image of the triangular dislocation network with a unit cell indicated. The second film layer form a hexagonal mesh free of threading dislocations. The Ag and Au atoms are distinguishable by their different contrast. The atom type that has a brighter contrast prefers one type of hollow site and the other atom type the other. (c) Schematic illustration of the stacking sequence of the 2 ML triangular dislocation structure. The letters indicate the stacking sequence relative to the Ru substrate. Shockley partial dislocations occur only at the first layer/substrate interface.*

When Ag, Au, or $Ag_{0.5}Au_{0.5}$ alloy films on Ru are two or more layers thick, the underlying first layer reconstructs to a highly-ordered dislocation network with a threefold symmetry. Atomic resolution STM images show that the top layers of the 2 ML films in all the three systems to be free of dislocation (Figures 4-6). The dislocation networks thus stay in the first layer and thread through the interface with the substrate and that with the second layer. Contrast in the STM images of these 2 ML films likely arises from vertical displacements or electronic effects originating from the buried interface layer. The triangular network of partial dislocations at the interface of the alloy structure shown in Figure 4

separate film regions of fcc and hcp stacking with respect to the substrate. Nodes are formed by the junctions of six partial dislocations enclosing small triangular regions of film atoms in fcc hollow sites according to embedded atom method (EAM) calculations.

While the 2 ML alloy film consists of one triangular network of dislocations, the 2 ML Au and Ag films form a dislocation structure consisting of three interwoven but independent trigon networks (Figure 5). Each network consists of two sets of Shockley partial dislocations (trigons), one at the Ag-Ru interface and one at the first layer-second layer interface (Figure 5c). Edge dislocations that thread through the first film layer connect the two sets of partial dislocation loops. The dark elongated feature on the edge of the trigons mark the stair-rod dislocations created when the threading edge dislocations dissociate into pairs of partial dislocation. Such dislocation networks avoid the energetically costly on-top site of a pseudo-morphic layer.
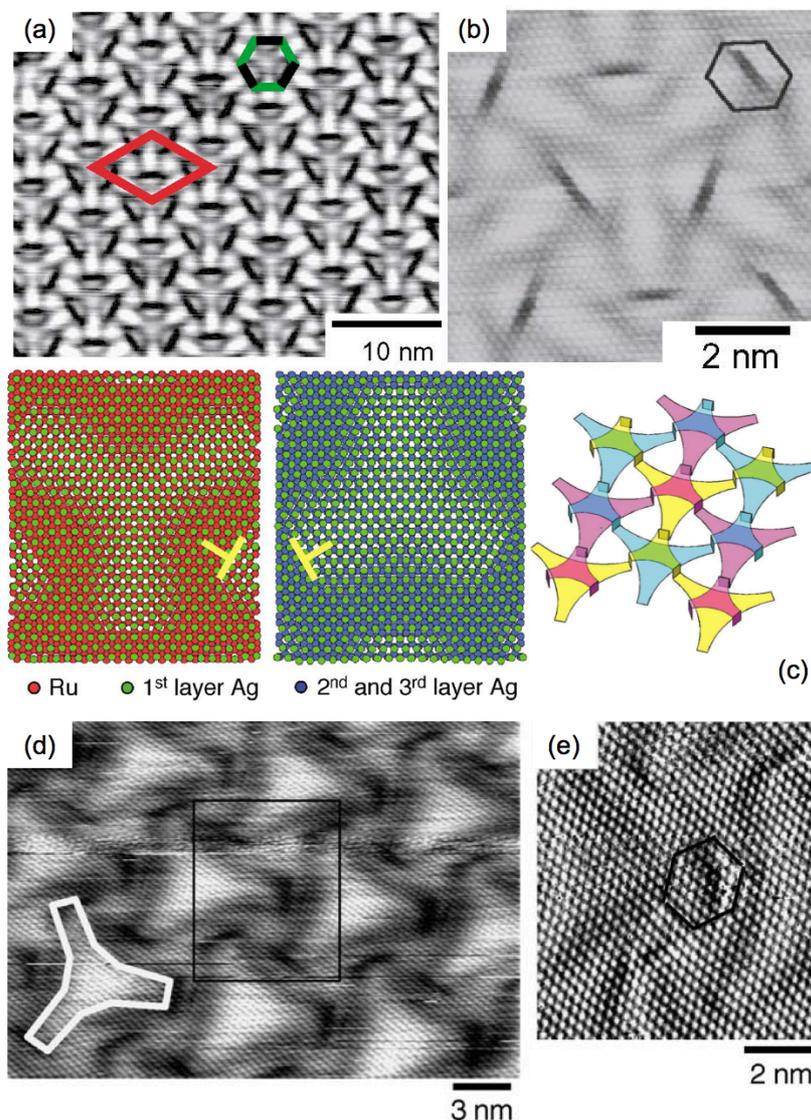

Figure 5. *Trigon dislocation networks in 2 ML Ag and Au film on Ru. (a) Scanning tunneling micrograph of a 2 ML film of Ag on Ru(0001) showing a single domain of the trigon dislocation network. The primitive unit cell is indicated in red and a threefold symmetric 'trigon' is indicated in green. (b) A closed Burgers circuit in the atomic resolved image shows the absence of any edge dislocation at the surface layer. (c) The left two pictures show the results of the embedded atom method calculation for three layers of Ag on Ru(0001) showing the view from the reconstructed Ag interface layer into the Ru bulk (leftmost picture) the two Ag layers (middle picture). Edge dislocations (marked yellow) are located at the edge of the trigon. The rightmost image shows a three-dimensional representation of the heterophase interface reconstruction layer, which consists of three equivalent interwoven dislocation networks (yellow, magenta, and cyan). (d) Trigon structure in 2 ML Au film grown on Ru. (e) Enlarged image of the boxed region in d. The closed Burgers circuit establishes the absence of threading edge dislocations on the surface layer.*

As more layers are deposited, we observed that the 2 ML trigon reconstruction persists in the Ag on Ru system (Figure 6) at the heterophase interphase (interface between two crystals of different composition). We can calculate the Ag chemical potential of the trigon layer using EAM by adding or removing atoms adjacent to the edge dislocations. By matching the Ag chemical potential of the trigon layer to that of bulk Ag, we predicted the density of the Ag interface layer to be ~0.9 relative to the

density of the Ru layer, closer to bulk Ag density than Ru. The result indicates that the larger trigons are at the Ru/Ag interface. The predicted trigon size agrees with the STM observation of ~25 atomic rows along the <11-2> directions. The dislocation networks in the heterophase interphase layer produces a first layer Ag with an intermediate density between Ag and Ru and efficiently relieve the 7% lattice mismatch between film and substrate from the second layer on.
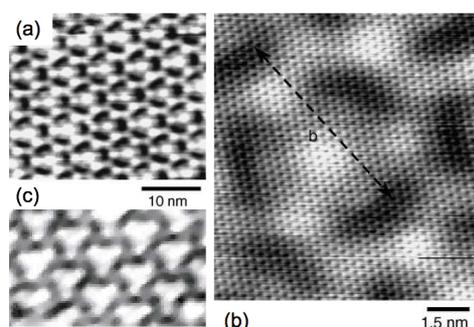

Figure 6. Multilayer Ag film on Ru. (a) Image of a 4 ML Ag film shows the trigon structure present at the first Ag layer visible through its stress field. (b) Atomically resolved image shows the trigon unit cell has 27 atomic rows. (c) The trigon structure can still be perceived in the 6 ML film albeit the decreased contrast.

Observation of the heterophase interphase structure is more difficult in the Au film on Ru. Figure 7 shows an STM image of the surface of a multilayer Au island on Ru. Atomic resolution image shows that the surface shows a surface reconstruction in the stripes of fcc and hcp sites. The same trigon network likely exists at the interface between Au and Ru and the superposition of the interface trigon structure and the surface stripe gives rise to the complicated pattern observed.
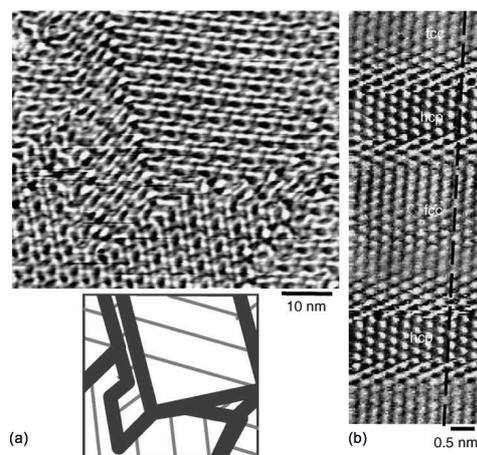
Figure 7. Multilayer Au island on Ru. (a) Scanning tunneling microscopy of the surface of a Au island shows a superposition of the trigon phase and the stripe phase. The cartoon shows the orientation of the multiple stripe domains in the image. Trigons can be recognized at the boundaries of the strip domains (wide lines in cartoon). (b) Atomic resolution image of the stripes on the surface layer. The undulation along the straight dotted line across the stripes comes from the stacking switches between fcc and hcp regions. The narrower stripe is assigned to hcp since this stacking has a higher energy on a bulk Au(111) surface.

We have shown with examples of the Au, Ag, and AuAg alloy on Ru that large in-plane misfit in heteroepitaxial films can be efficiently relieved by well-ordered dislocation networks. Understanding such dislocation structures has proved important in the development of surface structures to achieve physical or chemical properties for different applications.[5]

Publications :
    --- Ling, W.L., de la Figuera, J., Bartelt, N.C., Hwang, R.Q., Schmid, A.K., Thayer, G.E., & Hamilton, J.C.
    "Strain relief through heterophase interphase reconstruction: Ag(111)/Ru(0001)"
    Physical Review Letters 92, 116102 (2004)
    --- Ling, W.L., Hamilton, J.C., Thürmer, K., Thayer, G.E., de la Figuera, J., Hwang, R.Q., Carter, C.B., Bartelt, N.C., & McCarty, K.F.
    "Herringbone and triangular patterns of dislocations in Ag, Au, and AgAu alloy films on Ru(0001)"
    Surface Science 600, 1735-1757 (2006)

1.2. Dynamics in hetero-epitaxial films

Heteroepitaxy often yield 3-dim islands, which have a lower free energy than a uniform film.[6] Heteroepitaxial films therefore often de-wet to form 3-dim islands, exposing the bare substrate or leaving a thin wetting layer. Nonetheless, formation of 3-dim islands requires diffusion of material from thinner to thicker film regions and involves a large free-energy barrier in new-layer nucleation.[7,8] How uniformly deposited films transform into 3-dim islands was little understood. Using LEEM, we studied the de-wetting process with the Ag and Cu on Ru(0001) systems, which both follow the Stranski-Krastanov growth mode and form 3-dim islands on a wetting layer of 3 ML Ag and 2 ML Cu, respectively.

Low energy electron microscopy images the surface of a sample in real time through a beam of low-energy electrons reflected from the sample. Atomic steps and different phases can be recognized through various contrast mechanisms. For instance, by forming a dark field image from a first-order diffraction spot of the hcp Ru, adjacent terraces separated by single steps or double steps can be distinguished. On the other hand, quantum size effect gives rise to a unique intensity variation as a function of the electron energy for different film thickness and thus allows the determination of local film thickness up to 20 ML.[9–11] Low-energy electron microscopy allows the monitoring of the sample surface during material deposition or temperature change, etc., which makes it an invaluable tool for studying surface dynamical processes.

We found that the film morphology depends critically on the Ru surface topology when more than 2 ML Ag is deposited onto Ru(0001). Figure 8 shows LEEM images that compare annealed Ag films on stepped and flat Ru surfaces. The importance of substrate steps on de-wetting of the Ag film is immediately evident from these images. On the stepped region, local film-thickness determination shows multi-layer islands of over 20 ML thick surrounded by a 3 ML Ag film. On the contrary, on the flat Ru regions, no 3-dim islands were observed.
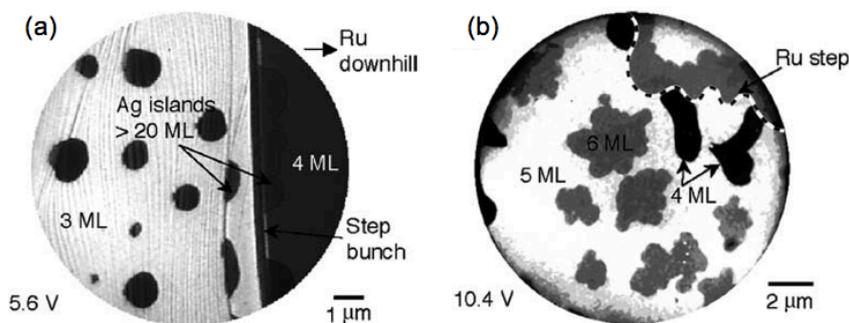

Figure 8. Low energy electron microscopy (LEEM) images of 5 ML Ag deposited and annealed to 350 °C on different Ru(0001) substrate regions. (a) Ag forms 3-dim islands on stepped substrate region. Tall islands are found at the foothill of the step bunch, which separates the stepped region on the left from a flat region on the right. (b) Only three layers of consecutive thickness is found on the flat substrate region.

Thickening of 3-dim islands would seemingly require nucleation of new layers on top of islands. Defects such as dislocations or surface steps often play a role in overcoming the nucleation barrier for new layers during crystal growth. However, analysis by LEEM showed that the islands retained a single flat (111) facet on the top, free of surface steps or dislocations. The thickening of the Ag islands therefore does not involve surface defects but Ru substrate steps.

We used LEEM to follow the surface evolution of Cu films in real time. Figure 9 shows snapshots from LEEM imaging during the de-wetting of a Cu film. A small Cu island, formed during deposition, is found on the upper right corner of the 0-min image. The subsequent images show how, when the film is annealed, this island gains mass from the surrounding film and strikingly, gains atomic layers as it moves down the Ru substrate steps. Because the island always has a flat top during the downhill migration, its front tip gains atomic layers each time it crosses a descending substrate step. This mechanism is illustrated in Figure 10. As the islands descend the substrate staircase, materials on the trailing edges of the island diffuse towards the front end, transferring materials from low atomic layer regions in the island to higher atomic layer regions and lowering the free energy correspondingly. Such self-diffusion can proceed through the edges of the moving island and does not require new layer nucleation.
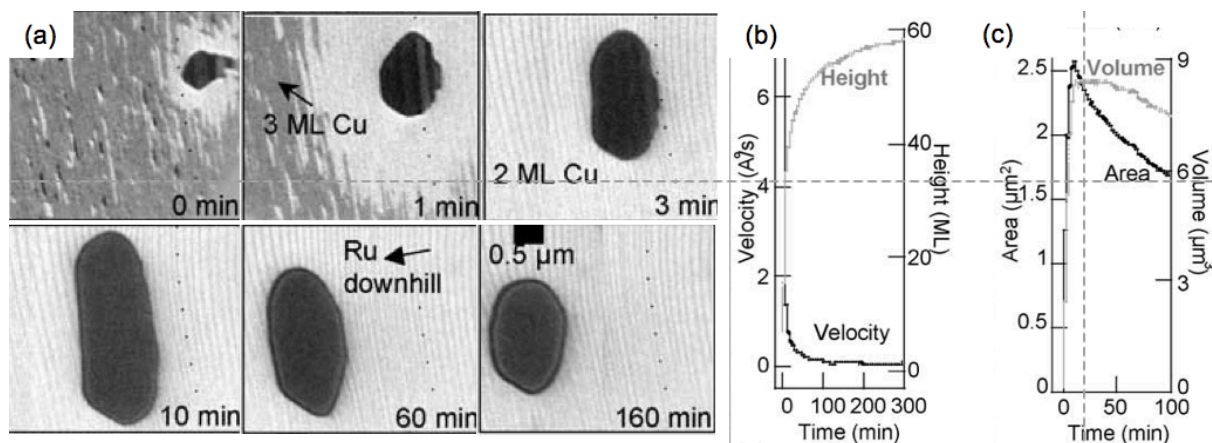
Figure 9. *Post-deposition 3-dim growth of a Cu island on Ru(0001) at 600 °C. (a) Snapshots of a LEEM movie capturing the Cu island migrating 2.5 μm in 2.5 h down around 30 double atomic-layer Ru substrate steps, thereby increasing its height by nearly 60 ML. The dotted line marks the same Ru substrate step edge in each frame. (b) Speed of the island and its height as a function of time. (c) Volume and surface area of the island as a function of time. The volume increases initially as the island consumes the surrounding Cu, then stays constant while the island grows taller. The volume finally decreases as its atoms diffuse to thicker islands outside the field of view during ripening.*
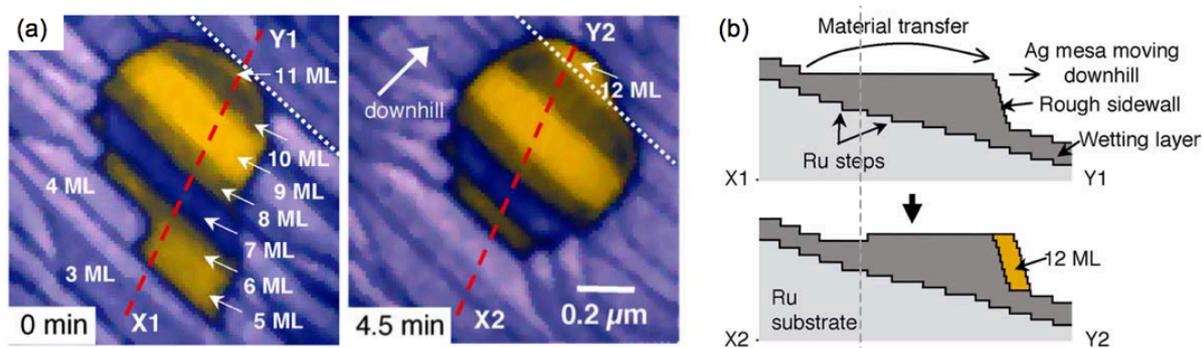
Figure 10. *Downhill migration during de-wetting. (a) A Ag mesa advances across a Ru step edge (white dotted line). (b) Schematic cross section along red dotted line in a. Atoms from the 5 ML 'tail' is transferred to the rough sidewall at the head of the island to form a 12-ML-thick film region (yellow).*

Our findings point out that Ag follows a layer-by-layer growth on large Ru terraces free of substrate steps. We have further found that Ag films grown on large step-free Ru terraces not just have minimal surface roughness, they are also free from twin boundaries, an important microstructural defect. As discussed in the previous section, stress coming from the lattice mismatch between Ru and Ag is effectively relieved by a dislocation network that resides at the interfaces beneath the second Ag layers. The second layer Ag is thus a defect-free substrate for the growth of subsequent Ag layers.

Random nucleation of the third Ag layer gives rise to two stacking sequences. Figure 11 shows the evolution of these randomly nucleated stacking sequences. When these film regions meet, a twin boundary is formed. Nevertheless, we have observed that the twin boundaries move with surface steps when the fourth layer of Ag is deposited, giving rise to regions of over 10 μm that are free from twin boundaries (Figure 11). Desorption experiments show that the stacking in underlying Ag layer has indeed been converted during film growth. Our results show that microstructural defect such as twin boundary can be coupled to film surface step during growth, a connection that has not been considered before.
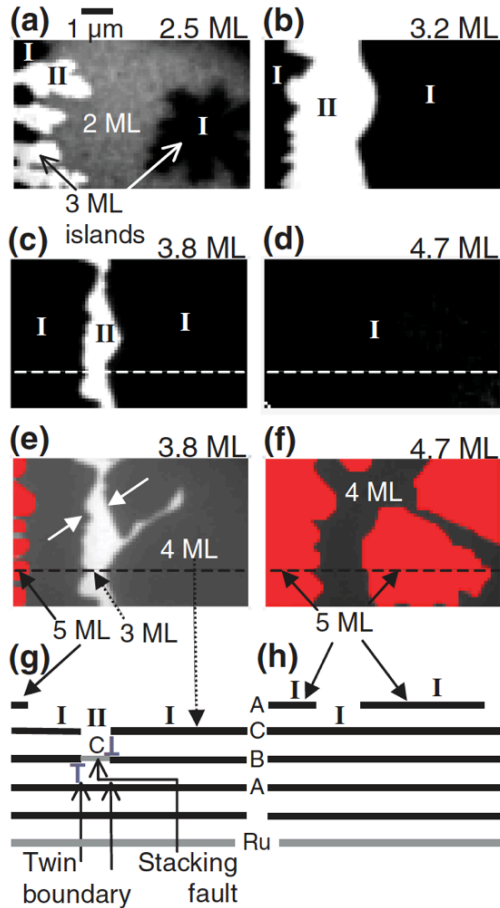
Figure 11. Elimination of twin boundaries during film growth. (a-d) Changes in stacking sequence of a 3 ML Ag film during growth on a flat substrate region at 180 °C imaged by dark-field LEEM with a (01) diffraction beam. The third Ag layer nucleates randomly in the two possible stacking sequences on the second Ag layer. The two domains (black and white) are labeled I and II, respectively. By 4.7 ML, in image d, the type II stacking domain has been eliminated. (e-g) Bright field images of the growing Ag film corresponding to dark field images in c and d, respectively. Contrast in these images origins from the film thickness. The advancing step edge of the fourth layer (white arrows) in image e coincides with the twin boundary in image c. Red area denotes the 5 ML thick film regions. (g-h) Schematic cross section of the dotted line in c and e (g) and d and f (h) to show how an advancing film layer causes twin boundaries to move and change the stacking of the underlying film layers. The dislocations (marked with blue T symbols) that form the twin boundary move in concert with the fourth Ag layer advancing from the left and the right. A domain of type II stacking is eliminated as opposite twinning dislocations annihilate when the fourth layer is completed.

Besides studying the growth dynamics in epitaxial films, we studied the decay mechanism of surface islands. In particular, we studied the effect of adsorbates on surface diffusion, in other words, the change in surface structure induced by mass flow in the presence of contaminants.

We used STM and LEEM to study the effect of S on Cu(111) surface mass transport. Sulfur is a common contaminant in metals. It has been proposed that a dilute gas of Cu_3S_3 clusters exists in equilibrium with Cu and S adatoms.[12] Considering the formation energy of the clusters, the cluster density can be orders of magnitude greater than the thermal Cu adatom concentration at high S coverage. The abundance of the clusters leads to enhanced Cu self-diffusion even though the barrier for cluster diffusion is larger than the Cu adatom diffusion barrier. While ad-species such as Cu_3S_3 is difficult to observe directly, monitoring the decay of Cu islands in the presence of S have provided evidence in support of the postulate.

The Cu(111) crystal was treated with 5% hydrogen in an argon atmosphere at 950°C for one day to deplete the bulk S content and cleaned with cycles of Ne and Ar sputtering and annealing. Sulfur was dosed onto the Cu surface from a solid-state electro-chemical cell.[13] The S coverage (θ_S) was determined by a mass spectrometer calibrated against the saturated S coverage on the Cu(111) surface.[14] The effect of S on Cu island decay and the ripening of deposited Cu island arrays was observed with LEEM and STM.

Figure 12 shows that a trace amount of S dramatically changes the surface mass transport on Cu(111). While no measurable change in the island area was observed before S exposure, the island decayed completely within 8.5 min upon exposure to 14 mML S. Similar accelerated island decay is also observed with STM at low temperature. We measured the decay rate of Cu islands, taken as the inverse of the vanishing time of an island with an area of 0.2 μm^2, as a function of θ_S at fixed temperature T. A fit to the decay curve (Figure 12) suggests that the increase in the decay rate is proportional to θ_S^3, consistent with a mass-carrying species that contains three S atoms.

11

While our results support the existence of Cu_3S_3 clusters, we found unexpectedly three regimes of Cu island decay kinetics as a function of θ_S. Figure 13 shows the island area evolution for the three regimes. For very low θ_S (the clean Cu limit) and high θ_S, the decay follows approximately $-t^{2/3}$ expected for diffusion-limited decay.[15] However, for intermediate θ_S, island area decays linearly with time.
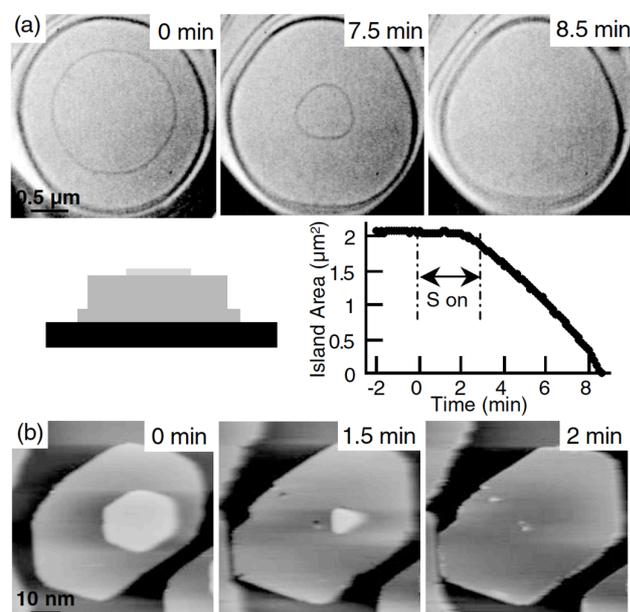

Figure 12. *Trace amount of S drastically speeds up self-diffusion on Cu(111). (a) Imaging by LEEM shows the decay of a monolayer high Cu island (innermost circle) at 215°C after exposure to 14 mML S. The diagram illustrates the configuration of the decaying Cu island (light grey) on top of a thick Cu stack (dark grey) sitting on the wetting layer (black). The island area is plotted as a function of time that shows its rapid decay after S is introduced. (b) Scanning electron microscopy results show similar speedup in the decay of a Cu island at -60°C after exposure to ~5 mML S. The Cu island shape changed from hexagonal to triangular during the decay as shown in both LEEM and STM observations, though the phenomenon is more pronounced in the STM images because of the lower temperature. The shape change is due to the preferential decoration of S at the {100} microfacet step edges.[16]*

Similarly, we found that the coarsening kinetics of 2-dim Cu island arrays fall into three regimes as a function of θ_S and T. As illustrated by the example shown in Figure 13, 2-dim coarsening proceeds by Ostwald ripening in the clean Cu regime, with big islands growing at the expense of smaller ones around.[17] As θ_S or T increases, Oswald ripening is no longer observed. Instead, all islands shrink and mass is transferred to distant step edges. As θ_S or T increases further, Ostwald ripening is once again observed.
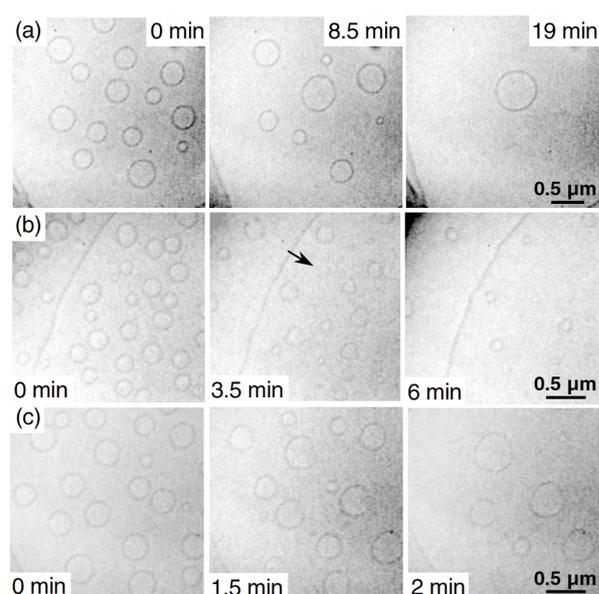
**Figure 13.** *Three coarsening regimes of Cu islands observed by LEEM. (a) Clean Cu. Ostwald ripening is observed with one big Cu island left at 10 min. (b) With 11.8 mML S. No Oswald ripening is observed. Material from islands is added to the step, which advances to the right on the lower terrace in the direction of the arrow. (c) With 12.3 mML S. Oswald ripening is observed at an accelerated rate.*

The intermediate regime with a linear island decay rate and the absence of Oswald ripening likely associate with an attachment-detachment limited kinetics.[15,18] The energetic barrier responsible for such kinetics could arise if it is difficult for clusters to decompose at the step edge. Nonetheless, the reversal to the diffusion limited kinetics at high θ_S or T is not obvious as increased amounts of S would not make it easier for clusters to decompose at step edges.

Instead, we propose that the Cu_3S_3 clusters do not attach directly at the step edges but decompose on terraces. The released Cu adatoms then attach to step edges with no barrier, as on the clean surface. If the reaction rate of cluster creation/destruction is very small (clean Cu limit with very low θ_S or T), the density of Cu_3S_3 clusters will be small and Cu monomers will be the dominant active species on the surface. When θ_S or T increases, the rate limiting process is the reaction between S and the Cu adatoms detaching from the step edge to form clusters. The flux between steps increases and is independent of the distances of the step edges for step edges further away than the diffusion length of Cu adatoms. This case is similar to the attachment-limited kinetics. No ripening occurs as the distance to neighboring step edges does not limit mass flow. When θ_S or T increases even further, the cluster formation rate is so fast that the cluster concentration near the step edge is in equilibrium with the step edge. The Cu_3S_3 clusters overtake the Cu monomers as the dominant mass transport agents and transport is limited by the diffusion rate of the clusters.

The terrace-reaction-limited kinetics at intermediate θ_S or T has not been considered before. The terrace-reaction rate determines overall surface mass transport rate as complex species, such as the Cu_3S_3 cluster, that can efficiently carry mass between step edges do not necessarily attach easily at step edges. Our work shows that it is important to consider where the complex species are formed in such cases.

Publications:
--- Ling, W.L., Giessel, T., Thürmer, K., Hwang, R.Q., Bartelt, N.C., & McCarty, K.F.
 "Crucial role of substrate steps in de-wetting of crystalline thin films"
Surface Science 570 (3): L297-L303 (2004)
--- Ling, W.L., Bartelt, N.C., Pohl, K., de la Figuera, J., Hwang, R.Q., & McCarty, K.F.
 "Enhanced self-diffusion on Cu(111) by trace amounts of S: chemical-reaction-limited kinetics"
Physical Review Letters 93, 166101 (2004)
--- Ling, W.L.*, Bartelt, N.C., McCarty, K.F., & Carter, C.B.
 "Twin boundaries can be moved by step edges during film growth"
Physical Review Letters 95, 166105 (2005)
--- El Gabaly, F., Ling, W.L., McCarty, K.F., & de la Figuera, J.
 "The importance of threading dislocations on the motion of domain boundaries in thin films
Science 308 (5726): 1303-1305 (2005)

Chapter 2. Nanocrystal structure by electron tomography

2.1 Vitreous sections of *in vivo* nanocrystals

After my first postdoctoral fellowship on surface phenomena of epitaxial films of a few monolayers grown *in situ*, I pursued a second postdoctoral fellowship that involved 3-dim reconstruction of thicker biological samples in their native hydrated state. The work was carried out in the laboratory of Prof. David Agard and Prof. John Sedat at the University of California at San Francisco (UCSF) medical school.

Vitrification of biological particles by liquid ethane cooled by liquid nitrogen developed in the 1980s has allowed the preservation of small particles in their solution state.[19] Subsequent analysis of the transmission electron micrographs of a homogeneous population (state-of-the-art analysis programs can also deal with samples with limited heterogeneity) of vitrified particles by single particle analysis can yield their native 3-dim structure.[20] Nevertheless, the technique only applies to a thin film solution of small particles (ranging from protein molecules to viruses).

Larger biological objects such as cells or tissues cannot be vitrified throughout its thickness by simple plunge-freezing in ethane. Besides, their thickness prevents them from being observed as a whole by transmission electron microscopy (TEM). Traditionally, such samples are chemically fixed, stained, embedded in resin and sectioned into slices of a few tens or hundreds of nanometers by ultramicrotomy for TEM imaging.[21] Such treatment inevitably introduces artifacts ranging from dehydration and dissolution of organelles.

The introduction of high pressure freezing, which combines the application of high pressure (~2 kBar) with the rapid freezing to inhibit the formation of crystalline ice, allows vitrification of samples up to ~200 µm.[22] Cryo-substitution can be performed on the cryo-fixed sample to substitute the solvent by resin at low temperature with ultramicrotomy carried out at room temperature.[23] This freeze substitution technique alleviates but do not totally eliminate the artefacts introduced in traditional chemical fixation. To be true to the native hydrated structure of the biological objects, cryo-electron microscopy of vitreous sections (CEMOVIS) can be performed.[24]

Without any chemical treatment, ultramicrotomy is performed at cryogenic temperature directly on the high-pressure frozen sample in CEMOVIS. The vitreous sections are then observed by cryo-electron microscopy without any staining. Since amorphous ice is brittle, vitreous sections contain crevasses besides knife marks from the ultramicrotomy. It is also tricky to keep the vitreous sections on electron microscopy grids. While resin sections can be floated off a water reservoir and picked up by an electron microscopy grid and remained well adhered to the grid, frozen hydrated sections need to be deposited directly onto the grids to which they have no affinity. Because of the crevasses and knife marks, structural information cannot be easily extracted from images of vitreous sections directly. Nonetheless, using electron tomography, structures in the interior of the vitreous sections away from the surface artefacts can be extracted.

I applied the technique of CEMOVIS and cryo-electron tomography to probe the organelle structures in Chlamydomonas cells provided to us by Prof. Wallace Marshall. Projection of the vitreous section in the transmission electron micrograph shows crevasses from sectioning as well as ice contamination accumulated between the sectioning and the cryo-TEM observation (Figure 14). Nonetheless, reconstruction of the tilt series acquired reveals the internal structure of the pyrenoid, showing the quasi-crystalline packing of the RuBisCO. The results confirm that CEMOVIS is a promising technique capable of visualizing organelles of eukaryotes in their native environment to nanometer resolution, complementary to other imaging techniques.
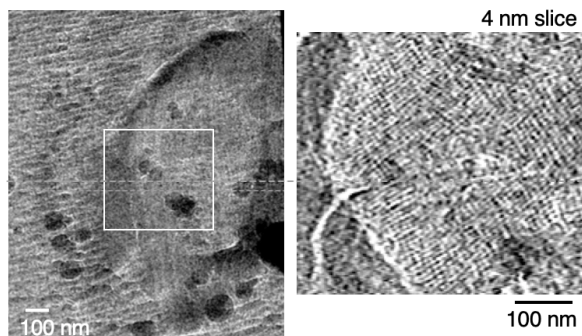
Figure 14. Cryo-section of a Chlamydomonas cell preserved by high pressure freezing. Ice crystal contamination from the transfer of the cryo-section to the microscope is abundant (dark round features, especially on the lower half of the field of view). Crevasses (elongated features throughout image) mask the structural information of the sample but the most prominent organelle, the pyrenoid, can be recognized. Tomography was performed on this cryo-section and a 4 nm central slice of the boxed region (lower left corner of the pyrenoid) from the tomogram is shown on the right. It shows that the tear by the crevasse has went through the thickness of the section (lower left corner). Nevertheless, the protein ordering in the pyrenoid is evident from the reconstructed tomogram.

Besides eukaryotic cells, the technique can be applied to thick samples that need to be kept hydrated. Examples include polymers or lipid structures. The technique CEMOVIS will also be useful for the studies of protein crystals by electron crystallography, as will be discussed in Section II.

2.2 Core-shell structure of crystalline nanospheres

I moved to France after one year at the UCSF and started working in a collaboration between the IBS and CEA/LETI when colloidal nanoparticles started to become an important element in optoelectronic or bio-labelling applications. Techniques applied to solid state objects traditional in materials science were not applicable to sample preparation for particles in solution. Applying techniques used in biology, we prepared these nanoparticles for TEM studies. Nevertheless, since these nanoparticles have multiple components and a complex structure, conventional imaging is not sufficient for their structural studies.

Electron tomography, a technique applied to biological samples, was not common in material science because material science samples most often contain crystalline components, which give rise to diffraction contrast. Transmission electron micrographs of these samples are thus no longer simple projections that can be used for tomographic reconstruction. To overcome this problem, scanning TEM (STEM) coupled with a high angle annular dark field (HAADF) detector was used to collect tilt series for tomographic reconstruction of these nanoparticles.[25]

An HAADF detector form an annulus around the electron beam and captures high angle (>40 mrad), incoherently scattered electrons to produce a dark field image. These electrons are Rutherford scattered from the nucleus of the atoms in the sample and varies roughly as the squared of the atomic number Z. Since Rutherford scattered electrons are collected, diffraction contrast from Bragg scattered electrons is avoided and tilt series closer to true projections can be collected.

The experiments were performed on a Titan scanning TEM (STEM). Besides a HAADF detector, it is also equipped with a Cs corrector, energy dispersive X-ray spectroscopy (EDS), and a Gatan imaging filter (GIF) for energy filtering and spectroscopy. The Cs corrector cancels the spherical aberration of the condenser lens to yield a smaller, higher-intensity probe, which allows a higher-resolution HAADF imaging and elemental analysis.

We used STEM HAADF tomography to analyze functionalized silica nanoparticles prepared by Dr. Olivier Raccurt. The condensed electron probe is scanned across the sample and an image is built up using the intensity of scattered electrons collected by the HAADF detector at each spot. The high sensitivity to the variation in Z of the HAADF detector together with the small probe allows precise localization of heavy elements in the silica matrix. To reduce damage induced by the strongly focused beam, we cooled the sample down to liquid nitrogen temperature using a cryo-tomography holder. Contamination was significantly reduced under cryo-condition and tilt series were collected. Figure 15 shows a section from the reconstructed tomogram of a cluster of multi-shell silica nanoparticles we examined. Instead of a uniform layer with Cu ions, the results show an uneven distribution of chelated Cu ions distributed in a porous shell around the silica core.

50 nm
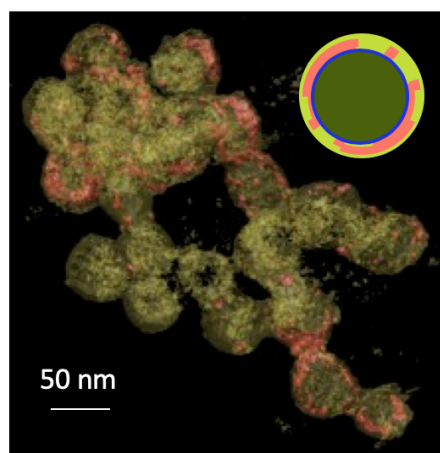
Figure 15. Three-dimensional volume of a cluster of multi-shell nanoparticles with segmentation with two threshold values corresponding to the silica (olive) and the Cu ions (salmon). The cartoon shows a schematic drawing of the nanosphere structure found in the reconstruction.

Publications:

--- Samuel, J., Tallec, G., Cherns, P., Ling, W.L., Raccurt, O., Poncelet, O., Imbert, D., and Mazzanti, M.
"Lanthanide-chelate silica nanospheres as robust multicolor Vis-NIR tags"
Royal Society of Chemistry Journal of Chemical Communications 46, 2647-2649, (2010)
--- Samuel, J., Raccurt, O., Poncelet, O., Auger, A., Ling, W.L., Cherns, P., Grunwald, D., and Tillement, O.
"Surface characterizations of fluorescent-functionalized silica nanoparticles: from the macroscale to the nanoscale"
Journal of Nanoparticle Research 12, 2255-2265 (2010)
--- Ling, W.L.*, Cherns, P., Samuel, J., Raccurt, O., Poncelet, O., Chabli, A.
"Z-contrast cryo-electron tomography probes shell porosity in multi-shell nanocomposites"
Journal of Nanoparticle Research 14 (4), 806-812 (2012)

Chapter 3. Interaction of complement proteins with organic and inorganic nanoparticles

3.1. C1q in pathogenesis

The complement system is an important component of the innate immune system. Complement was first discovered as a system complementary to the action of antibodies. The protein C1q, part of the protein complex C1 (first complement protein), recognizes bound antibodies and activates the complement cascade through the classical complement pathway.[26] C1q has also been found to bind some pathogens and activate complement directly in innate immunity through recognition of common charge motifs found in pathogens. Besides the classical pathway, the complement can also be activated through two other pathways, namely, the lectin and the alternative pathways.

Apart from humoral immunity, C1q is involved in many important physiological and pathological processes.[27] Structurally, C1q resembles a bouquet; a collagen stem branches out into 6 arms, which each terminates in a globular head domain gC1q, which can bind to a wide range of substrates.[28] For instance, C1q binds altered-self materials and is involved in apoptosis. Binding of C1q may or may not trigger complement activation. Specific bindings that triggers activation have been postulated to involve the Ca^{2+} ion found at the apex of the gC1q. C1q is also expressed in the nervous system and is involved in synaptic trimming. The protein also plays a role in pregnancy and cancer. We were interested particularly in its role in atherosclerosis and prion disease.

Atherosclerosis is the arterial inflammation that precedes plaque development.[29] The chronic inflammatory condition is caused by the accumulation of low-density lipoproteins (LDL) in the extracellular matrix of the blood vessels.[30] The LDL particles are modified by enzymes into E-LDL, which are then oxidized by oxidative agents in the arterial intima and transformed into lipid droplets and vesicles during the early stages of atherogenesis.[31]

The complement system plays an important role in atherosclerosis. Experiments have shown that E-LDL efficiently activates C1 and that C1q binds E-LDL particles with high affinity.[32] Figure 16 shows electron micrographs visualizing the interaction between C1q and E-LDL prepared in the laboratory of Dr. Gerard Arlaud by Dr. Adrian Biro. Bound C1q clearly interacts with E-LDL particles through their globular heads. The globular domain gC1q likely possesses a binding site for carboxyl group in un-esterified fatty acids in E-LDL generated upon cholesterol esterase treatment of LDL. The binding of C1q may control the pro-apoptotic effect of E-LDL. Given that endothelial cell apoptosis is involved in the atherogenesis process, the results may have important implications to atherogenesis.[33]
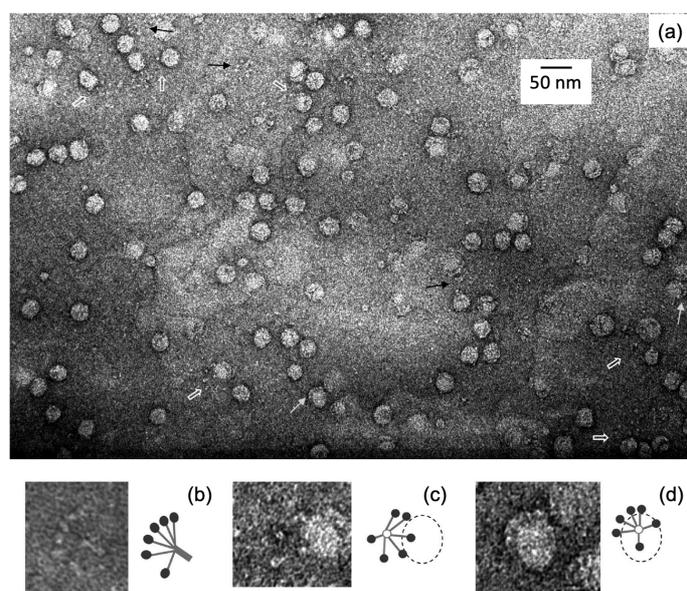
Figure 16. *Transmission electron micrograph of E-LDL bound to C1q molecules. Particles of E-LDL was preincubated with C1q for 30 min at 37°C. Samples diluted and stained with 2% uranyl acetate. (a) Large field of view. C1q molecules bound to the E-LDL particles with fewer than 6 globular heads and with all 6 heads are indicated by open and filled white arrows, respectively. Black arrows point to C1q molecules lying close to E-LDL particles, possibly detached during sample preparation. (b) Free C1q molecule. (c) Close-up of a C1q molecule bound to an E-LDL particle with a few heads. (d) A bound C1q molecule with its globular heads following the curvature of the E-LDL particle.*

Prion diseases are transmissible neurodegenerative disorders that occur when cellular prion protein (PrP[c])[2] is converted into abnormal isoform PrP[Sc].[34] The abnormal isoform PrP[Sc] has an increased beta-sheet content and tends to form aggregates, which can further assemble into amyloid fibrils. PrP[Sc] aggregates are resistant to protease degradation and have very different physiochemical properties from natively folded PrP[c]. It has been reported that the smallest aggregates that can initiate spongiform encephalopathies pathology contains 14-28 PrP molecules.[35]

C1q has been found to bind amyloid fibrils found as extracellular deposits in tissues and complement activation has been found to be involved in the pathology of various amyloid diseases, including Alzheimer's disease.[36] Besides contributing to neuronal damage in the end stages of prion diseases, complement activation is also thought to contribute to the infection, dissemination, and replication stages.[37] Mouse model has shown that C1q is one of the top proteins up-regulated in the brain with prion diseases.[38]

In collaboration with Dr. Jean Gagnon, we observed the interaction between C1q and PrP beta-oligomers with electron microscopy (Figure 17). Whereas gC1q has a diameter of about 4 nm, the gC1q regions on C1q molecules incubated with PrP oligomers appear much larger, with a diameter of around 8 nm, corresponding to the size of PrP oligomers. The images suggest that C1q binds PrP beta-oligomers through gC1q. Since each of the six gC1q on a C1q molecules can bind to an oligomer, C1q binding may contribute to the aggregation of the oligomers and the progression of the disease. On the other hand, C1q binding may play a role in the clearing of the oligomers. Further investigation will be necessary to determine the precise effect of C1q in prion diseases.
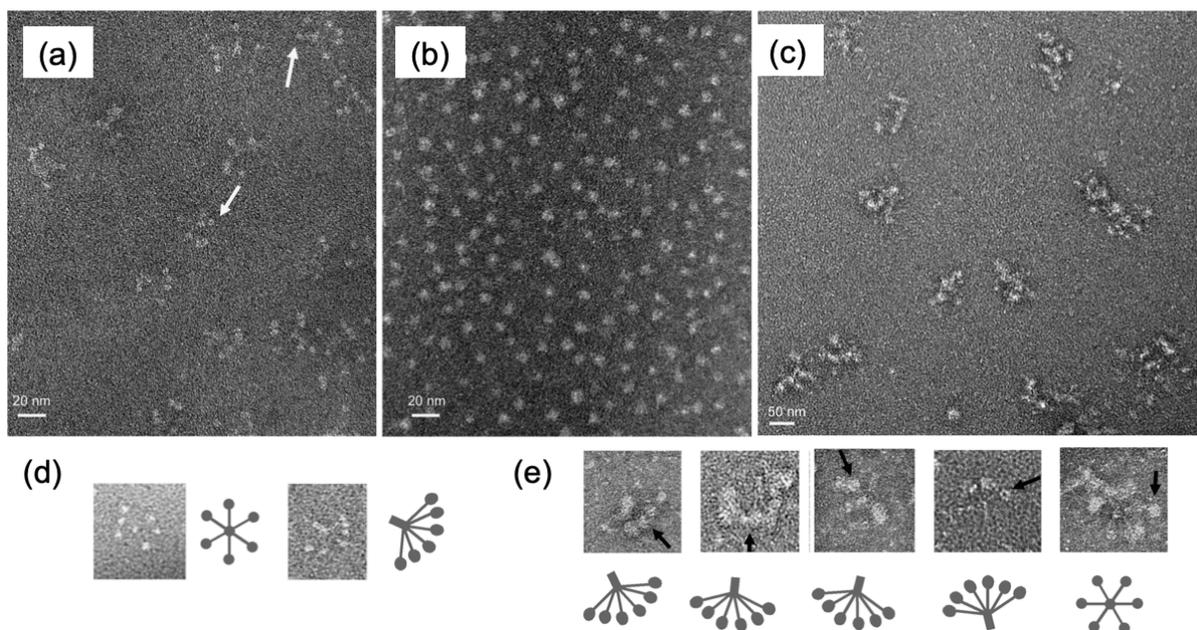
Figure 17. Transmission electron micrographs of C1q, PrP type II oligomers, and C1q-PrP complexes stained with 2% uranyl acetate or 1% ammonium molybdate. (a) C1q purified from human serum. White arrows point to globular head domains of C1q of ~4 nm. (b) PrP type II oligomers purified by SEC. The oligomers have a diameter of 5-8 nm. (c) A SEC fraction of C1q-PrP complex. (d) Top view and side view of C1q. (e) Side views and top view of purified C1q-PrP complexes. Black arrows point to examples of PrP bound to globular domains of C1q.

Publications:

--- Chouquet, A., Paidassi, H., <u>Ling, W.L.</u>, Frachet, P., Houen, G., Arlaud, G.J., Gaboriaud, C.
"X-ray structure of the human calreticulin globular domain reveals a peptide-binding area and suggests a multi-molecular mechanism"
PLoS ONE 6(3): e17886. doi:10.1371/journal.pone.0017886 (2011)
--- Arlaud, G. J., Biro, A., <u>Ling, W.L.</u>
"Enzymatically modified low-density lipoprotein is recognized by C1q and activates the classical complement pathway"
Journal of Lipids vol. 2011, Article ID 376092, 5 pages, 2011. Doi:10.1155/2011/376092 (2011)
--- Erlich, P., Dumestre-Pérard, C., <u>Ling, W.L.</u>, Lemaire-Vieille, C., Schoehn, G., Arlaud, G., Thielens, N.M., Gagnon, J., & Cesbron, J.-Y.
"Complement protein C1q forms a complex with cytotoxic prion protein oligomers"
Journal of Biological Chemistry 285, 19267-19276 (2010)
--- Biro, A., <u>Ling, W.L.</u>, Arlaud, G. J.
"Complement protein C1q recognizes enzymatically modified low-density lipoprotein through unesterified fatty acids generated by cholesterol esterase"
Biochemistry 49, 2167-2176 (2010)

3.2 Interaction of carbon nanoparticles with the human complement

This project started as an exploration of using carbon nanotubes as a support to grow helical arrays of proteins for their 3-dim structural determination as a collaboration between the IBS and Dr. Doris' laboratory in CEA, Saclay. Whereas we have shown that various proteins do organize on arc-discharged multiwalled carbon nanotubes, these arrays are not well-organized enough to be exploited for 3-dim structural analysis (Figure 18). On the other hand, the health effect of carbon nanotubes, a common type of industrial nanoparticles, is not well understood. The project thus evolved to become an investigation on the interaction of carbon nanotubes and other nanoparticles with C1q and the complement system. The project was a multidisciplinary effort, which involved chemists in Dr. Doris's group from CEA, Saclay, immunologists from Dr. Thielens' group in IBS/IRPAS, and physicists from Dr. Mingo's group in CEA/LITEN.
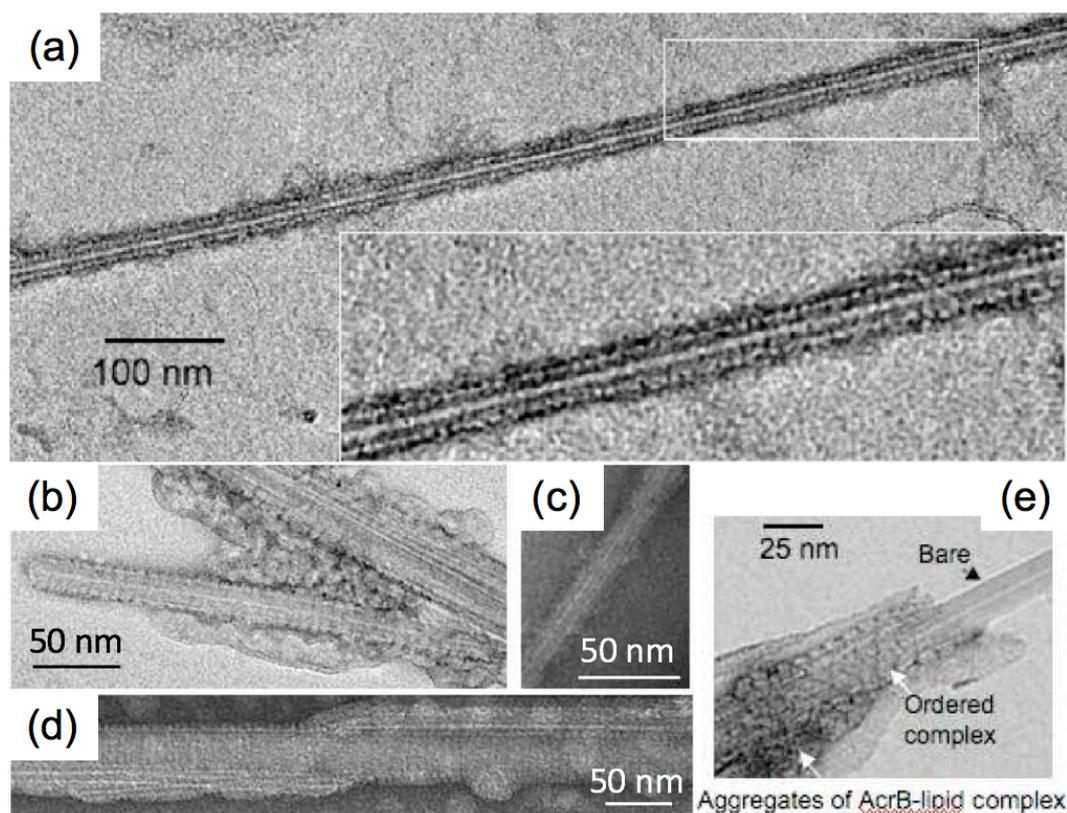
Figure 18. Organization of various proteins on arc-discharged multi-walled carbon nanotubes. (a) C1q attaches onto the nanotube through its globular head domain. Inset shows a detail view of the boxed area. (b) Calreticulin molecules aggregate around the nanotubes covered by calreticulin molecules. (c) Green fluorescent protein on carbon nanotube. (d) A soluble protein purified from the Acanthamoeba polyphaga Mimivirus on several joined carbon nanotubes. (e) Array of complex formed by membrane protein AcrB with lipid covers part of the nanotube.

Carbon nanomaterials, specifically, carbon nanotubes and nanodiamonds, have various potential clinical applications due to their exceptional biological, physical and chemical properties.[39–44] Safety of such potential nanomedicines have mainly focused on *in vivo* murine models and *in vitro* cellular toxicity.[45–53] Since many of these applications involve introducing the nanomaterials into the bloodstream or into the brain, where the recognition protein of the classical pathway of complement C1q is found, it is important to understand the response of C1q towards these nanomaterials. Inappropriate activation of the complement can lead to inflammation and tissue injury with detrimental consequences.[54] Since the complement system is highly species-specific, we investigated the interaction of various types of carbon nanotubes and nanodiamonds with C1q purified from human serum. Moreover, any binding of the multifunctional protein may deplete C1q locally and affect the many physiological processes that involve C1q.

We studied three different types of nanotube and nanodiamond samples: pristine, oxidized, and functionalized with polyethylene glycol (PEG) prepared in Dr. Doris' laboratory. These types of carbon nanotubes and nanodiamonds have been used in the development for implant coating, drug delivery, and as a neuroprotective agent against Alzheimer's disease among many biomedical applications.[41,45,55–60] *In vitro* complement activation assays carried out in IRPAS group showed that none of the nanotubes and nanodiamonds tested activate the classical pathway of complement. Nevertheless, surface plasmon resonance (SPR) showed that C1q bound to nanodiamonds and TEM results also showed binding of C1q to carbon nanotubes.

Figure 19 shows the interaction of pristine carbon nanotubes with C1q. Unlike arc-discharged multiwalled carbon nanotubes shown in Figure 18, which have little defects and are thus rigid, these carbon nanotubes fabricated by catalytic chemical vapor deposition have a high density of defect sites, which make them highly flexible. Due to their hydrophobicity, these nanotubes are bundled and entangled in aqueous buffer. Curiously, when they are mixed with C1q, the bundles dissociate into thinner bundles covered by C1q and in the case of the multiwalled carbon nanotubes, into individual nanotubes. The same phenomenon was observed with gC1q.
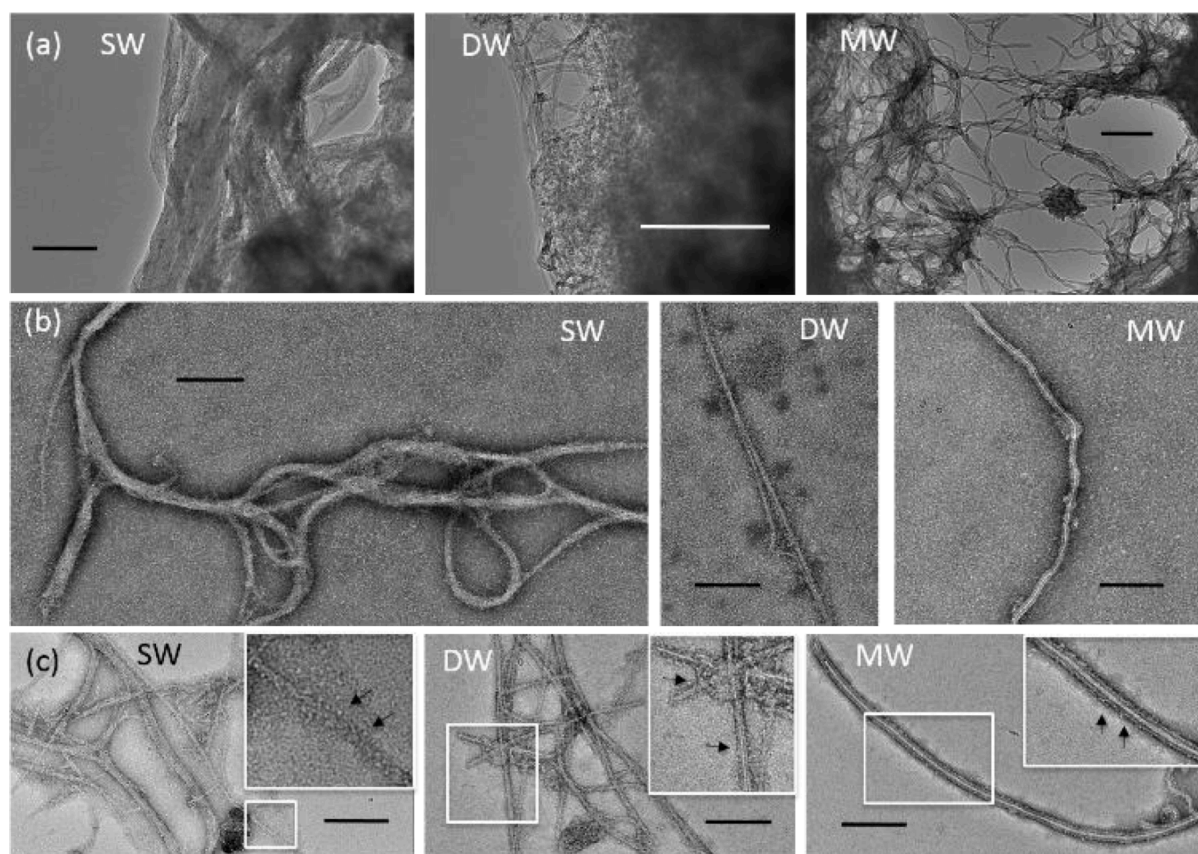
Figure 19. *Transmission electron micrographs of different types of catalytic chemical vapor deposited carbon nanotubes before (a) and after (b,c) protein adsorption. (a) Single-walled (SW), double-walled (DW), and multiwalled (MW) carbon nanotubes all appear as agglomerates of entangled bundles because of their low solubility. (b) Carbon nanotubes sonicated in the presence of C1q. (c) Carbon nanotubes sonicated in the presence of globular domains (gC1q) of C1q and resuspended in buffer without protein. The gC1q have been isolated from C1q molecules by enzymatic digestion. Insets show enlarged views of the boxed regions. Arrows in insets point to gC1q molecules adsorbed on the carbon nanotube surface. All scale bars correspond to 200 nm.*

Molecular dynamics simulations of the interactions between gC1q and the carbon nanotubes were carried out in Dr. Mingo's group at CEA/Liten. An attractive interaction was found, consistent with

the experimental results from SPR and TEM that C1q binds the carbon nanotubes. Moreover, stronger attraction was found on the side of the gC1q molecule, when the vector between the protein center and the Ca^{2+} ion was roughly parallel to the nanotube surface, whereas only very weak interaction was found when the Ca^{2+} ion at the apex of the gC1q molecule faced the carbon nanotube. As the Ca^{2+} ion has been speculated to be involved in the binding of complement activators, this finding is consistent with the results that the nanotubes did not activate complement.

The disaggregation of the carbon nanotube bundles can also be understood by the calculated free energy results with a simple model of nanotube adhesion. The energy to dissociate the bundles depend on the square root of the nanotube radius r. The energy gained by coating the nanotube with gC1q, on the other hand, depends on the square of the radius for thin nanotubes (approximated by single-walled carbon nanotubes) and linearly on the radius for larger nanotubes (approximated by graphene). The energy gained by protein adsorption and the energy cost in dissociation has a crossover at r around 25 nm, meaning that for nanotubes thinner than 25 nm, it is energetically more favorable for the nanotubes to stay bundled but for thicker nanotubes, it is more favorable to dissociate and be fully covered by proteins, consistent with the TEM observations.

We found similar C1q binding on the other carbon nanotube samples, namely, the oxidized and the PEGylated nanotubes (Figure 20). Binding of C1q on the PEGylated nanotubes seemed at odds with the fact that PEG is commonly used to evade the immune system and is considered stealth to immune proteins. As PEG functionalization depends on surface carboxylic groups generated by oxidation on carbon nanotubes, PEG is only grafted on defect sites and not the full nanotube surface. We postulated that C1q may be binding on the unmodified carbon nanotube surface and not on the PEG.
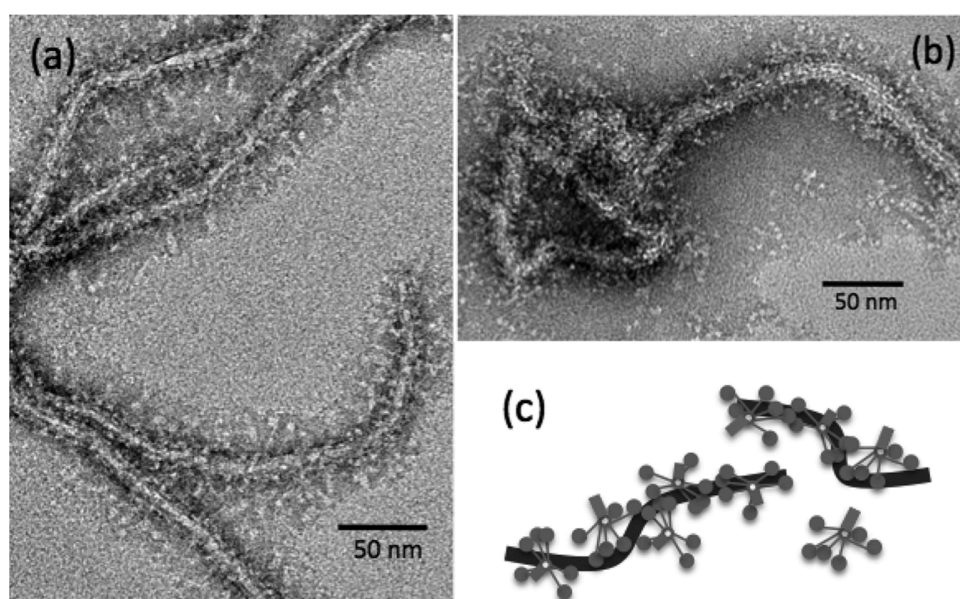
Figure 20. Transmission electron micrographs of the interaction of C1q molecules with acid treated carbon nanotubes (a) and PEG-grafted carbon nanotubes (b). (a) Unbound proteins have been removed by centrifugation and resuspension in buffer for both samples. (c) Schematic diagram (not-to-scale) of C1q molecules (grey) binding onto carbon nanotubes, depicted as thick black lines.

Carbon nanotubes fully covered with PEG were generated in Dr. Eric Doris's group to test this hypothesis. Amphiphiles incorporating a diacetylenic lipophilic chain were synthesized with PEG.[61] These molecules self-assembled on the nanotube surface as the hydrophobic portion was attracted to the nanotube surface with the hydrophilic PEG head oriented towards the aqueous phase (see Figure 21). Similar self-assembly has been observed on the carbon nanotubes.[62] To stabilize the PEG coating, the diyne motif incorporated in the lipophilic chain was photopolymerized by ultraviolet irradiation. Surface plasmon resonance testified that micelles made up of these amphiphiles do not bind C1q.

(a) lipophilic chain with polymerizable diacetylene
hydrophilic PEG

Diyne motif

aqueous solution (> CMC)

9 nm

hv (254 nm)

DA-PEG micelle   pDA-PEG micelle

(b)
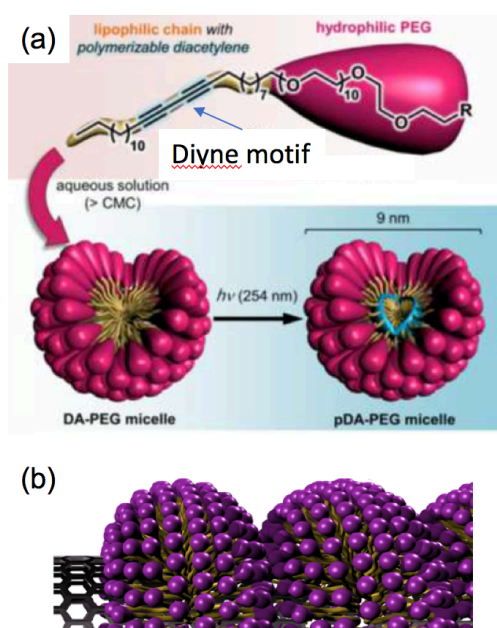
Figure 21. (a) Schematic diagram of diacetylene poly(ethylene glycol) (DA-PEG) amphiphiles. The diyne motif can be photopolymerized by ultraviolet irradiation at 254 nm to reinforce assemblies made of the amphiphiles, such as micelles. (b) Representation of supramolecular assemblies of DA-PEG amphiphiles formed on carbon nanotube surface when carbon nanotubes are sonicated in the presence of the amphiphiles. While the hydrophobic portion of the amphiphile is adsorbed onto the nanotube surface, the hydrophilic PEG head is oriented towards the aqueous phase. A region of bare nanotube surface is shown on the left for illustration purpose. In the experiments, all nanotube surface is covered by using excess amphiphiles. The supramolecular assemblies are photopolymerized to promote further stability of the PEG coating.

Figure 22 shows TEM images of the interaction of the protein C1q with carbon nanotubes with covalently grafted PEG and with carbon nanotubes fully coated with PEG assemblies. While PEGylated nanotubes with partial PEG coverage binds C1q readily, nanotubes fully covered with PEG do not attract C1q. These results support our hypothesis that C1q may be binding to uncovered carbon nanotube surface. Mode of PEG coverage thus needs to be considered for employing PEG in potential nanomedicine.
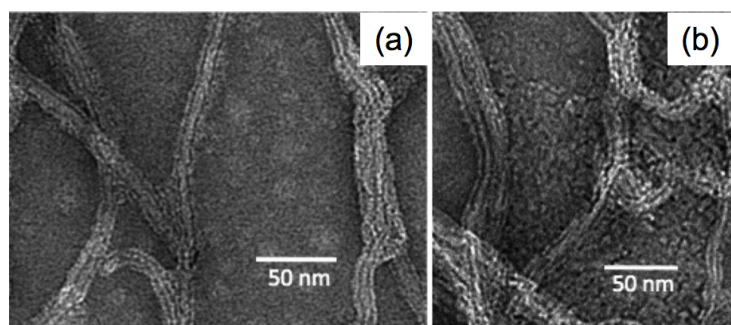
Figure 22. Carbon nanotubes fully coated with PEG incubated with C1q and resuspended in buffer without protein. (a) Carbon nanotubes show rough sidewalls from the supramolecular assembly of PEG but no bound C1q molecules. (b) Protein aggregates that are quasi-organized are found occasionally around nanotubes.

We next looked at the binding of C1q with pristine, oxidized and PEG-conjugated nanodiamonds. Unlike carbon nanotubes, nanodiamonds are relatively easy to disperse in aqueous solutions. Surface plasmon resonance studies showed that C1q binds to all the nanodiamond samples studied. Nevertheless, TEM shows that C1q binding has a different effect on nanodiamonds from that on carbon nanotubes.

Figure 23 shows pristine nanodiamonds before and after the addition of C1q. Pristine nanodiamonds form particles of around 30-100 nm made up of single crystal nanodiamonds. When the nanodiamonds are mixed with C1q, only large aggregates are found. It is difficult to discern the contents of the aggregates with negative staining. Cryo-electron microscopy was thus performed with the same mixing conditions.

A thin film of the nanodiamond with C1q sample was vitrified in liquid ethane at its freezing temperature. The frozen hydrated sample was imaged at liquid nitrogen temperature with no staining. In this case (Figure 23e), we see loosely packed nanodiamonds bridged by particles that can be recognized to be the protein C1q although the contrast is weak. We propose that the nanodiamond aggregates are due to the multivalence of the C1q molecule. Careful inspection of the negatively stained images shows C1q molecules bound to small particles with sharp edges of around 5-10 nm around the edges of big aggregates. We speculate that these small particles are single crystal nanodiamonds. From the images, we can see that the particles were bound to gC1q, the globular domains of C1q. Since each C1q molecules carry six gC1q, which can each interact with separate nanodiamonds and different facets on a nanodiamond particle can also interact with gC1q on different C1q molecules, a large agglomerate can be formed.
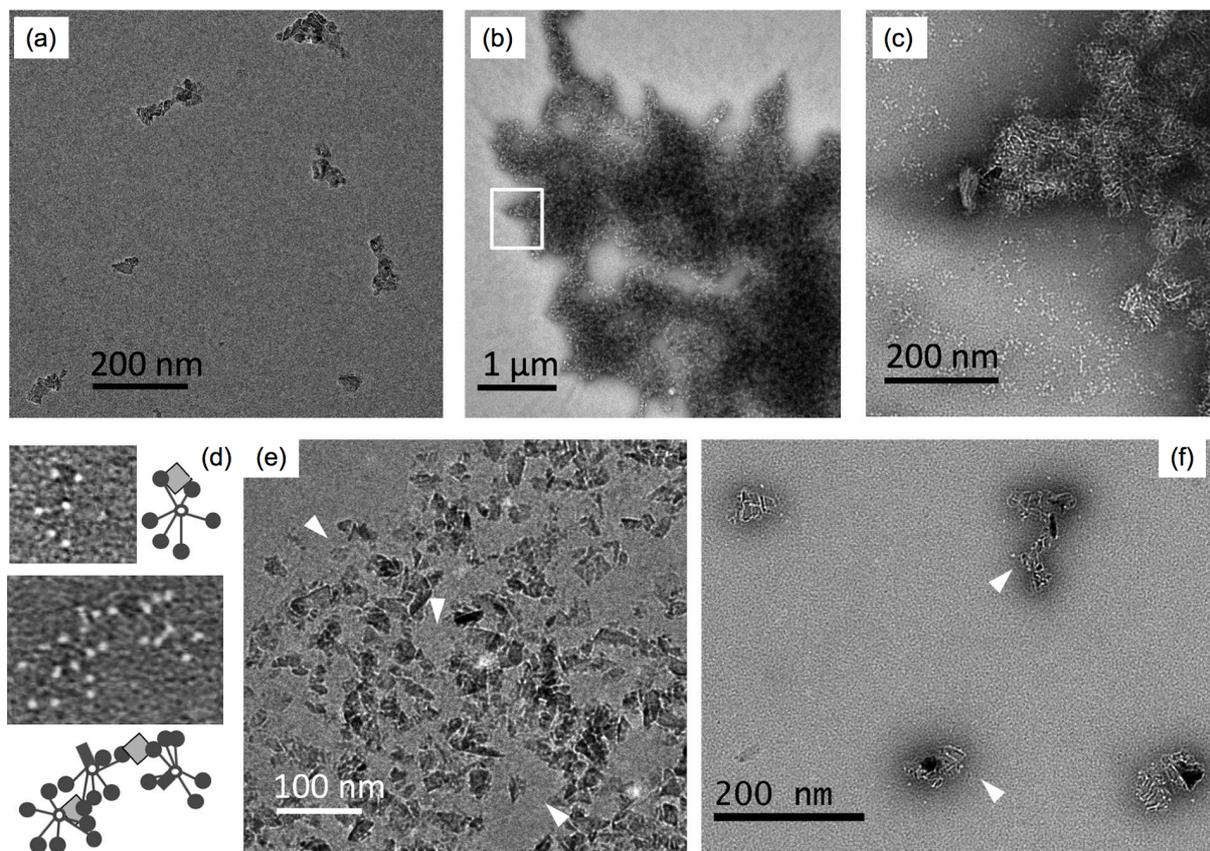
Figure 23. *Transmission electron microscopy studies of pristine nanodiamonds and their interactions with C1q and gC1q. (a) Pristine nanodiamonds form particles of size distribution of ~30-100 nm. (b) Aggregates of over 10 µm are formed when nanodiamonds are incubated with C1q. The sample is stained with 2% sodium silicotungstate. (c) Higher magnification image of boxed area in b. (d) Magnified images of some C1q molecules with bound nanodiamonds found around the large aggregates in b. Schematic diagram showing the mechanism of aggregation. Individual nanodiamond particles may bind multiple globular domains of one or more C1q molecules. (e) Cryo-electron micrograph of C1q with nanodiamonds sample prepared the same way as the sample in b but with no heavy metal staining. The image shows that the large aggregates are not solidly packed but consist of separated nanodiamond particles of ~50 nm. C1q molecules (white arrowheads) can be discerned by the clusters of globular head domains (gC1q) among the nanodiamond particles despite the low contrast in the unstained specimen. (f) Negatively stained image showing the interaction of isolated gC1q molecules with nanodiamonds. White arrowheads point to some bound gC1q on nanodiamond particles. No aggregates are observed.*

We tested this hypothesis by performing the experiments with gC1q. As shown in Figure 23f, we see gC1q bound to nanodiamond particles but no aggregates are found. Similar results were obtained with oxidized and PEGylated nanodiamonds. To test if this agglutination by C1q multivalence applies to other nanoparticles, we repeated the experiments with silica nanospheres. Figure 24 shows the results. Again, silica nanospheres were aggregated by C1q but not by gC1q alone. The results support the

25

proposition that compact nanoparticles that bind C1q may be aggregated by the multivalence of the protein.
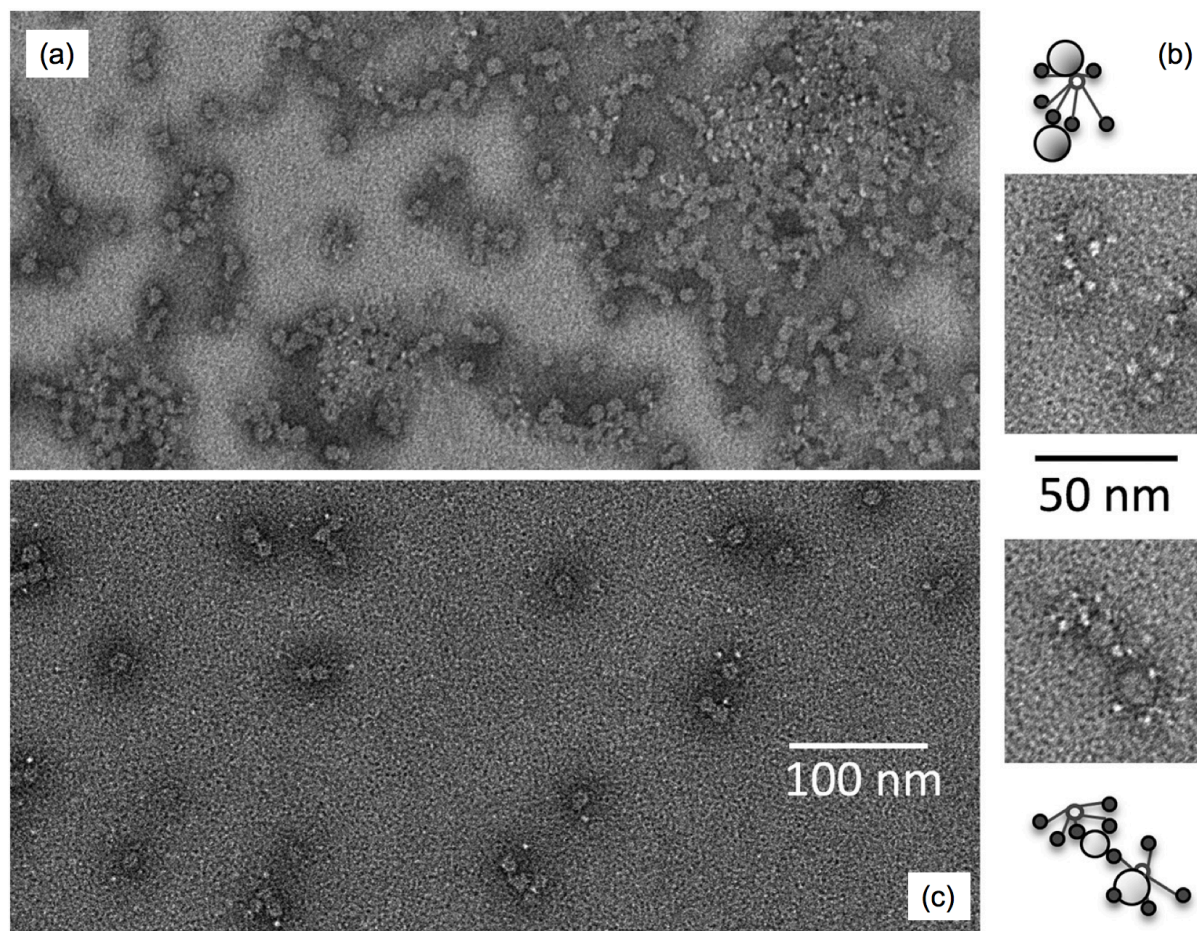
Figure 24. *Transmission electron micrographs of silica nanospheres interacting with C1q and isolated gC1q. (a) Silica nanospheres incubated with C1q molecules. Large aggregates of nanospheres are found. The globular domains of the C1q molecules can be recognized as small bright dots with regular size among the nanosphere aggregates. (b) Close-ups of small clusters of nanospheres with bound C1q molecules and their schematic representations. As globular domains from one C1q molecule can bind to different nanospheres while each nanosphere can attract multiple C1q molecules, an assembly of nanospheres can be brought together by C1q interaction. (c) Nanosphere sample incubated with isolated gC1q molecules. We find nanospheres decorated with gC1q but no large aggregates. Images a and c have the same scale.*

The examples of carbon nanotubes and nanodiamonds show that the consequence of C1q binding depends on the morphology of the nanoparticles. As illustrated in Figure 25, C1q binding is likely to agglutinate compact nanoparticles of a size comparable to the size of C1q. Such agglutination may be a way to improve the efficiency of clearing the nanoparticles from the body but such conjecture remains to be tested. Extended particles such as carbon nanotubes, on the other hand, readily offer binding sites for gC1q that belongs to the same C1q molecules. When multiple gC1q domains of the same C1q molecule bind to the particle, the collagen stem may cause steric hindrance for other interaction with the particle near the binding site. These factors need to be reckoned with for the design of nanoparticles in biomedical applications.
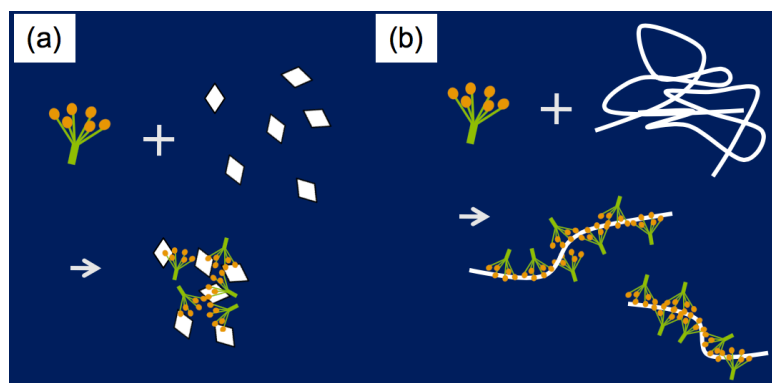
Figure 25 *Cartoons illustrating the interaction of C1q with nanoparticles of different geometry. (a) For small compact nanoparticles with size comparable to C1q and with multiple binding sites for gC1q, C1q binding can cause aggregation. (b) Elongated nanoparticles, such as carbon nanotubes, offer binding sites for multiple gC1q on the same C1q molecule. C1q binding helps to disperse the nanoparticles in this case.*

Given the extensive presence of C1q in the body and its role in diverse physiological and pathological processes, the binding of C1q on nanoparticles need to be considered for potential biomedical applications of nanoparticles. Binding of C1q may locally deplete C1q and affect the biological processes the molecule is involved in. Potential structural changes of the nanoparticles following C1q binding would also need to be taken into consideration.

Publications:

--- Ling, W.L.*, Biro, A., Bally, I., Tacnet, P., Deniaud, A., Doris, E., Frachet, P., Schoehn, G., Pebay-Peyroula, E., Arlaud, G.
"Proteins of the innate immune system crystallize on carbon nanotubes but are not activated"
ACS Nano 5, 730-737 (2011)
--- Belime, A., Gravel, E., Brenet, S., Ancelet, S., Caneiro, C., Hou, Y., Thielens, N., Doris, E., Ling, W.L.
"Mode of PEG coverage on carbon nanotubes affects binding of innate immune protein C1q"
Journal of Physical Chemistry B 122, 757-763 (2018)
--- Saint-Cricq, M., Carrete, J., Gaboriaud, C., Gravel, E., Doris, E., Thielens, N., Mingo, N., Ling, W.L.
"*Human immune protein C1q selectively disaggregates carbon nanotubes*"
Nano Letters 17, 3409-3415 (2017)
--- Belime, A., Thielens, N.M., Gravel, E., Frachet, P., Ancelet, S., Tacnet, P., Caneiro, C., Chuprin, J., Gaboriaud, C., Schoehn, G., Doris, E., Ling, W.L.
"Recognition protein C1q of innate immunity agglutinates nanodiamonds without activating complement."
Nanomedicine: Nanotechnology, Biology, and Medicine (in press)
--- Thielens, N., Belime, A., Gravel, E., Ancelet, S., Caneiro, C., Doris, E., Ling, W.L.
"Impact of the surface charge of polydiacetylene micelles on their interaction with human innate immune protein C1q and the complement system."
International Journal of Pharmaceutics 536, 434-439 (2018)

Chapter 4. Single particle analysis of the helicase domain of vaccinia virus helicase-primase D5

The vaccinia virus belongs to the Poxviridae family as the variola virus, which causes smallpox. The vaccinia virus represents the prototypic virus of the Orthopoxvirus genus and shares more than 97% sequence identity with the poxvirus variola virus. Even though smallpox has been declared eradicated in 1979 by the worldwide vaccination campaign, the highly lethal disease remains a threat due to its potential use in bioterrorism. Similar poxviruses that may be transmitted to humans from animals are also a concern. There is thus an interest in the development of antiviral drugs against this class of virus. While the viral genome replication machinery is an obvious target, its structure is not well understood.

Dr. Wim Burmeister, Dr. Frederic Iseni, and Dr. Nicolas Tarbouriech have long been working on the DNA replication machinery of the vaccinia virus. In collaboration with Dr. Guy Schoehn, we investigated the structure of the helicase-primase D5, an essential viral protein in the replication machine of the vaccinia virus. Using the single particle reconstruction technique, we studied the D5 helicase domain expressed by Dr. Stephanie Hutin.

The D5 protein consists of four domains. It has an N-terminal archaeoeukaryotic primase domain, followed by a cysteine cluster region and a D5N domain associated with D5-type helicases, and a superfamily 3 helicase domain at the C terminus. Earlier studies of D5 has indicated that it has a six-fold symmetry[63]. To simplify the protein production, different deletion constructs that could be produced in E. coli was created (Figure 26). A construct with residues 323-785 was found to show ATPase activity similar to the full-length D5 protein expressed in insect cells. This construct also forms a hexamer and was used for electron microscopy studies.
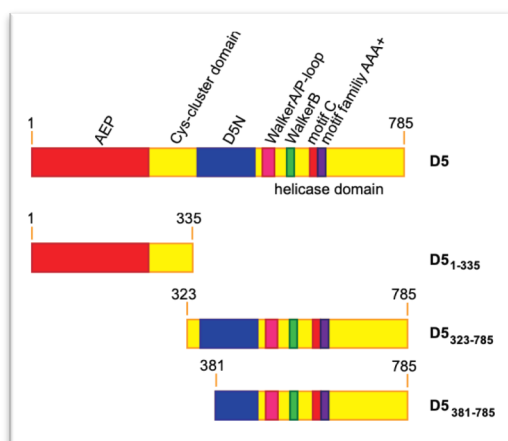
Figure 26. Domain organization of D5 and different constructs produced by Dr. Stephanie Hutin. The full-length protein is 95 kDa. The primase domain lies on the N-terminal. The superfamily 3 helicase domain on the C-terminal contains a motif characteristic of the AAA+ ATPase family. Construct D5$_{1-335}$, which lacks the ATPase motif, did not show any ATPase activity, as expected. Construct D5$_{381-785}$ lacks the oligomerization domain found in residues 323 to 380 and did not form a hexamer, which seems to be necessary for ATPase activity. The construct D5$_{323-785}$, which forms a hexamer and shows ATPase activity, was used in electron microscopy studies.

Figure 27 shows the 2-dim class averages from TEM images of the D5$_{323-785}$ negatively stained with 2% sodium silicotungstate. A 3-dim reconstruction confirms the hexameric structure. The model shows that the six protein subunits form a ring with tight interactions on one side. On the other side, the subunits are not connected, leaving a large opening along the six-fold axis.
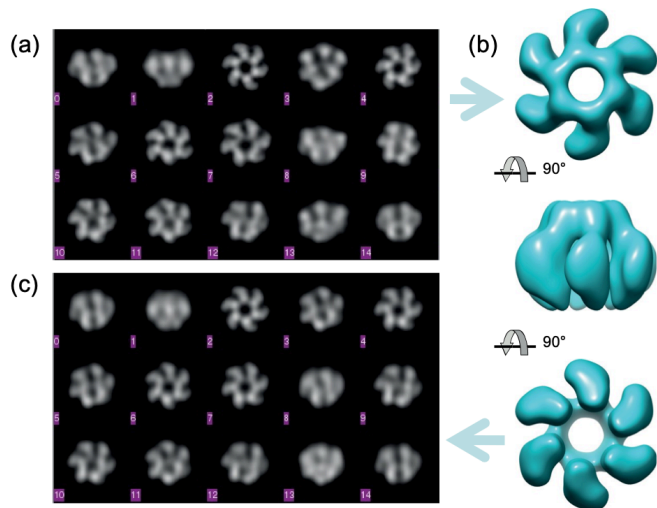
Figure 27. Single particle analysis of negatively stained D5$_{323-735}$. (a) Reference-free 2-dim class averages of D5$_{323-735}$ particles stained with 2% sodium silicotungstate. (b) Top, side, and bottom views of the 3-dim model from the reconstruction after refinement. The contour level is set to correspond to the expected volume of the hexamer. (c) Reprojections of the 3-dim model in b that best match the 2-dim classes in a.

Cryo-electron microscopy was performed to try to get a higher-resolution structure of the particle. The D5$_{323-785}$ was plunged frozen with a vitrobot. Class averages from 2-dim classification of the cryo-TEM images show details of the protein in the 'top' view looking down the (pseudo-)six-fold axis and reveal various conformations of the protein (Figure 28). No consistent 3-dim models could be obtained from the data as the negatively stained model did not have enough resolution to assign side views to the different conformations. Efforts to stabilize the protein in one conformation with various nucleotides was not successful. We also tried to use different glow discharge conditions, different support films, different additives such as amino acids and different ions, different blotting conditions, etc. to change the orientation of the particles in the ice but with no success.
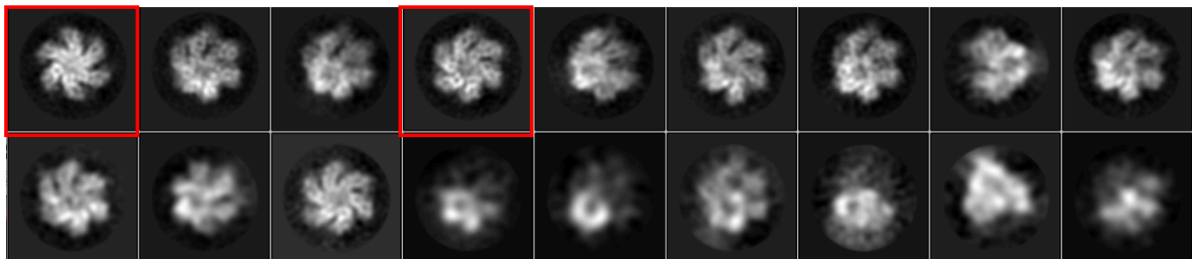
Figure 28. Two-dimensional class averages of cryo-electron microscopy images of D5$_{323-735}$ particles. Top views of different conformations of the proteins can be resolved (e.g. red boxes). No consistent 3-dim reconstruction could be obtained from the data set because of the lack of side views.

Dr. Hutin also expressed the full length D5 protein. Two-dimensional classes from negatively stained data are shown in Figure 29. The primase domain can be located on the side of the ring with tighter interaction. Nevertheless, the domain seems highly flexible and no further analysis could be achieved. The protein expressed in insect cells seemed to exhibit a higher degree of stability but nonetheless not enough for a consistent 3-dim classification.

Further effort to achieve a more homogeneous protein sample will be necessary to gain higher-resolution structural information with TEM for the D5 protein.
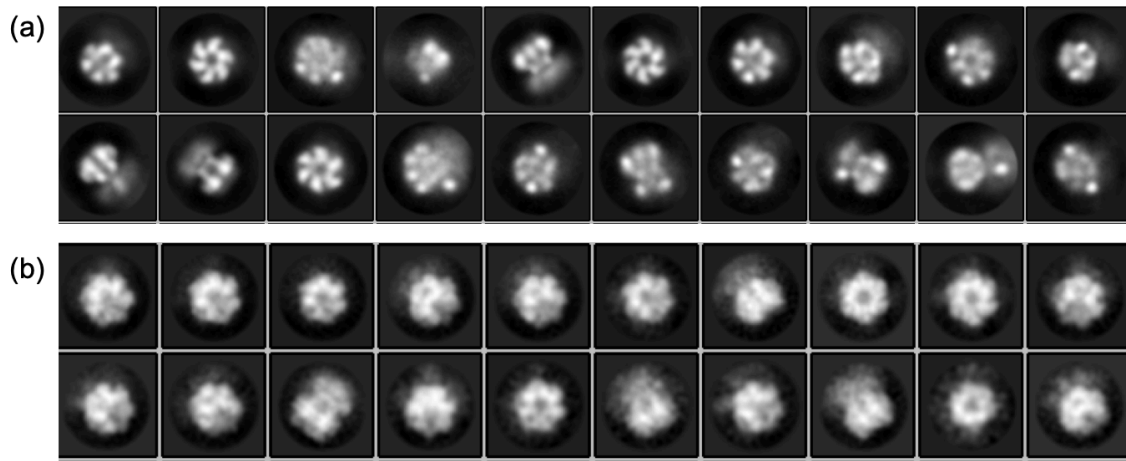
Figure 29. *Two-dimensional class averages of the full-length D5 protein produced in E. Coli BL21 Star (DE3) (a) and in SF21 insect cells (b). ADP and Mg^{2+} ions have been added to both samples. The primase domain appears as diffuse density localized mainly on one side of the particle.*

Publication:

--- Hutin, S., Ling, W.L., Round, A., Effantin, G., Reich, S., Iseni, F., Tarbouriech, N., Schoehn, G., Burmeister, W.
"*Domain organization of vaccinia virus helicase-primase D5*"
Journal of Virology 90, 4604-13 (2016)

Section II. Projects
Chapter 1. Cryo-electron diffraction of 3-dim crystals

While X-ray macromolecular crystallography has been a popular technique in structural biology and therapeutic drug search, obtaining crystals of a sufficient size (over a few microns) remains a major bottleneck. Membrane proteins, in particular, often yield only small crystals. Recent developments in cryo-electron crystallography open up a unique opportunity to study nano-sized (few hundred nanometers) crystals and may be a promising technique for structural studies of membrane proteins.

Electron diffraction studies by TEM are limited to nanocrystals and the reduced signal compared to microcrystals is compensated by the strong scattering of electrons. Considering the mean free path of 300 keV electrons in organic materials, crystal thickness is limited to ~300 nm for electron diffraction studies. Typical crystals for X-ray crystallography have size $\sim (30 \ \mu m)^3$ and thus 10^6 times more unit cells. The atomic form factor for electron scattering, $f_{el}(\Delta \mathbf{k})$ is related to that for X-ray scattering $f_x(\Delta \mathbf{k})$ by:

$$f_{el}(\Delta \mathbf{k}) = \frac{2me^2}{\hbar^2 \Delta k^2} \left[Z - \frac{mc^2}{e^2} f_x(\Delta \mathbf{k}) \right],$$

or,

$$f_{el}(\Delta \mathbf{k}) = \frac{3.779}{\Delta k^2} [Z - 3.54 \ \times \ 10^4 f_x(\Delta \mathbf{k})],$$

where m is the mass of the electron, e the charge of the electron, c the speed of light, $\hbar$ the Planck's constant divided by 2π, and Z the atomic number; the units for Δk is in Å^{-1}.[64]

The orders of magnitude stronger $f_{el}(\Delta \mathbf{k})$ compensates for the reduced number of unit cells available in the nanocrystals. Nonetheless, the reflections are very weak, especially at very high resolution (beyond 2 Å). Recent development of the new hybrid pixel detectors, which have superior dynamic range, signal-to-noise ratio, and quantum efficiency, has made macromolecular electron crystallography possible.

Due to the mosaicity common in protein crystals, only partial intensities of the reflections are obtained in still diffraction. Integrated intensities of inorganic samples have been obtained by precession of the electron beam about the optical axis.[65] *Ab initio* structure solution has been obtained from electron diffraction by combining tomography and electron precession.[66] Diffraction patterns were taken at regular interval on the same crystal rotated along a tilt axis while at each tilt angle, the electron beam is precessed around the optical axis to obtain the integrated intensities of the reflections. Importantly for inorganic materials with heavy elements, precession significantly reduces the dynamic effects that complicate data interpretation.[67] Alternative to precession, beam tilt can also be combined with sample stage rotation to integrate the full intensity of the reflections.[68] This technique has allowed the structure of calcined zeolite sample with 72 unique atoms to be solved with direct methods.[69]

With computer-controlled sample stage (compustage) that allows precision sample motion and CMOS detectors with fast readout and sensitivity for low electron dose, a series of diffraction patterns can now be collected from individual crystal on continuous rotation of the crystal. Such data collection mode allows intensities to be integrated spatially during rotation without precession or beam tilt.[70] By collecting data at cryogenic temperature, the technique was used to solve the structure of the model protein lysozyme and was named MicroED by the Gonen group.[71] Data collected with continuous rotation can be processed with standard X-ray crystallography software supported by the CCP4 program suite, which has a large user support community [72 73 74].

Cryo-electron crystallography has since been used to determine a number of protein structures with nanocrystals.[75] Besides lysozyme, other proteins with known structures, including and Ca^{2+}-ATPase, catalase, proteinase K, xylanase, thaumatin, trypsin, and thermolysin, have also been solved by cryo-electron diffraction with continuous rotation.[75–77] Even though these structures have been solved

previously by X-ray models, structures from electron diffraction yield extra information not available from X-ray structures. Since electrons interact with atoms through the Coulomb potential, electron diffraction structures can probe the charged states of amino acids and bound metal ions. For instance, the charged state of the iron ion in the heme group in catalase has been inferred from the Coulomb potential map.[76] This information, nonetheless, has to be carefully considered because the metal ion valence state are sometimes sensitive to radiation damage, as has been evident in X-ray studies.[78] On the other hand, the Coulomb potential map has confirmed the theoretical prediction that the Glu-908 side chain around the Ca^{2+} binding site is protonated in Ca^{2+}-ATPase. Electron diffraction, therefore, is a complementary technique to X-ray diffraction.

Besides proteins of known structures, the technique has also successfully solved unknown structures of small peptides [79,80]. The first unknown structure solved by "MicroED" was from 'invisible' crystals formed by a 11-residue segment (NACore) of α-synuclein, the main component of the aggregates observed in Parkinson and other neurodegenerative pathologies.[79] These crystals are needle shaped with diameter of 50-300 nm and length over 1 μm. They are so small that they are invisible to optical microscopes and were taken as amorphous aggregates. These crystals have a favorable geometry for the "MicroED" technique. Their cross-section is just below the mean-free path of the electrons at the imaging voltage, thus allow maximal number of unit cells to contribute to the diffraction. The long length permits diffraction patterns to be collected from unexposed parts along the same crystals as tilting proceeds. The structure of these 'invisible' crystals was determined by molecular replacement using a search model derived from the X-ray crystallography model of a nine-residue subsegment (SubNACore) of the NACore, which forms much larger crystals. Despite the fact that the SubNACore and NACore differ by only 2 residues, their level of toxicity differs noticeably. The structure of NACore has therefore been very useful in understanding the toxicity of α-synuclein, demonstrating the power and value of the technique.

All these encouraging results show that cryo-electron diffraction is a very promising technique for solving protein structures with submicron-sized crystals. The same sample preparation technique for cryo-electron microscopy is employed to prepare nanocrystals for cryo-electron diffraction studies. Nano-sized protein crystals are applied to Quantifoil or lacey carbon grids and plunge frozen into liquid ethane. Protein molecules are thus preserved in their hydrated state. Electron diffraction of 3-dim crystals collects data in the diffraction mode as opposed to image-based cryo-EM techniques, such as single particle analysis or real-space tomography, which collects data in the imaging mode. Imaging weak phase objects like native hydrated protein samples requires a contrasting mechanism. A defocus is usually applied to create phase contrast, which is the main contribution to the contrast transfer function that modifies the signal of the imaged object. Besides the extra steps required to correct for the modification from the contrast transfer function, it significantly limits the ultimate resolution that imaging techniques can achieve. The use of phase plate avoids the introduction of defocus. Nevertheless, resolution of the final 3-dim structure suffers from even slight deviation from the true focus, as for inaccurate determination of the defocus value in CTF correction.[81]

Besides avoiding the CTF, electron crystallography has other advantages over other 3-dim TEM reconstruction techniques. As a corollary of the Radon transform, 3-dim structure can be reconstructed from a set of 2-dim projections (e.g. images from transmission electron microscopes) as the projections yield sections in the 3-dim Fourier space. In tomography, projections of the sample are collected at defined tilt angles of the sample stage (Section I, Chapter 2). The relative orientations of the projections are thus known but translational alignment is still required because of the unavoidable imperfections of the sample stage. Due to large radiation dose at high magnification and the limited precision of the sample stage, only relatively large objects can be studied by tomography, though sub-tomogram averaging can yield higher-resolution information of smaller components that appear in multiple copies. Single particle analysis, on the other hand, collects 2-dim projections of protein samples relying on random orientations of a large number of identical protein molecules (Section I, Chapter 4). At least tens of thousands of images of the molecules are collected in hundreds of micrographs. These images are then classified and images in the same class are averaged. The orientations of the class averages are determined for 3-dim reconstruction. Reliable alignment limits the size of the molecules that can be analyzed to ~100 kDa. A meaningful reconstruction relies critically on the homogeneity of the

sample. Advanced data analysis can separate a mixed sample with a few homogeneous subsets to yield structures of different configurations of a molecule or of various subcomponents of a complex but such procedure, though powerful, requires proportionally more images to be collected and does not always yield positive results. Importantly, sample homogeneity cannot be ascertained until a high-resolution reconstruction is obtained after data collection and analysis, which takes weeks to months.

Electron diffraction with continuous sample rotation can be advantageous over tomography or single particle analysis for small proteins in various aspects. As in tomography, data is collected at known consecutive angles. However, since data is collected in the Fourier space, which is insensitive to translation, i.e., vibration or mechanical instability, no translational alignment is necessary. Nanocrystals of dimensions of ~100 nm typically contains ~10,000 protein molecules. Diffraction data set collected on any such nanocrystal are thus averaged over 10,000 structurally identical molecules in already the same orientation. No 2-dim classifications or angular assignments are necessary as in single particle analysis. Moreover, data analysis using advanced X-ray crystallography programs can yield a 3-dim structure within hours in favorable cases. Nevertheless, solving structure of unknown protein of reasonable size (>10 kDa) with electron crystallography is still a challenge. My main project will be to work on some of the issues in applying electron diffraction to solve protein structures.

One particular concern for electron diffraction has been the dynamical effect coming from the strong interaction of electrons with atoms. The dynamical effect arises when electrons encounter multiple scattering and is a concern especially for heavy elements. Precession electron microscopy has been a powerful tool to minimize the dynamical effect and allow unknown structures to be solved by direct methods with electron diffraction.[82] Biological materials are mostly made up of light elements and the dynamical effect is less pronounced. Dynamical scattering is also reduced by avoiding data collection exclusively at zone axes. Indeed, structures of the amyloid core of the prion have been solved by direct methods without precession, showing that the dynamical effect does not prevent *ab initio* phasing by electron diffraction.[80] Nevertheless, qualities of electron diffraction maps are poor compared to X-ray crystallography maps and dynamical scattering definitely plays a role. In collaboration with Prof. Jan Pieter Abrahams, whose group is developing advanced algorithm to reduce the effects of dynamical scattering in electron diffraction, we will improve our data processing by considering the effects of dynamical scattering.

Recovering the phases of the reflections is a major challenge in structural resolution in crystallography. Molecular replacement has been used to calculate initial phases in protein electron diffraction structures. Only peptide data that have reached very high resolution (around 1 angstrom) have been successfully treated with direct methods.[80] Unlike in X-ray, no technique has been established for experimental phasing in electron microscopy. Anomalous scattering in electron diffraction is much weaker than in X-ray. Besides, electron microscopes operate at fix voltages, which cannot be freely adjusted. In the context of the project 'Electron diffraction of sensitive materials' led by Dr. Jean-Luc Rouviere supported by the CEA and in collaboration with Dr. Julio Cesar da Silva at the ESRF, ptychography will be explored to recover phase information. This method will also be developed within an ANR project submitted by Dr. Dominique Housset in collaboration with Prof. Jan Pieter Abrahams at Basel University, and Dr. Eric van Genderen at PSI. The ANR project will also involve retrieving phases by taking advantage of the strong interaction of electrons with charged atoms in crystallophore developed by Dr. Eric Girard's group at the IBS.[83] In addition, we will try to exploit site specific radiation damage[84] and real space electron micrographs to retrieve phase information.[85]

Another major obstacle for employing electron diffraction in protein crystallography is the size of the protein crystals. While only nano-sized crystals are required, it is not trivial to control the crystal size. As described in one of the early articles, electron diffraction was used to solve 'invisible' crystals beyond the resolution of optical microscopes. Growth of crystals to be used in electron diffraction thus cannot be easily monitored. In collaboration with Dr. Alexander Van Driessche at UGA/OSUG, we study the nucleation mechanisms for protein crystals.[86] Glucose isomerase is used as a model and different conditions are found to nucleate crystals of different forms (Figure 30). We are also working with Prof. Catherine Venien-Bryan at Sorbonne University to try to optimize the growth of thin stacks of membrane protein crystals for 3-dim electron diffraction studies.[87] Dr. Jean-Luc Pellequer's group

at the IBS is studying the dimensions of the crystals produced with atomic force microscopy to probe the crystal thickness, which cannot be easily accessible by TEM.
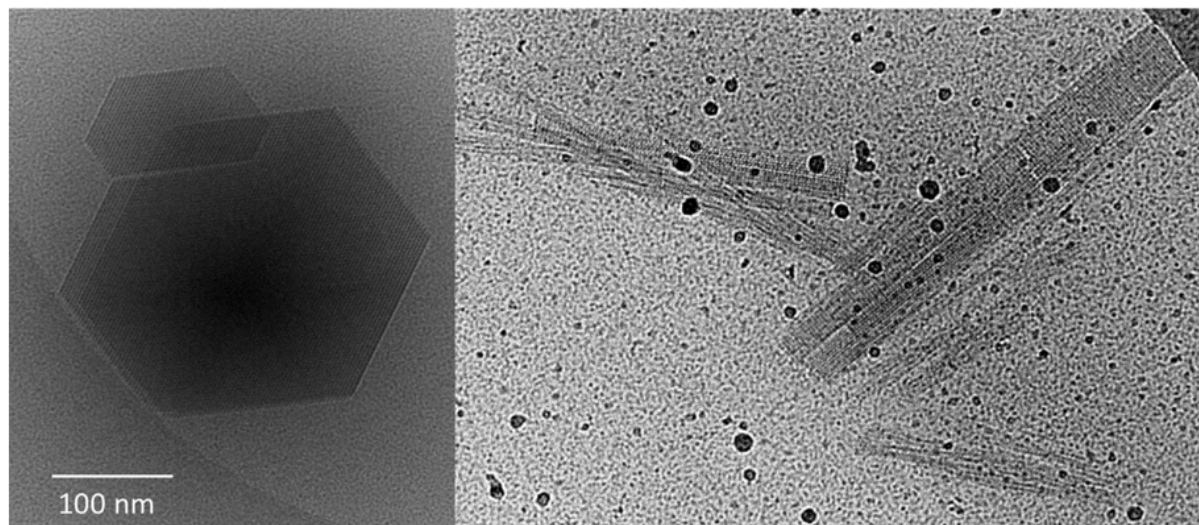
Figure 30. *Different conditions yield different crystal forms of glucose isomerase crystals (samples from Dr. Van Driessche). Compact crystals are formed in one condition (left image). In another crystallization condition (right), monomers first form fibers, which then assemble to form elongated crystals.*

A promising source of crystals for electron diffraction studies are *in vivo* protein crystals. Protein crystallization occurs inside living cells when the cells need to manage a large quantity of protein (e.g. pyrenoid in Chlamydomonas cell shown in the Figure 14 of Section 1, Chapter 2.1). The high protein concentration during recombinant protein expression in cells presents one such circumstance. Indeed, several recombinant proteins with post-translational modifications have been found to crystallize *in vivo* when expressed in the baculovirus insect cell system.[88] This phenomenon represents an exciting opportunity for proteins that fail to crystallize *in vitro*.[89,90] Post-translational modifications are incorporated[91] and membrane proteins will be naturally inserted in lipids. While these crystals may be too small for traditional X-ray diffraction, they are suitable for studies with X-ray free-electron laser as well as electron diffraction, the latter being a much more accessible technique requiring much less material.

Figure 31 shows the *in vivo* crystals found in insect cells overexpressing human connexin 36 (Cx36) from Dr. Valentine Gordeliy's group at the IBS. Connexins (Cx) form intercellular channels (gap junctions) and hemichannels (connexons) that regulate the passage of small molecules and ions between adjoined cells, and between intracellular and extracellular space, respectively.[92–94] They modulate the synchronization of cell activities and also cell proliferation and cell death. Connexins are affected in pathological conditions, such as inflammation and ischemia, and mutations in Cx genes are correlated with a variety of diseases.[95,96]
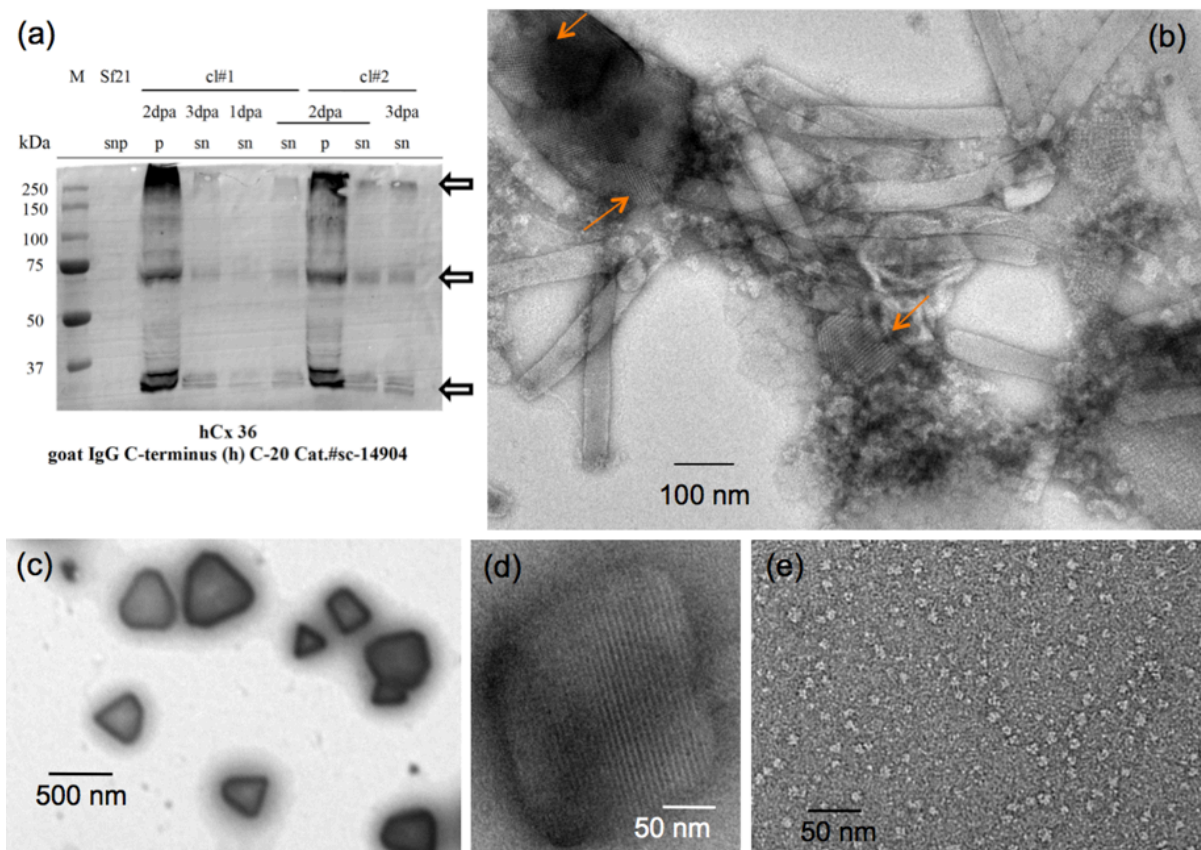
**Figure 31.** *Human connexin 36 (hCx36) expressed as nanocrystals in Sf21 insect cells using baculovirus expression vector. (a) Western-blot analysis with specific anti-Cx36 antibodies confirming the expression of hCx36. (b) Transmission electron micrograph of a membrane fraction before purification stained with 2% sodium silicotungstate showing hCx36 crystals attached to the baculovirus envelope. Examples are pointed out by orange arrows. (c) Purified hCx36 crystals. (d) A magnified view of a nano-crystal showing clear lattice plans that reveal the crystalline order. (e) hCx36 oligomers after prolonged incubation of crystals with harsh detergent. Multiple oligomeric states are present. (Ling et al., unpublished)*

A gap junction channel is formed by two apposed hemichannels, which each consists of six Cx subunits (Figure32). In the human genome, there are twenty-one Cx isoforms with various physiological functions and regulation mechanisms. The 21 isoforms are divided into five groups (α, β, γ, δ, ε) according to their sequence homology. Connexin 36 (36 for estimated mass of 36 kDa), together with Cx31.9 and Cx40.1, belong to the δ family.

Connexin 36 is of particular interest as it is expressed in the central nervous system, as well as in the pancreatic β-cells.[97–99] Gap junctions consisting of Cx36 form electrical synapses between neurons and governs neuroplasticity.[100–102] These synapses are distinct from the more common chemical synapses and determine neuronal synchronization, signal averaging and network oscillations.[103–106] Expression of Cx36 is found to increase during early postnatal development and after neuronal injury, such as stroke (ischemia).[107] Blocking Cx36 is shown to disrupt learning and memory.[108] In the case of ischemic insult, regulation of gap junction channels and hemichannels involving Cx36 significantly affects the propagation of cell damage and death.[109,110] Loss of Cx36 also impairs vision and causes symptoms resembling type 2 diabetes.[111,112] The gating mechanisms of Cx36 are critical for specific modulation of Cx36 conductance underlying its functions in these important areas, including the plasticity of Cx36 electrical synapses that governs our cognition.
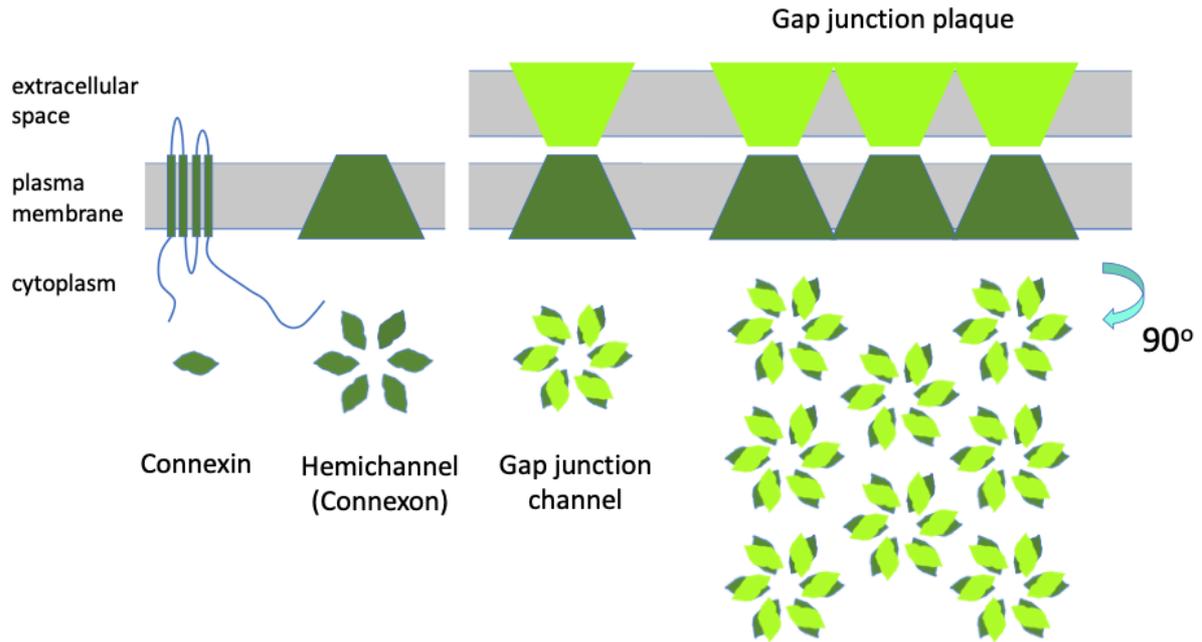
Figure 32. Connexin higher-order structure and organization. Connexins (Cx) have four transmembrane helices with the N- and C-termini in the cytoplasmic side. Six Cx monomers form a connexon or a hemichannel that allows the passage of small ions and molecules between the cytoplasm and the extracellular space. Hemichannels in adjacent cells can dock to form gap junction channels, which organize into gap junction plaques for the modulation of direct communication between the two cells.

Despite its importance, molecular mechanisms behind the regulation of Cx36, as for almost all other members of the Cx family, are very poorly understood. This lack of knowledge goes hand in hand with the lack of high-resolution structural information on Cx. Structural studies of most membrane proteins is demanding but studies of Cx faces particular problems.[113] Connexins are difficult to purify from tissues as they have low expressions and they are often mixed with different isoforms. A recombinant protein expression system is therefore required to obtain pure Cx samples. Besides, as post-translational modifications are key to their slow gating regulations, Cx usually have multiple phosphorylation sites and Cx samples in general have mixed degree of post-translational modifications.[114] Moreover, Cx form different oligomers (from dimers to hexamers) when mixed with detergents. Obtaining a homogeneous Cx sample is thus extremely challenging. Electron diffraction of Cx crystals produced *in vivo* would bypass most of these difficulties.

Another source of *in vivo* protein crystals comes from Dr. Jacque-Philippe Colletier's team at the IBS.[115] Figure 33 shows crystals of an insecticide protein produced *in vivo* in bacteria. Selected area diffraction allows us to obtain a diffraction pattern on individual crystals. Crystals from different combinations of toxins are also produced in bacteria by Dr. Guillaume and Dr. Lopes with Dr. Colletier.[116] Electron diffraction would allow the structural determination of these crystals simultaneously.[117]

While these crystals are too small for conventional X-ray crystallography, some of them are still too thick for the transmission of a 200 keV electron beam. In collaboration with Dr. Christine Moriscot, Benoit Gallet, and Dr. Guy Schoehn, we plan to perform cryo-sectioning on these crystals to obtain sections of crystals thin enough for electron diffraction. The whole bacteria producing these crystals will be high pressure frozen and cryo-sectioned directly (see Section I, Chapter 2.1). Besides cryo-ultramicrotomy, cryo-focused ion beam may also be tried in collaboration with Dr. Pierre-Henri at the CEA.[118]
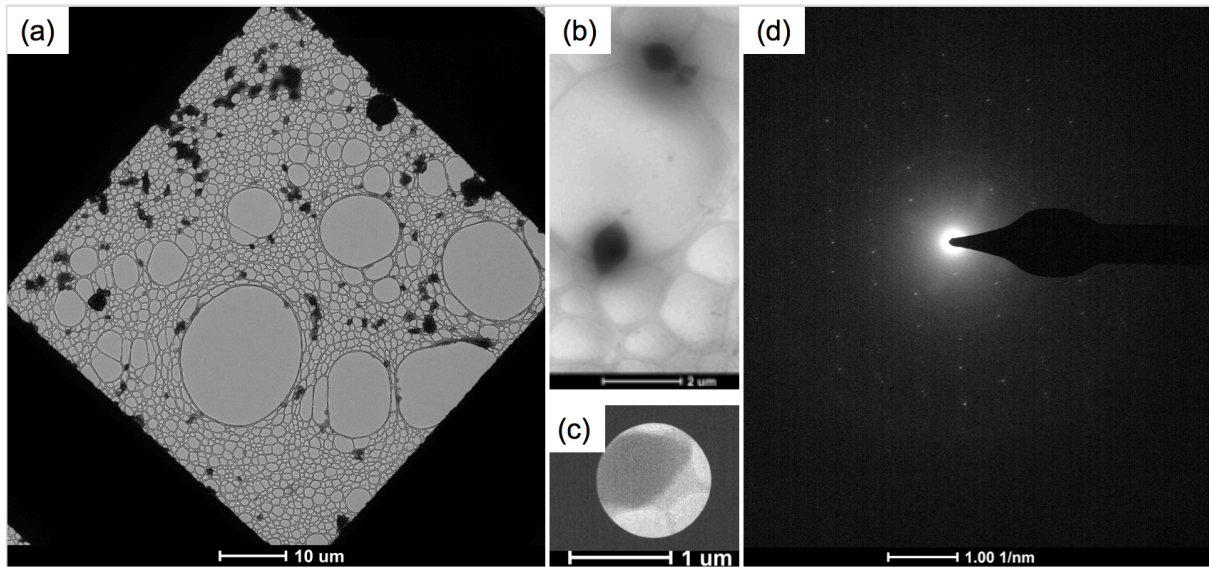
*Figure 33*. *Purified crystals of Cyt1A grown in vivo in bacteria. (a) Large field of view of crystals preserved in their hydrated state on lacey carbon film. (b) Enlarged view of two crystals. (c) The selected area diffraction aperture allows us to obtain diffraction from a single crystal. Alternatively, nanobeam can be used to limit the area contributing to the diffraction pattern. (d) Selected area diffraction of a Cy1A crystal.*

Chapter 2. Electron microscopy and diffraction of engineered nanoparticles

Colloidal nanoparticles have many potential applications in energy, photonics, microelectronics, and medicine. Information on the internal structure (core/shell vs composition gradient), the size and the dispersion of these quantum dots are crucial for optimizing their synthesis to yield optimal quantum fluorescence and functionalization for their various applications. X-ray techniques have been used commonly to study these nanoparticles. Nevertheless, these techniques are global techniques, which give information on the average of the sample and cannot access information of individual particles. Transmission electron microscopy is complementary to X-ray diffraction.

Because of their small size (~1-5 nm), carbon support films contribute significantly to the background noise when imaging these nanoparticles. In collaboration with Dr. Peter Reiss at the CEA, I will develop techniques to image these novel nanoparticles. Dr. Reiss specializes in quantum dots without toxic heavy metals such as Cd. These low toxicity quantum dots are based on InP and CuInS2.[119,120] Figure 34a shows a graphene oxide film deposited on a Quantifoil grid. The crystalline lattice can be resolved in quantum dots deposited on the graphene oxide layer (Figure 34b).
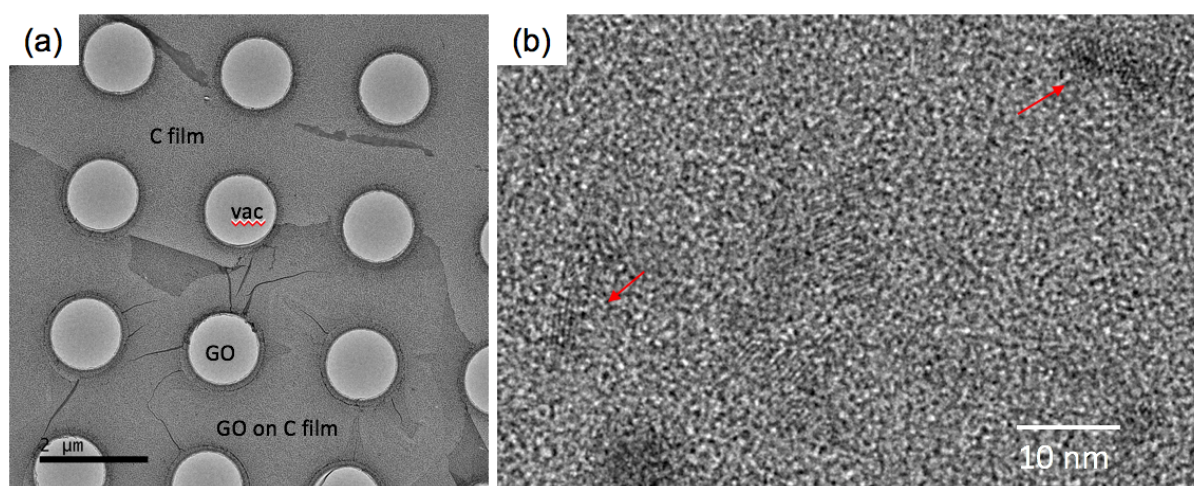
***Figure 34.** Imaging colloidal quantum dots. (a) A graphene oxide (GO) film deposited on a R1.2/1.3 Quantifoil can be seen on the bottom half of the image. The Quantifoil consists of a carbon (C) film with regular holes (vac for vacuum) of diameter 1.2 μm separated by 1.3 μm. (b) Quantum dots found in GO region. As GO is much more transparent to the electron beam than C, background noise is significantly reduced for quantum dots deposited on GO films suspended in the holes. Red arrows point to some quantum dots in which the crystalline lattice has be resolved.*

Besides noise from the support film, beam-induced motion of the particles is also an important factor that limits the resolution of the particles. Even though counting electron detectors allow very rapid recording of movies, for which movie frames can be realigned to correct drift, only collective drift (drift of sample holder or grid) can be easily corrected. Direction and magnitude of beam-induced particle motion depends on the particle size, its adhesion to the support film, and its immediate environment. Such local motion is not taken into consideration in conventional drift correction. In the future, different imaging conditions will be applied to try to reduce the particle movement. Data analysis technique may also be developed to deal with individual particle motion.

Electron diffraction on these nanoparticles will also be developed. Electron powder diffraction patterns can be compared to the X-ray powder diffraction patterns. Importantly, electron diffraction will allow us to focus on smaller sample area and detect coexisting structures, which often happen during synthesis of nanoparticles. Existing X-ray powder diffraction programs will be adapted to analyze electron powder diffraction patterns.

Publication:

-- Wegner, K.D., Pouget, S., <u>Ling, W.L.,</u> Carrière, M., and Reiss, P.
"Gallium -- a versatile element for tuning the photoluminescence properties of InP quantum dots."
Chemical Communications (2019) DOI: 10.1039/c8cc09740b

Chapter 3. Structural studies of C1q

Continuing the collaboration with IRPAS group at the IBS, we will study the C1/IgM complex as an effort to solve the structure of C1. As discussed in Section 1, Chapter 3, C1q is the recognition unit of the C1 complex, the first complement protein that activates complement through the classical pathway. The C1 complex comprises C1q and a tetrameric proenzyme C1r$_2$s$_2$. When C1q binds to an activator, mechanical changes cause the self-activation of C1r, which then activates C1s. Nonetheless, the structure of C1 and the mechanism of C1 activation is still not resolved due to the flexibility of the components.

In acquired immunity, the complement is activated when C1q recognizes bound antibodies. Various recombinant IgMs will be produced in IRPAS to bind C1 in an effort to rigidify the flexible molecule. For instance, Figure 35 shows an image of recombinant IgM617 preserved in its native hydrated state. Single particle analysis will be employed to solve the structure of the IgM-C1 complex when a stable complex is obtained. Cryo-electron tomography may also be performed to get a lower resolution model.
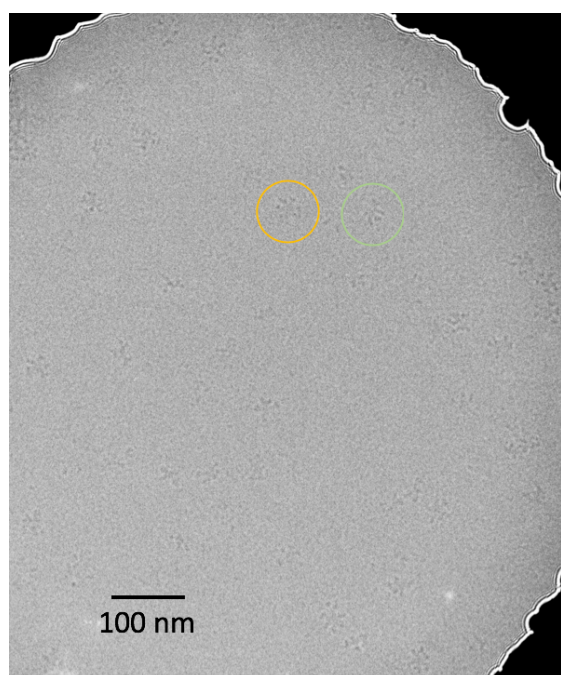
Figure 35. Cryo-electron micrograph of IgM 617. Sample has been applied to a Au Ultrafoil grid and vitrified with the vitrobot. The IgM molecules are well separated and different views of the molecules can be found. For example, the orange circle and the green circle highlight two different views of the molecules.

Publications:
-- Arlaud, G.J., Gaboriaud, C., Ling, W.L., Thielens, N.
"Structure of the C1 complex of complement"
Proceedings of the National Academy of Sciences 114, E5766-5767 (2017)
-- Gaboriaud, C., Ling, W.L., Thielens, N., Bally, I., Rossi, V.
"Deciphering the fine details of C1 assembly and activaton mechanisms: "mission impossible"?"
Frontiers in immunology 5, 565-569 (2014)

Bibliography

(1)   Carter, C.; Hwang, R. Dislocations and the Reconstruction of (111)Fcc Metal-Surfaces. *Phys. Rev. B* **1995**, *51* (7), 4730–4733. https://doi.org/10.1103/PhysRevB.51.4730.

(2)   Alerhand, O.; Vanderbilt, D.; Meade, R.; Joannopoulos, J. Spontaneous Formation of Stress Domains on Crystal-Surfaces. *Phys. Rev. Lett.* **1988**, *61* (17), 1973–1976. https://doi.org/10.1103/PhysRevLett.61.1973.

(3)   Thayer, G. E.; Bartelt, N. C.; Ozolins, V.; Schmid, A. K.; Chiang, S.; Hwang, R. Q. Linking Surface Stress to Surface Structure: Measurement of Atomic Strain in a Surface Alloy Using Scanning Tunneling Microscopy. *Phys. Rev. Lett.* **2002**, *89* (3), 036101. https://doi.org/10.1103/PhysRevLett.89.036101.

(4)   Stevens, J.; Hwang, R. Strain Stabilized Alloying of Immiscible Metals in Thin-Films. *Phys. Rev. Lett.* **1995**, *74* (11), 2078–2081. https://doi.org/10.1103/PhysRevLett.74.2078.

(5)   Gong, J. Structure and Surface Chemistry of Gold-Based Model Catalysts. *Chem. Rev.* **2012**, *112* (5), 2987–3054. https://doi.org/10.1021/cr200041p.

(6)   Venables, J. A. *Introduction to Surface and Thin Film Processes*, 1st ed.; Cambridge University Press, 2000.

(7)   Herring, C. in: Gomer, R., Smith, C. S. (Eds), *Structure and Properties of Solid Surfaces*, University of Chicago Press, Chicago, **1952**.

(8)   Rohrer, G. S.; Rohrer, C. L.; Mullins, W. W. Coarsening of Faceted Crystals. *J. Am. Ceram. Soc.* **2002**, *85* (3), 675–682.

(9)   Bauer, E. Low-Energy-Electron Microscopy. *Rep. Prog. Phys.* **1994**, *57* (9), 895–938. https://doi.org/10.1088/0034-4885/57/9/002.

(10)   Chung, W. F.; Feng, Y. J.; Poon, H. C.; Chan, C. T.; Tong, S. Y.; Altman, M. S. Layer Spacings in Coherently Strained Epitaxial Metal Films. *Phys. Rev. Lett.* **2003**, *90* (21), 216105. https://doi.org/10.1103/PhysRevLett.90.216105.

(11)   Jonker, B. T.; Bartelt, N. C.; Park, R. L. Quantum Size Effect in Electron Transmission through Cu and Ag Films on W(110). *Surf. Sci.* **1983**, *127* (2), 183–199. https://doi.org/10.1016/0039-6028(83)90413-2.

(12)   Feibelman, P. J. Formation and Diffusion of S-Decorated Cu Clusters Onc Cu(111). *Phys. Rev. Lett.* **2000**, *85* (3), 606–609. https://doi.org/10.1103/PhysRevLett.85.606.

(13)   Heegemann, W.; Meister, K.; Bechtold, E.; Hayek, K. Adsorption of Sulfur on (100) and (111) Faces of Platinum - Leed and Aes Study. *Surf. Sci.* **1975**, *49* (1), 161–180. https://doi.org/10.1016/0039-6028(75)90334-9.

(14)   Foss, M.; Feidenhansl, R.; Nielsen, M.; Findeisen, E.; Buslaps, T.; Johnson, R. L. Sulfur Induced Cu-4 Tetramers on Cu(111). *Surf. Sci.* **1997**, *388* (1–3), 5–14. https://doi.org/10.1016/S0039-6028(97)00071-X.

(15)   McLean, J. G.; Krishnamachari, B.; Peale, D. R.; Chason, E.; Sethna, J. P.; Cooper, B. H. Decay of Isolated Surface Features Driven by the Gibbs-Thomson Effect in an Analytic Model and a Simulation. *Phys. Rev. B* **1997**, *55* (3), 1811–1823. https://doi.org/10.1103/PhysRevB.55.1811.

(16)   Wahlstrom, E.; Ekvall, I.; Olin, H.; Lindgren, S. A.; Wallden, L. Observation of Ordered Structures for S/Cu(111) at Low Temperature and Coverage. *Phys. Rev. B* **1999**, *60* (15), 10699–10702. https://doi.org/10.1103/PhysRevB.60.10699.

(17)   Icking-Konert, G. S.; Giesen, M.; Ibach, H. Decay of Cu Adatom Islands on Cu(111). *Surf. Sci.* **1998**, *398* (1–2), 37–48. https://doi.org/10.1016/S0039-6028(97)00755-3.

(18)   Hannon, J. B.; Klunker, C.; Giesen, M.; Ibach, H.; Bartelt, N. C.; Hamilton, J. C. Surface Self-Diffusion by Vacancy Motion: Island Ripening on Cu(001). *Phys. Rev. Lett.* **1997**, *79* (13), 2506–2509. https://doi.org/10.1103/PhysRevLett.79.2506.

(19)   Dubochet, J.; Adrian, M.; Chang, J.; Homo, J.; Lepault, J.; Mcdowall, A.; Schultz, P. Cryo-Electron Microscopy of Vitrified Specimens. *Q. Rev. Biophys.* **1988**, *21* (2), 129–228. https://doi.org/10.1017/S0033583500004297.

(20)   Frank, J. *Three-Dimensional Electron Microscopy of Macromolecular Assemblies: Visualization of Biological Molecules in Their Native State*, 2nd ed.; Oxford University Press: New York, 2006.

(21)   Glauert, A. M. and Lewis, P. R. *Biological Specimen Preparation for Transmission Electron Microscopy*; Princeton University Press: Princeton, 1998. https://press.princeton.edu/titles/6666.html.

(22)   Vanhecke, D.; Graber, W.; Studer, D. Chapter 9 Close-to-Native Ultrastructural Preservation by High Pressure Freezing. In *Methods in Cell Biology*; Introduction to Electron Microscopy for Biologists; Academic Press, 2008; Vol. 88, pp 151–164. https://doi.org/10.1016/S0091-679X(08)00409-3.

(23)   Murray, S. Chapter 1 High Pressure Freezing and Freeze Substitution of Schizosaccharomyces Pombe and Saccharomyces Cerevisiae for TEM. In *Methods in Cell Biology*; Introduction to Electron Microscopy for Biologists; Academic Press, 2008; Vol. 88, pp 3–17. https://doi.org/10.1016/S0091-679X(08)00401-9.

(24)   Al-Amoudi, A.; Chang, J.-J.; Leforestier, A.; McDowall, A.; Salamin, L. M.; Norlen, L. P.; Richter, K.; Blanc, N. S.; Studer, D.; Dubochet, J. Cryo-Electron Microscopy of Vitreous Sections. *EMBO J* **2004**, *23* (18), 3583–3588. https://doi.org/10.1038/sj.emboj.7600366.

(25)   Midgley, P. A.; Ward, E. P. W.; Hungría, A. B.; Thomas, J. M. Nanotomography in the Chemical, Biological and Materials Sciences. *Chem. Soc. Rev.* **2007**, *36* (9), 1477–1494. https://doi.org/10.1039/B701569K.

(26)   Kishore, U.; Reid, K. B. M. C1q: Structure, Function, and Receptors. *Immunopharmacology* **2000**, *49* (1–2), 159–170. https://doi.org/10.1016/S0162-3109(00)80301-X.

(27)   Kouser, L.; Madhukaran, S. P.; Shastri, A.; Saraon, A.; Ferluga, J.; Al-Mozaini, M.; Kishore, U. Emerging and Novel Functions of Complement Protein C1q. *Front. Immunol.* **2015**, *6*. https://doi.org/10.3389/fimmu.2015.00317.

(28)   Gaboriaud, C.; Juanhuix, J.; Gruez, A.; Lacroix, M.; Darnault, C.; Pignol, D.; Verger, D.; Fontecilla-Camps, J. C.; Arlaud, G. J. The Crystal Structure of the Globular Head of Complement Protein C1q Provides a Basis for Its Versatile Recognition Properties. *J. Biol. Chem.* **2003**, *278* (47), 46974–46982. https://doi.org/10.1074/jbc.M307764200.

(29)   Ross, R. Mechanisms of Disease - Atherosclerosis - An Inflammatory Disease. *N. Engl. J. Med.* **1999**, *340* (2), 115–126. https://doi.org/10.1056/NEJM199901143400207.

(30)   Lusis, A. J. Atherosclerosis. *Nature* **2000**, *407* (6801), 233–241. https://doi.org/10.1038/35025203.

(31)   Torzewski, M.; Lackner, K. J. Initiation and Progression of Atherosclerosis - Enzymatic or Oxidative Modification of Low-Density Lipoprotein? *Clin. Chem. Lab. Med.* **2006**, *44* (12), 1389–1394. https://doi.org/10.1515/CCLM.2006.259.

(32)   Biro, A.; Thielens, N. M.; Cervenak, L.; Prohaszka, Z.; Fust, G.; Arlaud, G. J. Modified Low Density Lipoproteins Differentially Bind and Activate The. *Mol. Immunol.* **2007**, *44* (6), 1169–1177. https://doi.org/10.1016/j.molimm.2006.06.013.

(33)   Dersch, K.; Ichijo, H.; Bhakdi, S.; Husmann, M. Fatty Acids Liberated from Low-Density Lipoprotein Trigger Endothelial Apoptosis via Mitogen-Activated Protein Kinases. *Cell Death Differ.* **2005**, *12* (8), 1107–1114. https://doi.org/10.1038/sj.cdd.4401633.

(34)   Prusiner, S. Novel Proteinaceous Infectious Particles Cause Scrapie. *Science* **1982**, *216* (4542), 136–144. https://doi.org/10.1126/science.6801762.

(35)   Silveira, J. R.; Raymond, G. J.; Hughson, A. G.; Race, R. E.; Sim, V. L.; Hayes, S. F.; Caughey, B. The Most Infectious Prion Protein Particles. *Nature* **2005**, *437* (7056), 257–261. https://doi.org/10.1038/nature03989.

(36)   Valazquez, P.; Cribbs, D. H.; Poulos, T. L.; Tenner, A. J. Aspartate Residue 7 in Amyloid Beta-Protein Is Critical for Classical Complement Pathway Activation: Implications for Alzheimer's Disease Pathogenesis. *Nat. Med.* **1997**, *3* (1), 77–79. https://doi.org/10.1038/nm0197-77.

(37)   Mabbott, N. A.; Bruce, M. E.; Botto, M.; Walport, M. J.; Pepys, M. B. Temporary Depletion of Complement Component C3 or Genetic Deficiency of C1q Significantly Delays Onset of Scrapie. *Nat. Med.* **2001**, *7* (4), 485–487. https://doi.org/10.1038/86562.

(38)   Gehlenborg, N.; Hwang, D.; Lee, I. Y.; Yoo, H.; Baxter, D.; Petritis, B.; Pitstick, R.; Marzolf, B.; DeArmond, S. J.; Carlson, G. A.; et al. The Prion Disease Database: A Comprehensive Transcriptome Resource for Systems Biology Research in Prion Diseases. *Database- J. Biol. Databases Curation* **2009**, bap011. https://doi.org/10.1093/database/bap011.

(39)   Tran, P. A.; Zhang, L.; Webster, T. J. Carbon Nanofibers and Carbon Nanotubes in Regenerative Medicine. *Adv. Drug Deliv. Rev.* **2009**, *61* (12), 1097–1114. https://doi.org/10.1016/j.addr.2009.07.010.

(40)   Sirivisoot, S.; Yao, C.; Xiao, X.; Sheldon, B. W.; Webster, T. J. Greater Osteoblast Functions on Multiwalled Carbon Nanotubes Grown from Anodized Nanotubular Titanium for Orthopedic Applications. *Nanotechnology* **2007**, *18* (36), 365102. https://doi.org/10.1088/0957-4484/18/36/365102.

(41)   Chen, R. J.; Bangsaruntip, S.; Drouvalakis, K. A.; Wong Shi Kam, N.; Shim, M.; Li, Y.; Kim, W.; Utz, P. J.; Dai, H. Noncovalent Functionalization of Carbon Nanotubes for Highly Specific Electronic Biosensors. *Proc. Natl. Acad. Sci. U. S. A.* **2003**, *100* (9), 4984–4989. https://doi.org/10.1073/pnas.0837064100.

(42)   Schrand, A. M.; Hens, S. A. C.; Shenderova, O. A. Nanodiamond Particles: Properties and Perspectives for Bioapplications. *Crit. Rev. Solid State Mater. Sci.* **2009**, *34* (1–2), 18–74. https://doi.org/10.1080/10408430902831987.

(43)   Mochalin, V. N.; Shenderova, O.; Ho, D.; Gogotsi, Y. The Properties and Applications of Nanodiamonds. *Nat. Nanotechnol.* **2012**, *7* (1), 11–23. https://doi.org/10.1038/nnano.2011.209.

(44)   Man, H. B.; Ho, D. Nanodiamonds as Platforms for Biology and Medicine. *J. Lab. Autom.* **2013**, *18* (1), 12–18. https://doi.org/10.1177/2211068212456198.

(45)   Chen, Y.-C.; Tsai, C.-Y.; Lee, C.-Y.; Lin, I.-N. In Vitro and in Vivo Evaluation of Ultrananocrystalline Diamond as an Encapsulation Layer for Implantable Microchips. *Acta Biomater.* **2014**, *10* (5), 2187–2199. https://doi.org/10.1016/j.actbio.2014.01.014.

(46)   Shkurupy, V. A.; Arkhipov, S. A.; Neshchadim, D. V.; Akhramenko, E. S.; Troitskii, A. V. In Vitro Effects of Nanosized Diamond Particles on Macrophages. *Bull. Exp. Biol. Med.* **2015**, *158* (4), 500–503. https://doi.org/10.1007/s10517-015-2794-z.

(47)   Kurantowicz, N.; Strojny, B.; Sawosz, E.; Jaworski, S.; Kutwin, M.; Grodzik, M.; Wierzbicki, M.; Lipińska, L.; Mitura, K.; Chwalibog, A. Biodistribution of a High Dose of Diamond, Graphite, and Graphene Oxide Nanoparticles After Multiple Intraperitoneal Injections in Rats. *Nanoscale Res. Lett.* **2015**, *10* (1), 398. https://doi.org/10.1186/s11671-015-1107-9.

(48)   Yuan, Y.; Wang, X.; Jia, G.; Liu, J.-H.; Wang, T.; Gu, Y.; Yang, S.-T.; Zhen, S.; Wang, H.; Liu, Y. Pulmonary Toxicity and Translocation of Nanodiamonds in Mice. *Diam. Relat. Mater.* **2010**, *19* (4), 291–299. https://doi.org/10.1016/j.diamond.2009.11.022.

(49)   Thomas, V.; Halloran, B. A.; Ambalavanan, N.; Catledge, S. A.; Vohra, Y. K. In Vitro Studies on the Effect of Particle Size on Macrophage Responses to Nanodiamond Wear Debris. *Acta Biomater.* **2012**, *8* (5), 1939–1947. https://doi.org/10.1016/j.actbio.2012.01.033.

(50)   Vaijayanthimala, V.; Cheng, P.-Y.; Yeh, S.-H.; Liu, K.-K.; Hsiao, C.-H.; Chao, J.-I.; Chang, H.-C. The Long-Term Stability and Biocompatibility of Fluorescent Nanodiamond as an in Vivo Contrast Agent. *Biomaterials* **2012**, *33* (31), 7794–7802. https://doi.org/10.1016/j.biomaterials.2012.06.084.

(51)   Zhao, X.; Liu, R. Recent Progress and Perspectives on the Toxicity of Carbon Nanotubes at Organism, Organ, Cell, and Biomacromolecule Levels. *Environ. Int.* **2012**, *40*, 244–255. https://doi.org/10.1016/j.envint.2011.12.003.

(52)   Nel, A.; Xia, T.; Madler, L.; Li, N. Toxic Potential of Materials at the Nanolevel. *Science* **2006**, *311* (5761), 622–627. https://doi.org/10.1126/science.1114397.

(53)   Lewinski, N.; Colvin, V.; Drezek, R. Cytotoxicity of Nanoparticles. *Small* **2008**, *4* (1), 26–49. https://doi.org/10.1002/smll.200700595.

(54)   Moghimi, S. M.; Andersen, A. J.; Ahmadvand, D.; Wibroe, P. P.; Andresen, T. L.; Hunter, A. C. Material Properties in Complement Activation. *Adv. Drug Deliv. Rev.* **2011**, *63* (12), 1000–1007. https://doi.org/10.1016/j.addr.2011.06.002.

(55)   Alawdi, S. H.; El-Denshary, E. S.; Safar, M. M.; Eidi, H.; David, M.-O.; Abdel-Wahhab, M.
         A. Neuroprotective Effect of Nanodiamond in Alzheimer's Disease Rat Model: A Pivotal
         Role for Modulating NF-KB and STAT3 Signaling. *Mol. Neurobiol.* **2017**, *54* (3), 1906–
         1918. https://doi.org/10.1007/s12035-016-9762-0.

(56)   Lim, D. G.; Kim, K. H.; Kang, E.; Lim, S. H.; Ricci, J.; Sung, S. K.; Kwon, M. T.; Jeong, S.
         H. Comprehensive evaluation of carboxylated nanodiamond as a topical drug delivery system
         https://www.dovepress.com/comprehensive-evaluation-of-carboxylated-nanodiamond-as-a-
         topical-drug-peer-reviewed-fulltext-article-IJN (accessed Sep 12, 2017).
         https://doi.org/10.2147/IJN.S104859.

(57)   Liu, Z.; Tabakman, S.; Welsher, K.; Dai, H. Carbon Nanotubes in Biology and Medicine: In
         Vitro and in Vivo Detection, Imaging and Drug Delivery. *Nano Res.* **2009**, *2* (2), 85–120.
         https://doi.org/10.1007/s12274-009-9009-8.

(58)   García-Hevia, L.; Villegas, J. C.; Fernández, F.; Casafont, Í.; González, J.; Valiente, R.;
         Fanarraga, M. L. Multiwalled Carbon Nanotubes Inhibit Tumor Progression in a Mouse
         Model. *Adv. Healthc. Mater.* **2016**, *5* (9), 1080–1087.
         https://doi.org/10.1002/adhm.201500753.

(59)   Antaris, A. L.; Robinson, J. T.; Yaghi, O. K.; Hong, G.; Diao, S.; Luong, R.; Dai, H. Ultra-
         Low Doses of Chirality Sorted (6,5) Carbon Nanotubes for Simultaneous Tumor Imaging and
         Photothermal Therapy. *Acs Nano* **2013**, *7* (4), 3644–3652.
         https://doi.org/10.1021/nn4006472.

(60)   Kafa, H.; Wang, J. T.-W.; Rubio, N.; Venner, K.; Anderson, G.; Pach, E.; Ballesteros, B.;
         Preston, J. E.; Abbott, N. J.; Al-Jamal, K. T. The Interaction of Carbon Nanotubes with an
         in Vitro Blood-Brain Barrier Model and Mouse Brain in Vivo. *Biomaterials* **2015**, *53*, 437–
         452. https://doi.org/10.1016/j.biomaterials.2015.02.083.

(61)   Mackiewicz, N.; Gravel, E.; Garofalakis, A.; Ogier, J.; John, J.; Dupont, D. M.; Gombert, K.;
         Tavitian, B.; Doris, E.; Duconge, F. Tumor-Targeted Polydiacetylene Micelles for In Vivo
         Imaging and Drug Delivery. *Small* **2011**, *7* (19), 2786–2792.
         https://doi.org/10.1002/smll.201100212.

(62)   Richard, C.; Balavoine, F.; Schultz, P.; Ebbesen, T. W.; Mioskowski, C. Supramolecular
         Self-Assembly of Lipid Derivatives on Carbon Nanotubes. *Science* **2003**, *300* (5620), 775–
         778. https://doi.org/10.1126/science.1080848.

(63)   Sèle, C.; Gabel, F.; Gutsche, I.; Ivanov, I.; Burmeister, W. P.; Iseni, F.; Tarbouriech, N. Low-
         Resolution Structure of Vaccinia Virus DNA Replication Machinery. *J. Virol.* **2013**, *87* (3),
         1679–1689. https://doi.org/10.1128/JVI.01533-12.

(64)   Fultz, B.; Howe, J. M. *Transmission Electron Microscopy and Diffractometry of Materials*,
         Springer-Verlag Berline Heidelbert, **2013**.

(65)   Vincent, R.; Midgley, P. A. Double Conical Beam-Rocking System for Measurement of
         Integrated Electron Diffraction Intensities. *Ultramicroscopy* **1994**, *53* (3), 271–282.
         https://doi.org/10.1016/0304-3991(94)90039-6.

(66)   Mugnaioli, E.; Gorelik, T.; Kolb, U. "Ab Initio" Structure Solution from Electron Diffraction
         Data Obtained by a Combination of Automated Diffraction Tomography and Precession
         Technique. *Ultramicroscopy* **2009**, *109* (6), 758–765.
         https://doi.org/10.1016/j.ultramic.2009.01.011.

(67)   White, T. A.; Eggeman, A. S.; Midgley, P. A. Is Precession Electron Diffraction
         Kinematical? Part I:: "Phase-Scrambling" Multislice Simulations. *Ultramicroscopy* **2010**, *110*
         (7), 763–770. https://doi.org/10.1016/j.ultramic.2009.10.013.

(68)   Zhang, D.; Oleynikov, P.; Hovmöller, S.; Zou, X. Collecting 3D Electron Diffraction Data by
         the Rotation Method. *Z. Für Krist.* **2010**, *225* (2–3), 94–102.
         https://doi.org/10.1524/zkri.2010.1202.

(69)   Wan, W.; Sun, J.; Su, J.; Hovmoller, S.; Zou, X. Three-Dimensional Rotation Electron
         Diffraction: Software RED for Automated Data Collection and Data Processing. *J. Appl.
         Crystallogr.* **2013**, *46*, 1863–1873. https://doi.org/10.1107/S0021889813027714.

(70)   Shi, D.; Nannenga, B. L.; de la Cruz, M. J.; Liu, J.; Sawtelle, S.; Calero, G.; Reyes, F. E.;
         Hattne, J.; Gonen, T. The Collection of MicroED Data for Macromolecular Crystallography.
         Nat. Protoc. **2016**, *11* (5), 895–904. https://doi.org/10.1038/nprot.2016.046.

(71)   Nannenga, B. L.; Shi, D.; Leslie, A. G. W.; Gonen, T. High-Resolution Structure
          Determination by Continuous-Rotation Data Collection in MicroED. *Nat. Methods* **2014**, *11*
          (9), 927–930. https://doi.org/10.1038/NMETH.3043.
(72)   Hattne, J.; Reyes, F. E.; Nannenga, B. L.; Shi, D.; de la Cruz, M. J.; Leslie, A. G. W.; Gonen,
          T. MicroED Data Collection and Processing. *Acta Crystallogr. Sect. Found. Adv.* **2015**, *71*
          (4), 353–360. https://doi.org/10.1107/S2053273315010669.
(73)   Winn, M. D.; Ballard, C. C.; Cowtan, K. D.; Dodson, E. J.; Emsley, P.; Evans, P. R.; Keegan,
          R. M.; Krissinel, E. B.; Leslie, A. G. W.; McCoy, A.; et al. Overview of the CCP4 Suite and
          Current Developments. *Acta Crystallogr. D Biol. Crystallogr.* **2011**, *67* (4), 235–242.
          https://doi.org/10.1107/S0907444910045749.
(74)   CCP4: Software for Macromolecular Crystallography http://www.ccp4.ac.uk/ (accessed Feb
          8, 2017).
(75)   Nannenga, B. L.; Gonen, T. MicroED Opens a New Era for Biological Structure
          Determination. *Curr. Opin. Struct. Biol.* **2016**, *40*, 128–135.
          https://doi.org/10.1016/j.sbi.2016.09.007.
(76)   Yonekura, K.; Kato, K.; Ogasawara, M.; Tomita, M.; Toyoshima, C. Electron
          Crystallography of Ultrathin 3D Protein Crystals: Atomic Model with Charges. *Proc. Natl.
          Acad. Sci.* **2015**, *112* (11), 3368–3373. https://doi.org/10.1073/pnas.1500724112.
(77)   Hattne, J.; Shi, D.; Cruz, M. J. de la; Reyes, F. E.; Gonen, T. Modeling Truncated Pixel
          Values of Faint Reflections in MicroED Images. *J. Appl. Crystallogr.* **2016**, *49* (3), 1029–
          1034. https://doi.org/10.1107/S1600576716007196.
(78)   Yano, J.; Kern, J.; Irrgang, K.-D.; Latimer, M. J.; Bergmann, U.; Glatzel, P.; Pushkar, Y.;
          Biesiadka, J.; Loll, B.; Sauer, K.; et al. X-Ray Damage to the Mn4Ca Complex in Single
          Crystals of Photosystem II: A Case Study for Metalloprotein Crystallography. *Proc. Natl.
          Acad. Sci. U. S. A.* **2005**, *102* (34), 12047–12052. https://doi.org/10.1073/pnas.0505207102.
(79)   Rodriguez, J. A.; Ivanova, M. I.; Sawaya, M. R.; Cascio, D.; Reyes, F. E.; Shi, D.; Sangwan,
          S.; Guenther, E. L.; Johnson, L. M.; Zhang, M.; et al. Structure of the Toxic Core of Alpha-
          Synuclein from Invisible Crystals. *Nature* **2015**, *525* (7570), 486-+.
          https://doi.org/10.1038/nature15368.
(80)   Sawaya, M. R.; Rodriguez, J.; Cascio, D.; Collazo, M. J.; Shi, D.; Reyes, F. E.; Hattne, J.;
          Gonen, T.; Eisenberg, D. S. Ab Initio Structure Determination from Prion Nanocrystals at
          Atomic Resolution by MicroED. *Proc. Natl. Acad. Sci. U. S. A.* **2016**, *113* (40), 11232–
          11236. https://doi.org/10.1073/pnas.1606287113.
(81)   Clabbers, M. T. B.; Abrahams, J. P. Electron Diffraction and Three-Dimensional
          Crystallography for Structural Biology. *Crystallogr. Rev.* **2018**, *24* (3), 176–204.
          https://doi.org/10.1080/0889311X.2018.1446427.
(82)   Sinkler, W.; Marks, L. D.; Edwards, D. D.; Mason, T. O.; Poeppelmeier, K. R.; Hu, Z.;
          Jorgensen, J. D. Determination of Oxygen Atomic Positions in a Ga–In–Sn–O Ceramic Using
          Direct Methods and Electron Diffraction. *J. Solid State Chem.* **1998**, *136* (1), 145–149.
          https://doi.org/10.1006/jssc.1998.7804.
(83)   Engilberge, S.; Riobe, F.; Di Pietro, S.; Lassalle, L.; Coquelle, N.; Arnaud, C.-A.; Pitrat, D.;
          Mulatier, J.-C.; Madern, D.; Breyton, C.; et al. Crystallophore: A Versatile Lanthanide
          Complex for Protein Crystallography Combining Nucleating Effects, Phasing Properties, and
          Luminescence. *Chem. Sci.* **2017**, *8* (9), 5909–5917. https://doi.org/10.1039/c7sc00758b.
(84)   Foos, N.; Seuring, C.; Schubert, R.; Burkhardt, A.; Svensson, O.; Meents, A.; Chapman, H.
          N.; Nanao, M. H. X-Ray and UV Radiation-Damage-Induced Phasing Using Synchrotron
          Serial Crystallography. *Acta Crystallogr. Sect. Struct. Biol.* **2018**, *74* (Pt 4), 366–378.
          https://doi.org/10.1107/S2059798318001535.
(85)   Trapani, S.; Schoehn, G.; Navaza, J.; Abergel, C. Macromolecular Crystal Data Phased by
          Negative-Stained Electron-Microscopy Reconstructions. *Acta Crystallogr. Sect. D* **2010**, *66*
          (5), 514–521. https://doi.org/10.1107/S0907444910002763.
(86)   Sleutel, M.; Van Driessche, A. E. S. Nucleation of Protein Crystals - a Nanoscopic
          Perspective. *Nanoscale* **2018**, *10* (26), 12256–12267. https://doi.org/10.1039/c8nr02867b.
(87)   De Zorzi, R.; Nicholson, W. V.; Guigner, J.-M.; Erne-Brand, F.; Stahlberg, H.; Venien-
          Bryan, C. Growth of Large and Highly Ordered 20 Crystals of a K+ Channel, Structural Role

(88) Fan, G. y.; Maldonado, F.; Zhang, Y.; Kincaid, R.; Ellisman, M. H.; Gastinel, L. N. In Vivo Calcineurin Crystals Formed Using the Baculovirus Expression System. *Microsc. Res. Tech.* **1996**, *34* (1), 77–86. https://doi.org/10.1002/(SICI)1097-0029(19960501)34:1<77::AID-JEMT11>3.0.CO;2-M.

(89) Koopmann, R.; Cupelli, K.; Redecke, L.; Nass, K.; DePonte, D. P.; White, T. A.; Stellato, F.; Rehders, D.; Liang, M.; Andreasson, J.; et al. In Vivo Protein Crystallization Opens New Routes in Structural Biology. *Nat. Methods* **2012**, *9* (3), 259–262. https://doi.org/10.1038/nmeth.1859.

(90) Schoenherr, R.; Klinge, M.; Rudolph, J. M.; Fita, K.; Rehders, D.; Luebber, F.; Schneegans, S.; Majoul, I. V.; Duszenko, M.; Betzel, C.; et al. Real-Time Investigation of Dynamic Protein Crystallization in Living Cells. *Struct. Dyn.* **2015**, *2* (4), 041712. https://doi.org/10.1063/1.4921591.

(91) Duszenko, M.; Redecke, L.; Mudogo, C. N.; Sommer, B. P.; Mogk, S.; Oberthuer, D.; Betzel, C. *In Vivo* Protein Crystallization in Combination with Highly Brilliant Radiation Sources Offers Novel Opportunities for the Structural Analysis of Post-Translationally Modified Eukaryotic Proteins. *Acta Crystallogr. Sect. F Struct. Biol. Commun.* **2015**, *71* (8), 929–937. https://doi.org/10.1107/S2053230X15011450.

(92) Dbouk, H. A.; Mroue, R. M.; El-Sabban, M. E.; Talhouk, R. S. Connexins: A Myriad of Functions Extending beyond Assembly of Gap Junction Channels. *Cell Commun. Signal.* **2009**, *7* (1), 4. https://doi.org/10.1186/1478-811X-7-4.

(93) Gilula, N. B.; Reeves, O. R.; Steinbach, A. Metabolic Coupling, Ionic Coupling and Cell Contacts. *Nature* **1972**, *235* (5336), 262–265. https://doi.org/10.1038/235262a0.

(94) Sáez, J. C.; Leybaert, L. Hunting for Connexin Hemichannels. *FEBS Lett.* **2014**, *588* (8), 1205–1211. https://doi.org/10.1016/j.febslet.2014.03.004.

(95) Saez, J. C.; Berthoud, V. M.; Branes, M. C.; Martinez, A. D.; Beyer, E. C. Plasma Membrane Channels Formed by Connexins: Their Regulation and Functions. *Physiol. Rev.* **2003**, *83* (4), 1359–1400. https://doi.org/10.1152/physrev.00007.2003.

(96) Retamal, M. A.; Reyes, E. P.; García, I. E.; Pinto, B.; Martínez, A. D.; González, C. Diseases Associated with Leaky Hemichannels. *Front. Cell. Neurosci.* **2015**, *9*. https://doi.org/10.3389/fncel.2015.00267.

(97) Condorelli, D. F.; Parenti, R.; Spinella, F.; Salinaro, A. T.; Belluardo, N.; Cardile, V.; Cicirata, F. Cloning of a New Gap Junction Gene (Cx36) Highly Expressed in Mammalian Brain Neurons. *Eur. J. Neurosci.* **1998**, *10* (3), 1202–1208. https://doi.org/10.1046/j.1460-9568.1998.00163.x.

(98) Belluardo, N.; Mudò, G.; Trovato-Salinaro, A.; Le Gurun, S.; Charollais, A.; Serre-Beinier, V.; Amato, G.; Haefliger, J.-A.; Meda, P.; Condorelli, D. F. Expression of Connexin36 in the Adult and Developing Rat Brain1. *Brain Res.* **2000**, *865* (1), 121–138. https://doi.org/10.1016/S0006-8993(00)02300-3.

(99) Serre-Beinier, V.; Gurun, S. L.; Belluardo, N.; Trovato-Salinaro, A.; Charollais, A.; Haefliger, J. A.; Condorelli, D. F.; Meda, P. Cx36 Preferentially Connects Beta-Cells within Pancreatic Islets. *Diabetes* **2000**, *49* (5), 727–734. https://doi.org/10.2337/diabetes.49.5.727.

(100) Connors, B. W.; Long, M. A. Electrical Synapses in the Mammalian Brain. *Annu. Rev. Neurosci.* **2004**, *27* (1), 393–418. https://doi.org/10.1146/annurev.neuro.26.041002.131128.

(101) Pereda, A. E.; Curti, S.; Hoge, G.; Cachope, R.; Flores, C. E.; Rash, J. E. Gap Junction-Mediated Electrical Transmission: Regulatory Mechanisms and Plasticity. *Biochim. Biophys. Acta BBA - Biomembr.* **2013**, *1828* (1), 134–146. https://doi.org/10.1016/j.bbamem.2012.05.026.

(102) Pereda, A. E. Electrical Synapses and Their Functional Interactions with Chemical Synapses. *Nat. Rev. Neurosci.* **2014**, *15* (4), 250–263. https://doi.org/10.1038/nrn3708.

(103) Deans, M. R.; Gibson, J. R.; Sellitto, C.; Connors, B. W.; Paul, D. L. Synchronous Activity of Inhibitory Networks in Neocortex Requires Electrical Synapses Containing Connexin36. *Neuron* **2001**, *31* (3), 477–485. https://doi.org/10.1016/S0896-6273(01)00373-7.

(104) DeVries, S. H.; Qi, X.; Smith, R.; Makous, W.; Sterling, P. Electrical Coupling between Mammalian Cones. *Curr. Biol.* **2002**, *12* (22), 1900–1907. https://doi.org/10.1016/S0960-9822(02)01261-7.

(105) Hormuzdi, S. G.; Pais, I.; LeBeau, F. E. N.; Towers, S. K.; Rozov, A.; Buhl, E. H.; Whittington, M. A.; Monyer, H. Impaired Electrical Signaling Disrupts Gamma Frequency Oscillations in Connexin 36-Deficient Mice. *Neuron* **2001**, *31* (3), 487–495. https://doi.org/10.1016/S0896-6273(01)00387-7.

(106) LeBeau, F. E. N.; Traub, R. D.; Monyer, H.; Whittington, M. A.; Buhl, E. H. The Role of Electrical Signaling via Gap Junctions in the Generation of Fast Network Oscillations. *Brain Res. Bull.* **2003**, *62* (1), 3–13. https://doi.org/10.1016/j.brainresbull.2003.07.004.

(107) Belousov, A. B.; Fontes, J. D. Neuronal Gap Junctions: Making and Breaking Connections during Development and Injury. *Trends Neurosci.* **2013**, *36* (4), 227–236. https://doi.org/10.1016/j.tins.2012.11.001.

(108) Bissiere, S.; Zelikowsky, M.; Ponnusamy, R.; Jacobs, N. S.; Blair, H. T.; Fanselow, M. S. Electrical Synapses Control Hippocampal Contributions to Fear Learning and Memory. *Science* **2011**, *331* (6013), 87–91. https://doi.org/10.1126/science.1193785.

(109) Contreras, J. E.; Sánchez, H. A.; Véliz, L. P.; Bukauskas, F. F.; Bennett, M. V. L.; Sáez, J. C. Role of Connexin-Based Gap Junction Channels and Hemichannels in Ischemia-Induced Cell Death in Nervous Tissue. *Brain Res. Brain Res. Rev.* **2004**, *47* (0), 290–303. https://doi.org/10.1016/j.brainresrev.2004.08.002.

(110) Wang, Y.; Denisova, J. V.; Kang, K. S.; Fontes, J. D.; Zhu, B. T.; Belousov, A. B. Neuronal Gap Junctions Are Required for NMDA Receptor–Mediated Excitotoxicity: Implications in Ischemic Stroke. *J. Neurophysiol.* **2010**, *104* (6), 3551–3556. https://doi.org/10.1152/jn.00656.2010.

(111) Guldenagel, M.; Ammermuller, J.; Feigenspan, A.; Teubner, B.; Degen, J.; Sohl, G.; Willecke, K.; Weiler, R. Visual Transmission Deficits in Mice with Targeted Disruption of the Gap Junction Gene Connexin36. *J. Neurosci.* **2001**, *21* (16), 6036–6044.

(112) Wellershaus, K.; Degen, J.; Deuchars, J.; Theis, M.; Charollais, A.; Caille, D.; Gauthier, B.; Janssen-Bienhold, U.; Sonntag, S.; Herrera, P.; et al. A New Conditional Mouse Mutant Reveals Specific Expression and Functions of Connexin36 in Neurons and Pancreatic Beta-Cells. *Exp. Cell Res.* **2008**, *314* (5), 997–1012. https://doi.org/10.1016/j.yexcr.2007.12.024.

(113) Yeager, M.; Nicholson, B. J. Structure and Biochemistry of Gap Junctions; Biology, B.-A. in M. and C., Ed.; Gap Junctions; Elsevier, 2000; Vol. 30, pp 31–98. https://doi.org/10.1016/S1569-2558(00)30003-0.

(114) Pogoda, K.; Kameritsch, P.; Retamal, M. A.; Vega, J. L. Regulation of Gap Junction Channels and Hemichannels by Phosphorylation and Redox Changes: A Revision. *BMC Cell Biol.* **2016**, *17* (1), 11. https://doi.org/10.1186/s12860-016-0099-3.

(115) Colletier, J.-P.; Sawaya, M. R.; Gingery, M.; Rodriguez, J. A.; Cascio, D.; Brewster, A. S.; Michels-Clark, T.; Hice, R. H.; Coquelle, N.; Boutet, S.; et al. De Novo Phasing with X-Ray Laser Reveals Mosquito Larvicide BinAB Structure. *Nature* **2016**, *539* (7627), 43–47. https://doi.org/10.1038/nature19825.

(116) Butko, P. Cytolytic Toxin Cyt1A and Its Mechanism of Membrane Damage: Data and Hypotheses. *Appl Env. Microbiol* **2003**, *69* (5), 2415–2422. https://doi.org/10.1128/AEM.69.5.2415-2422.2003.

(117) Jones, C. G.; Martynowycz, M. W.; Hattne, J.; Fulton, T. J.; Stoltz, B. M.; Rodriguez, J. A.; Nelson, H. M.; Gonen, T. The CryoEM Method MicroED as a Powerful Tool for Small Molecule Structure Determination. *Acs Cent. Sci.* **2018**, *4* (11), 1587–1592. https://doi.org/10.1021/acscentsci.8b00760.

(118) Martynowycz, M. W.; Zhao, W.; Hattne, J.; Jensen, G. J.; Gonen, T. Collection of Continuous Rotation MicroED Data from Ion Beam-Milled Crystals of Any Size. *Structure* **2019**, *27* (3), 545-548.e2. https://doi.org/10.1016/j.str.2018.12.003.

(119) Sandroni, M.; Gueret, R.; Wegner, K. D.; Reiss, P.; Fortage, J.; Aldakov, D.; Collomb, M.-N. Cadmium-Free CuInS2/ZnS Quantum Dots as Efficient and Robust Photosensitizers in Combination with a Molecular Catalyst for Visible Light-Driven H2 Production in Water. *Energy Environ. Sci.* **2018**. https://doi.org/10.1039/C8EE00120K.

(120)   Reiss, P.; Carrière, M.; Lincheneau, C.; Vaure, L.; Tamang, S. Synthesis of Semiconductor Nanocrystals, Focusing on Nontoxic and Earth-Abundant Materials. *Chem. Rev.* **2016**, *116* (18), 10731–10819. https://doi.org/10.1021/acs.chemrev.6b00116.

Appendix
Curriculum Vitae

WAI LI WINNIE LING
E-mail: wai-li.ling@ibs.fr
ResearcherID:F-9823-2012
ORCID 0000-0002-4264-5750

EDUCATION
   University of California at Berkeley, U.S.
      PhD in Condensed Matter Physics Experiment December 20, 2001
      MA in Physics December 17, 1998
   University of Chicago, U.S.
      BA in Physics and Mathematics with honors June 11, 1994

EXPERIENCE
   Institut de Biologie Structurale, Grenoble, France
Research Scientist, Laboratory of Electron Microscopy and Methods January, 2009-present
CEA Expert senior in Instrumentation and Characterization (Electron Microscopy) since December, 2013
Institut de Biologie Structurale Jean-Pierre Ebel/Leti- CEA, Grenoble, France
Limited-Term Research Scientist, Transverse Nanoscience Program April, 2007-October, 2008
University of California at San Francisco, San Francisco, California, U.S.A.
Postdoctoral Researcher, Department of Biochemistry and Biophysics 2005-2006
*   developed techniques to realize tomography of vitreous sections in cryo-TEM to discern cellular structures in their native states.
Sandia National Laboratories, Livermore, California, U.S.A.
Postdoctoral Researcher**,** Materials Physics Group 2001-2005
*   studied surface structure and dynamics, visualized in real time, nucleation, strain relief, and corrosion in hetero-epitaxial films.
Lawrence Berkeley National Laboratory, Berkeley, California, U.S.A.
Graduate Student Researcher, Advanced Light Source 1998-2001
*   investigated multilayer magnetic nanostructures fabricated with continuous thickness variation to better understand magnetic coupling and spin-reorientation transition.
Graduate Student Researcher, Materials Science Division 1995-1998
*   investigated correlation between magnetic and structural properties, leading to improved magnetism in thin cobalt films using oxygen surfactant.
*   designed and built UHV chamber with scanning tunneling microscopy, molecular beam epitaxy, variable temperature sample holder, and sample transfer system, that enabled structural studies of thin film growth with atomic resolution.
University of Chicago, Chicago, Illinois, U.S.A.
Undergraduate Researcher Assistant, Department of Physics 1993-1994
*   completed subroutines for searching the signature of Dalitz decay.
General Atomics, San Diego, California, U.S.A.
Summer Student Researcher, Fusion Group summer 1992
*   modified programs to generate different modes of Alvén waves in tokamak.
University of Chicago, Chicago, Illinois, U.S.A.
Summer Student Researcher, Dr. Haselkorn Lab summer 1991
*   created vector for studying D1 protein in photosystem II.

HONORS
   ∗   **Sandia National Laboratories Recognitions Award** 2005
   ∗   **Associate member of Sigma Xi** 1994
   ∗   **Member of Phi Beta Kappa** 1993
   ∗   **Student Marshall, University of Chicago** 1993

FELLOWSHIPS
* **Department of Education Fellowship** 1994-1995, 1999-2000
* **Princeton Program of Plasma Physics Summer Fellowship** 1992
* **Howard Hughes Summer Research Grant** 1991
* **Sir Y.K. Pao Fellowship** 1990-1994

FUNDED PROJECTS
* **CEA-DRF-impulsion** 2018-2019 (Coordinator)
  Cryo-ME NP *"Cryo-microscopie électronique et diffraction électronique de nouvelles nanoparticules"*
* **CEA-DRF-impulsion** 2017-2018 (Partner)
  Hybridimer "Dimère hybride nanocristal semiconducteur-nanobâtonnet d'or lié par l'ADN pour contrôler l'émission de photons"
* **CEA-PE Bottom up** 2017-2018 (Partner)
  DEMS "Diffraction électronique et matériaux sensibles"
* **IBS-Internal Funding** 2017 (Coordinator)
  "Cryo-electron diffraction of protein nanocrystals"
* **ANR** 2017-2020 (Team Member)
  C1qEffero "C1q-mediated efferocytosis: from molecular and cellular mechanisms to self-tolerance or autoimmunty"
* **ANR** 2014-2017 (Partner)
  Replipox "Structural and functional elucidation of the poxvirus genome replication process"
* **CEA-Programme Trasnversal Toxicologie** 2013-2016 (Coordinator)
  NanoImmunoTox "Towards the prediction of immunotoxicity in human upon first contact with carbon nanomaterials"

TEACHING
Tutor in Mathematics, San Quentin Prison College Program (Patten University) 2002
* helped students with mathematics problems and cultivated collaboration among students.

Instructor for Summer Research Interns, Lawrence Berkeley National Laboratory 1995
* independently developed lesson plan and delivered lectures on selected research topics in modern science.

Graduate Student Instructor, Physics Department, University of California at Berkeley 1994-1995
* led discussion sessions and directed laboratory sections in general physics class.

Tutor in Science and Mathematics, Excel Program for Girls in High-school 1995
* helped high school students with school works and organized activities to build self-confidence.

Grader, Mathematics Department, University of Chicago 1991-1994
* graded homework and assisted in final grade assignment in undergraduate level courses.

Introduction to Emerging Methods at IBS 5 Dec 2012, 3 Mar 2015, 6 Dec 2017 (1hr lecture)
* "Electron Tomography"

INVITED PRESENTATIONS
* **Midi MINATEC** 16 November 2018
  "Does our innate immune system react to carbon nanotubes and nanodiamonds?"
* **Journée Scientifique d'IBS 2018 Faits Marquants** 7 June 2018
  "3-dim electron diffraction of nano-sized peptide and protein crystals"
* **L'Ecole de <Giens> 2017 Groupe Interdisciplinaire pour l'étude des effets environnmentaux des nanotechnologies** 16-18 Oct 2017
  "L'interaction d'une protéine immunitaire avec les nanotubes de carbon"
* **Seminar of the Instituto de Química Física "Rocasolano", CSIC, Madrid, Spain** 23 Dec 2016
  "Structural studies of the vaccinia virus helicase-primase D5 with electron microscopy"
* **Séminaires du Service de Bioénergétique, Biologie Structurale et Mécanismes, CNRS, Saclay, France** 24 Aug 2016
  "Structural studies of the vaccinia virus helicase-primase D5 with electron microscopy"
* **PennScience seminar, University of Pennsylvania, Philadelphia, US** 17 Feb 2016
  "Interactions of carbon nanotubes and nanodiamonds with the human complement"
* **Journées nanosciences du CEA** Dec 2010
  "Une nouvelle technique présente à l'IBS: MET cryogénique"

OTHER PROFESSIONAL ACTIVITIES

    Organizer PSB (Partnership for Structural Biology) School in Cryo-Electron Microscopy 2018
    Consultant CERIC-Europena Research Infrastructure Consortiu**m** 2016
    Jury Meeting of the Doctoral School of Chemistry and Life Sciences, Grenoble Alps Uiversity 2016
    Instructor Fete de la Science 2016

TECHNIQUES

cryo-transmission electron microscopy (cryo-TEM); electron diffraction; electron tomography; scanning TEM (STEM); cryo-ultramicrotomy; high pressure freezing (HPF); scanning tunneling microscopy (STM); low energy electron microscopy (LEEM); angle-resolved photoemission spectroscopy (ARPES); photoemission electron microscopy (PEEM); magneto-optic Kerr effect (MOKE); molecular beam epitaxy (MBE); Auger electron spectroscopy (AES); ultra-high vacuum (UHV).

ADDITIONAL TRAININGS

* **Janelia MicroED Workshop** 21-25 Feb, 2016, Janelia Research Campus, VA, U.S.
* **MATLAB Les fondamentaux, Traitement et visualisation de donnees** 8-10, 24 March, 2016, CNRS, Grenoble
* **MXIS Practical course on in-plate crystallography and in situ** 17 Nov au 19 Nov, 2015, CBS, Grenoble
* **Electron Microscopy Reconstruction** with P. Penczek, 4 days, EMBL, Grenoble
* **Single particle analysis** with I. Gutsche, 2 weeks, EMBL, Grenoble
* **MATLAB Traitement d'Image** 3 oct au 5 oct, 2011, CNRS, Grenoble
* **Java** May 2011 (35 hrs) CNRS, Grenoble
* **EMBO Practical Course on Cryo-Electron Microscopy and 3D-Image Analysis** Aug 24-31, 2008, EMBL Heidelberg
* **Vitreous Cryo Course** Jan 17-19, 2006, EM Lab, UC Berkeley
* **Cryo Electron Microscopy Course** June 7-16, 2005, University of British Columbia in Vancouver
* **Student Machine Shop Training Course** completed Aug 16, 1996, Physics Dept., UC Berkeley
* **Practical Electronics** completed June 30, 1995, Physics Dept., UC Berkeley
* **International Graduate Student Instructor Training Course** 1995, UC Berkeley
* **Graduate Student Instructor Training Conference** Fall 1994, UC Berkeley

LANGUAGES

English, Chinese, French (B2 du CECR), one-year college-level Spanish

OTHERS

    Organizer of barre au sol section of AAC CEA 2018-present
    Secretary of ice-skating section of AS CEA/ST 2017-present
    Women Leaders 2006: A Symposium for Women in University Settings
    Survival Skills for Successful Women Physicists Workshop, American Physical Society 2004

42 Wegner, K.D., Pouget, S., Ling, W.L. Carrière, M., and Reiss, P.
"Gallium -- a versatile element for tuning the photoluminescence properties of InP quantum dots."
Chemical Communications 55, 1663-1666 (2019) DOI: 10.1039/c8cc09740b

41 Caputo, F., Arnould, A., Bacia, M., Ling, W.L. Rustique, E., Texier, I., Mello, A.P., Couffin, A.-C.
"Measuring particle size distribution by asymmetric flow field flow fractionation: a powerful method for the pre-clinical characterization of lipid-based nanoparticles."
Molecular Pharmaceutics 16, 756-767 (2019)

40. Belime, A., Thielens, N.M., Gravel, E., Frachet, P., Ancelet, S., Tacnet, P., Caneiro, C., Chuprin, J., Gaboriaud, C., Schoehn, G., Doris, E., Ling, W.L.
"Recognition protein C1q of innate immunity agglutinates nanodiamonds without activating complement."
Nanomedicine: Nanotechnology, Biology, and Medicine (accepted)

39. Mizuta, R., Devos, J.M., Webster, J., Ling, W.L., Narayanan, T., Round, A., Munnur, D., Mossou, E., Farahat, A.A,, Boykin, D.W., Wilson, W.D., Neidle, S., Schweins, R., Rannou, P., Haertlein, M., Forsyth, V.T., and Mitchell, E.P.
"Dynamic self-assembly of DNA minor groove-binding ligand DB921 into nanotubes triggered by an alkali halide."
Nanoscale 10, 5550-5558 (2018)

38. Thielens, N., Belime, A., Gravel, E., Ancelet, S., Caneiro, C., Doris, E., Ling, W.L.
"Impact of the surface charge of polydiacetylene micelles on their interaction with human innate immune protein C1q and the complement system."
International Journal of Pharmaceutics 536, 434-439 (2018)

37. Wojtas, D. H., Ayyer, K., Liang, M., Mossou, E., Romoli, F., Seuring, C., Beyerlein, K.R., Bean, R.J., Morgan, A.j., Oberthuer, D., Fleckenstein, H., Heymann, M., Gati, C., Yefanov, O., Barthelmess, M., Ornithopoulou, E., Galli, L., Xavier, P.L., Ling, W.L., Frank, M., Yoon, C.H., White, T.A., Bajt, S., Mitraki, A., Boutet, S., Aquila, A., Barty, A., Forsyth, V.T., Chapman, H.N., and Millane, R.P.
"Analysis of XFEL Serial Diffraction Data from Individual Crystalline Fibrils."
IUCrJ 4 (6):795–811. (2017)

36. Belime, A., Gravel, E., Brenet, S., Ancelet, S., Caneiro, C., Hou, Y., Thielens, N., Doris, E., Ling, W.L.
"Mode of PEG coverage on carbon nanotubes affects binding of innate immune protein C1q"
Journal of Physical Chemistry B 122, 757-763 (2018)

35. Arlaud, G.J., Gaboriaud, C., Ling, W.L., Thielens, N.
"Structure of the C1 complex of complement"
Proceedings of the National Academy of Sciences 114, E5766-5767 (2017)

34. Saint-Cricq, M., Carrete, J., Gaboriaud, C., Gravel, E., Doris, E., Thielens, N., Mingo, N., Ling, W.L.,
"Human Immune Protein C1q Selectively Disaggregates Carbon Nanotubes"
Nano Letters 17, 3409-3415 (2017)

33. Prakash, P., Gravel, E., Li, H., Miserque, F., Habert, A., den Hertog, M., Ling, W.L., Namboothiri, I.N.N., Doris, E.
"*Direct and co-catalytic oxidative aromatization of 1,4-dihydropyridines and related substrates using gold nanoparticles supported on carbon nanotubes*"
Catalysis Science and Technology 6, 6476-6479 (2016)

32. Hutin, S., Ling, W.L., Round, A., Effantin, G., Reich, S., Iseni, F., Tarbouriech, N., Schoehn, G., Burmeister, W.
"*Domain organization of vaccinia virus helicase-primase D5*"
Journal of Virology 90, 4604-13 (2016)

31. Gutsche, I., Desfosses, A., Effantin, G., <u>Ling, W.L.</u>, Haupt, M., Ruigrok, R.W.H., Sachse, C., Schoehn, G.
"*Near-atomic cryo-EM structure of the helical measles virus nucleocapsid*"
Science 348, 704-707 (2015)
30. Gaboriaud, C., <u>Ling, W.L.</u>, Thielens, N., Bally, I., Rossi, V.
"*Deciphering the fine details of C1 assembly and activaton mechanisms: "mission impossible"?*"
Frontiers in immunology 5, 565-569 (2014)
29. <u>Ling, W.L.</u>*, Cherns, P., Samuel, J., Raccurt, O., Poncelet, O., Chabli, A.
"*Z-contrast cryo-electron tomography probes shell porosity in multi-shell nanocomposites*"
Journal of Nanoparticle Research 14 (4), 806-812 (2012)
28. Mackiewicz, N., Bark, T., Cao, B., Delaire, J.A., Riehl, D., <u>Ling, W.L.</u>, Foillard, S., Doris, E.
"*Fullerene-functionalized carbon nanotubes as improved optical limiting devices*"
Carbon 49, 3998-4003 (2011)
27. Paidassi, H., Tacnet-Delorme, P., Verneret, M., Gaboriaud, C., Houen, G., Duus, D., <u>Ling, W.L.</u>, Arlaud, G.J., Frachet, P.
"*Investigations on the C1q/calreticulin/phosphatidylserine interactions yield new insights into apoptotic cell recognition*"
Journal of Molecular Biology 408 (2), 277-290 (2011)
26. <u>Ling, W.L.</u>*, Biro, A., Bally, I., Tacnet, P., Deniaud, A., Doris, E., Frachet, P., Schoehn, G., Pebay-Peyroula, E., Arlaud, G.
"*Proteins of the Innate Immune System Crystallize on Carbon Nanotubes but Are Not Activated*"
ACS Nano 5, 730-737 (2011)
25. Chouquet, A., Paidassi, H., <u>Ling, W.L.</u>, Frachet, P., Houen, G., Arlaud, G.J., Gaboriaud, C.
"*X-ray structure of the human calreticulin globular domain reveals a peptide-binding area and suggests a multi-molecular mechanism*"
PLoS ONE 6(3): e17886. doi:10.1371/journal.pone.0017886 (2011)
24. Arlaud, G. J., Biro, A., <u>Ling, W.L.</u>
"*Enzymatically modified low-density lipoprotein is recognized by C1q and activates the classical complement pathway*"
Journal of Lipids vol. 2011, Article ID 376092, 5 pages, 2011. Doi:10.1155/2011/376092 (2011)
23. Samuel, J., Raccurt, O., Poncelet, O., Auger, A., <u>Ling, W.L.</u>, Cherns, P., Grunwald, D., and Tillement, O.
"*Surface Characterizations of Fluorescent-Functionalized Silica Nanoparticles: from the Macroscale to the Nanoscale*"
Journal of Nanoparticle Research 12, 2255-2265 (2010)
22. Erlich, P., Dumestre-Pérard, C., <u>Ling, W.L.</u>, Lemaire-Vieille, C., Schoehn, G., Arlaud, G., Thielens, N.M., Gagnon, J., & Cesbron, J.-Y.
"*Complement protein C1q forms a complex with cytotoxic prion protein oligomers*"
Journal of Biological Chemistry 285, 19267-19276 (2010)
21. Samuel, J., Tallec, G., Cherns, P., <u>Ling, W.L.</u>, Raccurt, O., Poncelet, O., Imbert, D., and Mazzanti, M.
"*Lanthanide-chelate silica nanospheres as robust multicolor Vis-NIR tags*"
Royal Society of Chemistry Journal of Chemical Communications 46, 2647-2649, (2010)
20. Biro, A., <u>Ling, W.L.</u>, Arlaud, G. J.
"*Complement Protein C1q Recognizes Enzymatically Modified Low-Density Lipoprotein through Unesterified Fatty Acids Generated by Cholesterol Esterase*"
Biochemistry 49, 2167-2176 (2010)
19. Samuel, J., Raccurt, O., <u>Ling, W.L.</u>, Poncelet, O.
"*Autoreduction of Metallic Species on the Surface of Silica Nanoparticles by Surface Functionalization*"
2009MRS Fall Meeting Symposium N proceedings (Volume 1207E, 1207-N10-60) DOI: 10.1557/PROC-1207-N10-60
18. Erlich, P., Dumestre-Pérard, C., <u>Ling, W.L.</u>, Lemaire-Vieille, C., Arlaud, G., Gagnon, J., & Cesbron, J.-Y.
"*Prion protein oligomers and C1q recognition*"

Molecular Immunology 46**,** 2837 (2009)

17. <u>Ling, W.L.</u>, Hamilton, J.C., Thürmer, K., Thayer, G.E., de la Figuera, J., Hwang, R.Q., Carter, C.B., Bartelt, N.C., & McCarty, K.F.
"Herringbone and triangular patterns of dislocations in Ag, Au, and AgAu alloy films on Ru(0001)"
Surface Science 600**,** 1735-1757 (2006)

16. <u>Ling, W.L.</u>*, Bartelt, N.C., McCarty, K.F., & Carter, C.B.
"Twin boundaries can be moved by step edges during film growth"
Physical Review Letters 95, 166105 (2005)

15. El Gabaly, F., <u>Ling, W.L.</u>, McCarty, K.F., & de la Figuera, J.
"The importance of threading dislocations on the motion of domain boundaries in thin films"
Science 308 (5726): 1303-1305 (2005)

14. <u>Ling, W.L.</u>, Giessel, T., Thürmer, K., Hwang, R.Q., Bartelt, N.C., & McCarty, K.F.
"Crucial role of substrate steps in de-wetting of crystalline thin films"
Surface Science 570 (3): L297-L303 (2004)

13. <u>Ling, W.L.</u>, Bartelt, N.C., Pohl, K., de la Figuera, J., Hwang, R.Q., & McCarty, K.F.
"Enhanced self-diffusion on Cu(111) by trace amounts of S: chemical-reaction-limited kinetics"
Physical Review Letters 93, 166101 (2004)
-- mentioned in President Bush's 2005 Science budget

12. <u>Ling, W.L.</u>, de la Figuera, J., Bartelt, N.C., Hwang, R.Q., Schmid, A.K., Thayer, G.E., & Hamilton, J.C.
"Strain relief through heterophase interphase reconstruction: Ag(111)/Ru(0001)"
Physical Review Letters 92, 116102 (2004)

11. Choi, H.J., <u>Ling, W.L.</u>, Scholl, A., Wolfe, J.H., Bovensiepen, U., Toyama, F., & Qiu, Z.Q.
"Spin reorientation transition of Fe films in magnetically coupled Fe/Cu/Ni/Cu(001)"
Physical Review B 66, 014409 (2002)

10. <u>Ling, W.L.</u>, Rotenberg, Eli, Choi, H.J., Wolfe, J.H., Toyama, F., Paik, Silena, Smith, N.V., & Qiu, Z.Q.
"Double quantum well states in Cu/Co/Cu grown on Co(001)"
Physical Review B 65, 113406 (2002)

9. Man, K.L.; <u>Ling, W.L.</u>; Paik, Silena Y.; Poppa, H.; Altman, M.S., & Qiu, Z.Q.
"Modification of initial growth and magnetism in Fe/Cu(100)"
Physical Review B 65, 024409 (2002)

8. Wolfe, J.H.; Kawakami, R.K.; <u>Ling, W.L.</u>; Qiu, Z.Q.; Arias, R.; & Mills, D.L.
"Roughness induced in plane uniaxial anisotropy in ultrathin Fe films"
Journal of Magnetism and Magnetic Materials 232, 36 (2001)

7. <u>Ling, W.L.</u>, Qiu, Z.Q., Takeuchi, O., Ogletree, D.F. & Salmeron, M.
"Effect of oxygen surfactant on the magnetic and structural properties of Co films grown on Cu(110)"
Physical Review B 63, 024408 (2001)

6. <u>Ling, W.L.</u>, Takeuchi, O., Ogletree, D.F., Qiu, Z.Q. & Salmeron, M.
"STM studies on the growth of monolayers: Co on Cu(110) with one half monolayer of preadsorbed oxygen"
Surface Science 450, 227 (2000)

5. Escorcia-Aparicio, E.J., Wolfe, J.H., Choi, H.J., <u>Ling, W.L.</u>, Kawakami, R.K. & Qiu, Z.Q.
"Magnetic phases of thin Fe films grown on stepped Cr(001)"
Physical Review B 59, 11892-11896 (1999)

4. Escorcia-Aparicio, E.J., Choi, H.J., Wolfe, J.H., <u>Ling, W.L.</u>, Kawakami, R.K. & Qiu, Z.Q.
"Modification of the magnetic properties of Fe/Cr(001) by controlling the compensation of a vicinal Cr(001) surface"
Journal of Applied Physics 85, 4961-4963 (1999)

3. Escorcia Aparicio, E.J., Choi, H.J., <u>Ling, W.L.</u>, Kawakami, R.K. & Qiu, Z.Q.
"90 degrees magnetization switching in thin Fe films grown on stepped Cr(001)"
Physical Review Letters 81, 2144-2147 (1998)

2. Escorcia Aparicio, E.J., Choi, H.J., <u>Ling, W.L.</u>, Kawakami, R.K. & Qiu, Z.Q.

"The effect of interfacial steps on the ferromagnetic/antiferromagnetic interface of thin Fe films on Cr(001)"
IEEE Transactions on Magnetics 34, 1219-1221 (1998)
1. Chu, M.S., Greene, J.M., <u>Ling, W.</u>, Turnbull, A.D., Berk, H.L., Rosenbluth, M.N.
"A numerical study of the Alfvén continuum damping of toroidal Alfvén eigenmodes"
Physics of Plasmas 1, 1214-25 (1994)